PROTON INDUCED FISSION CROSS SECTIONS OF THE URANIUM ISOTOPES ^{233}U, ^{234}U, ^{235}U, ^{236}U, AND ^{238}U.

by

James Reid Boyce

Department of Physics
Duke University

Date: July 26, 1972

Approved:

Henry W. Newson, Supervisor

Edward G. Bilpuch

Eugene Greuling

David A. Hess

A dissertation submitted in partial fulfillment of the requirements for the degree of Doctor of Philosophy in the Department of Physics in the Graduate School of Duke University

1972

PROTON INDUCED FISSION CROSS SECTIONS FOR THE URANIUM ISOTOPES ^{233}U, ^{234}U, ^{235}U, ^{236}U, AND ^{238}U.

by

James Reid Boyce

The Cyclo-Graaff facility at Triangle Universities Nuclear Laboratory located on the Duke University campus was used to measure proton induced total fission cross sections for the uranium isotopes ^{233}U, ^{234}U, ^{235}U, ^{236}U, and ^{238}U. The 90° differential cross sections were measured for the incident proton energy range $4.5 \leq E_p \leq 31.0$ MeV in 250 keV and smaller energy steps with a maximum beam-energy spread of 5 keV at 30 MeV. In addition over 100 fission fragment angular distributions were measured at angular intervals of 10° between 20° and 160° and were analyzed to determine fission fragment anisotropies as a function of excitation energy. The angular distribution results were combined with the 90° differential cross sections to obtain accurate proton induced total fission cross sections. Targets used were supplied by Oak Ridge National Laboratory and were of isotopic purity greater than 99%. Surface barrier fission fragment counters were used to detect fission fragments.

A method of analysis has been developed and demonstrated whereby first, second, and third chance fission contributions to the total yield are estimated. The method utilizes the optical model to describe the formation of the compound system and a

statistical formalism to describe the de-excitation of the excited compound nucleus in either fission or neutron channels as the dominant decay mechanism. The analysis of cross section ratios for different isotopes clearly indicates that conventional optical models overestimate the proton total reaction cross section for incident proton energies below the Coulomb barrier. An empirically adjusted reaction cross section is therefore used for the compound nucleus formation cross section used in the calculations. The sensitivity of the analysis to various assumptions and model parameters is discussed.

The analysis of the measured cross section data results in the determination of previously unreported fission thresholds and the energy dependence of neutron to fission branching ratios, Γ_n/Γ_f, for all isotopes studied. The formulation is general enough to allow incorporation of refinements based on the current state of nuclear theory.

ACKNOWLEGMENTS

I am extremely grateful to three people without whose supervision, interest, and encouragement this work would not have been possible: Professor Henry W. Newson, especially for introducing me to the fascinating field of nuclear fission; Dr. H. W. Schmitt, for suggesting this particular project; and Dr. F. O. Purser, for daily conversations, advice, and guidance exploring all facets of this research.

I am also greatly indebted to Dr. T. D. Hayward for much of the angular distribution analysis. The discussions with Dr. W. J. Thompson and Mr. R. Eastgate concerning the optical model were of great value to me. I am especially grateful to Dr. Reiner Bass for his suggestions and advice in the analysis stages of this work.

The support and encouragement Dr. E. G. Bilpuch extended to me in all my endeavors at Duke and TUNL is gratefully acknowledged. I am also appreciative of the interest Dr. Eugene Greuling has expressed throughout all my studies at Duke.

To the entire TUNL staff, and especially Messrs. R. L. Rummel, M. T. Smith, S. E. Edwards, and A. W. Lovette, I extend a heartfelt thanks not only for maintaining the equipment used in this research, but also for providing a most pleasant atmosphere within which to work.

I will be eternally grateful to my parents whose sacrifices for my education cannot be overemphasized. To my fiancee, Miss

Linda Neal, I owe my greatest debt. Without her friendship, trust, love, and patience I would not have been able to complete graduate school.

This work was supported in part by the United Stated Atomic Energy Commission. Targets for this research were supplied by Oak Ridge National Laboratory.

J.R.B.
July 26, 1972

CONTENTS

LIST OF FIGURES

LIST OF TABLES

PROTON INDUCED FISSION CROSS SECTIONS

FOR THE URANIUM ISOTOPES

^{233}U, ^{234}U, ^{235}U, ^{236}U, AND ^{238}U.

Chapter I
INTRODUCTION

Since the discovery of nuclear fission by Otto Hahn and Fritz Strassmaan in 1938 and its interpretation by Lise Meitner and Otto Frisch, physicists have tried to determine the nuclear processes which result in fission. In recent years fission research has been greatly stimulated by advances in the technologies of detectors, fast electronics, and computers. These efforts have resulted in some rather exotic discoveries such as the now famous shape isomers and the double humped fission barrier.

In part stimulated by new experimental results, fission theory has received new emphasis in the past five years. The initial theoretical impetus was provided by the work of Strutinsky[1] who developed a method of correcting liquid drop potentials with contributions to the nuclear potential surface from shell model theory. These corrections led directly to predictions of a two peaked fission barrier in the mass region of the actinide nuclei and provided a ready explanation of previously difficult to explain phenomena such as isomeric fission and sub-threshold fission resonances. Extensions of this idea by Strutinsky[1,2] and many others[3] led to the prediction of a region of stable nuclei around A=296 which in turn has generated much of the current interest in heavy ion research.

A complete theory of fission must include an explanation of the dependence of fission characteristics upon excitation energy. This is particularly relevant to the problem of

producing super-heavy nuclei as most of the proposed reactions leading to such nuclei require the formation of a very heavy intermediate compound nucleus at a very high excitation energy. Success or failure in forming the desired stable super-heavy nuclei will depend in large measure upon whether the intermediate compound nucleus can de-excite sufficiently by sequential particle and gamma emission to reach the island of stability in the mass region around A=296 or whether fission will interrupt the de-excitation process at some point in the decay chain. Detailed information regarding the fission/particle emission branching ratio as a function of excitation energy is necessary to provide a clear picture of the probabilities involved.

For very moderate excitation energies the present experimental picture of fission is clouded because neutron evaporation competes with fission. Sequential neutrons can be evaporated from the excited initial compound nucleus and any one of the residual nuclei along the evaporation chain may fission, provided the evaporation process leaves it with sufficient excitation energy.

The fact that a nucleus can undergo fission or evaporate one or more neutrons and still have a chance to fission has led to the following terminology: The fission process of the initial nucleus is called first chance fission. If one, two, ... , n neutrons are evaporated prior to fission, the process is respectively called second, third, ..., (n+1)th chance fission. This multiple chance fission effect was first seen in the fast neutron induced total fission cross sections of the actinides. At the onset of each additional fission chance there is a distinct rise in the cross section. Thus above second chance threshold at a given initial excitation energy, recorded fission data will contain contributions from at least two different fissioning nuclei, which, moreover, are fissioning at quite

different excitation energies.

Much of the currently available data regarding the energy dependence of the branching ratios, Γ_n/Γ_f , is due to the work of Vandenbosch, Huizenga, and their co-workers.[4] A large part of their work has dealt with target nuclei with A≤210, a region in which the effect of second chance fission is reduced by virtue of the high fission barriers involved. All available experimental results for heavier nuclei at the excitation energies in question contain estimated but undiscriminated contributions from a sequence of fissioning nuclei produced by competing particle emission.

Simple extrapolation to higher mass regions on the basis of well known Γ_n/Γ_f data for A≤210 is unreliable. The shell corrections involved in the potential surfaces affecting both ground state and saddle point characteristics are strongly N, Z, and deformation dependent.

The purpose of the investigations reported here is to develop a method by which useable branching ratio expressions can be obtained for those experimental situations in which multiple chance fission occurs. Basically the method used consisted of measuring accurate proton induced total fission cross sections over a large energy range, 4.5 MeV ≤ Ep ≤ 31.0 MeV, and with small energy steps, for the five isotopes of uranium, ^{233}U, ^{234}U, ^{235}U, ^{236}U, and ^{238}U. In this way the threshold for each fission chance, up through fourth chance, is systematically crossed. By comparing the results from neighboring isotopes with a statistical model we obtain a self consistent set of fission thresholds and energy dependent branching ratio expressions for eight isotopes of neptunium.

Two types of experiments were required. First, 90° differential fission cross section yield curves were measured. Second, in order to obtain accurate total fission cross sections, over 100 eighteen point fission fragment angular distributions were measured. These are of interest in themselves since much of the information in the literature was taken at only two angles; however, for the present analysis only the functional form of the dependence of the cross section on angle and energy is needed, and detailed analysis of these data to obtain information on angular momentum effects in fission has been left to the future.

Chapter II describes the experimental equipment used, the data collection and reduction procedures, and a summary of experimental uncertainties. In Chapter III the theoretical statistical basis and the model used in the analysis are described. In order to preserve continuity useful information of a digressional nature has been relegated to the appendices.

Chapter II
EXPERIMENTAL METHOD
A. Experimental Equipment

The experiments reported in this dissertation were conducted at the Cyclo-Graaff facility of Triangle Universities Nuclear Laboratory. The laboratory is schematically shown in Figure 1.

A negative ion isochronous cyclotron served as a fixed energy injector for an FN tandem Van de Graaff accelerator. The proton energy range from 2 to 16 MeV was accessible by using the tandem only. Above 17 MeV the external 15 Million volt H^- beam from the cyclotron was injected through the HVEC source arrangement into the tandem. The useful energy range was thus extended to 31 MeV.

The emerging beam was then directed into one of two target areas depending on the experiment. The differential cross section yield curves were measured in high resolution target area #4 (Fig. 1). The beam from the tandem was passed through a unique high resolution analyzing system consisting of two 90° magnets with 40" radii, two singlet quadrupoles, and tunable sextupoles for controlling second order aberrations. With this analyzing system the maximum beam energy spread for the yield curve data was kept below 5 keV. The fission fragment angular distributions were measured in target area #1 in a 24" diameter scattering chamber.

Figure 2 shows the basic chamber setup used in the measurements. At the entrance to the scattering chamber the

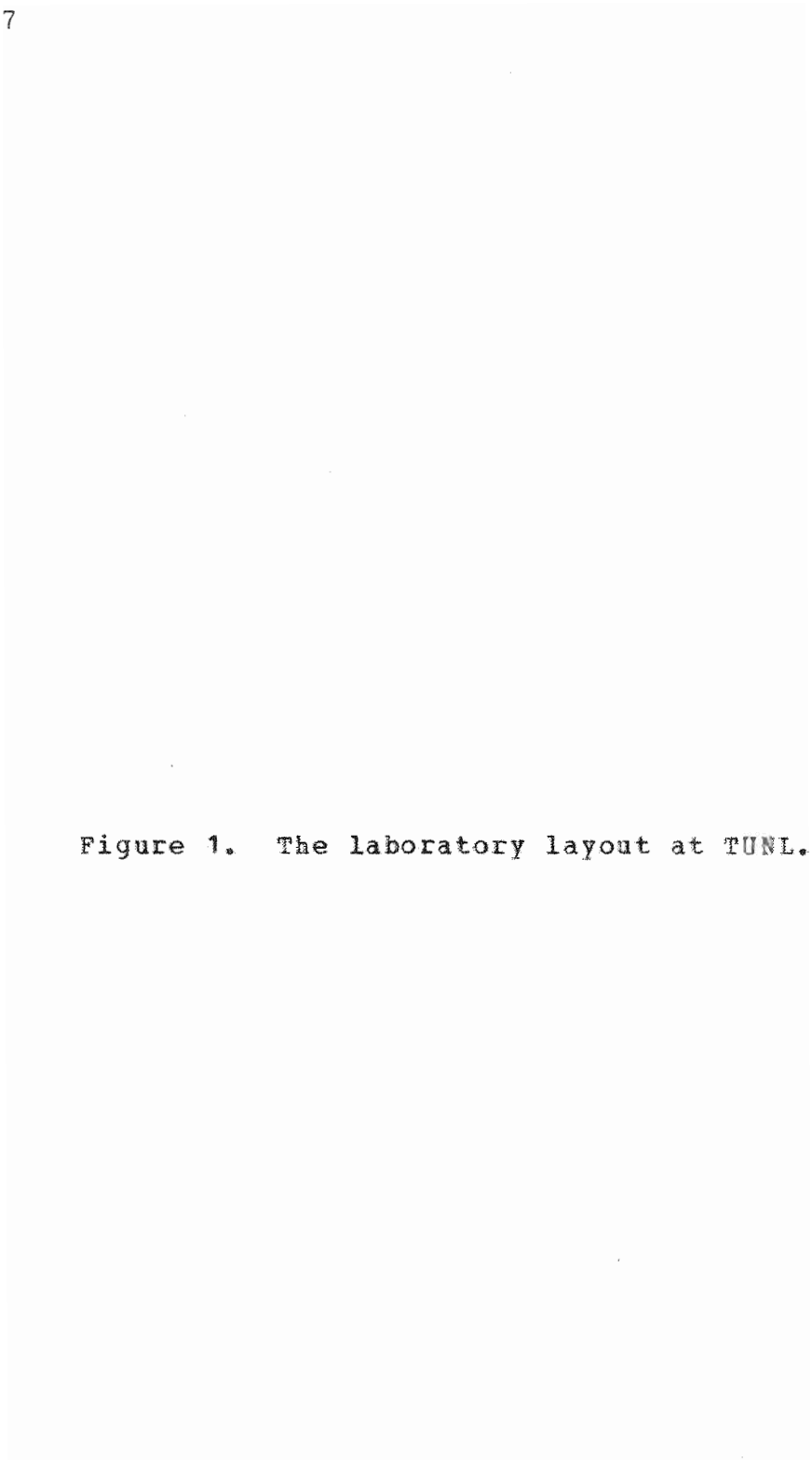

Figure 1. The laboratory layout at TUNL.

Cyclo-Graaff Laboratory -TUNL

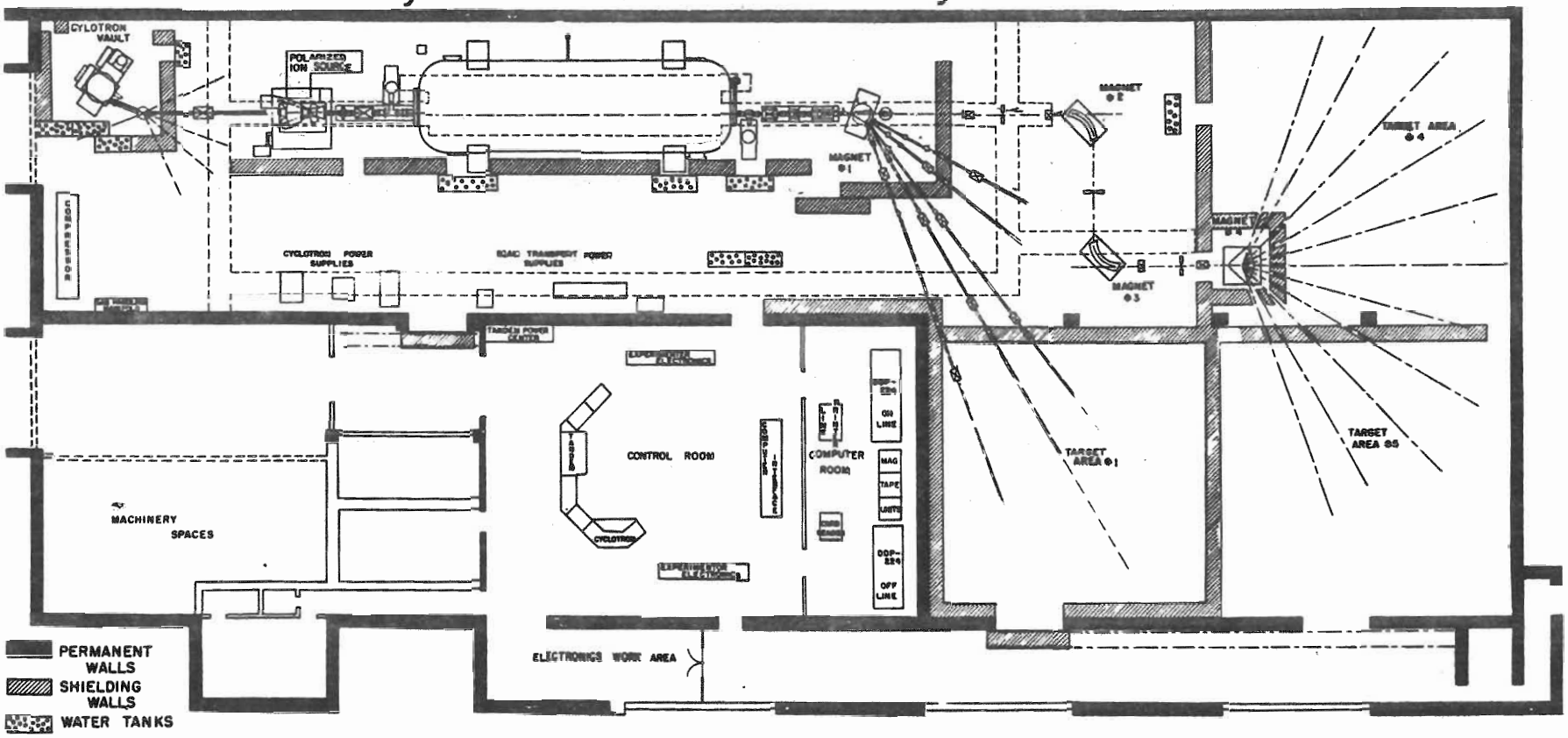

Figure 2. The basic scattering chamber setup.
(Not to scale.)

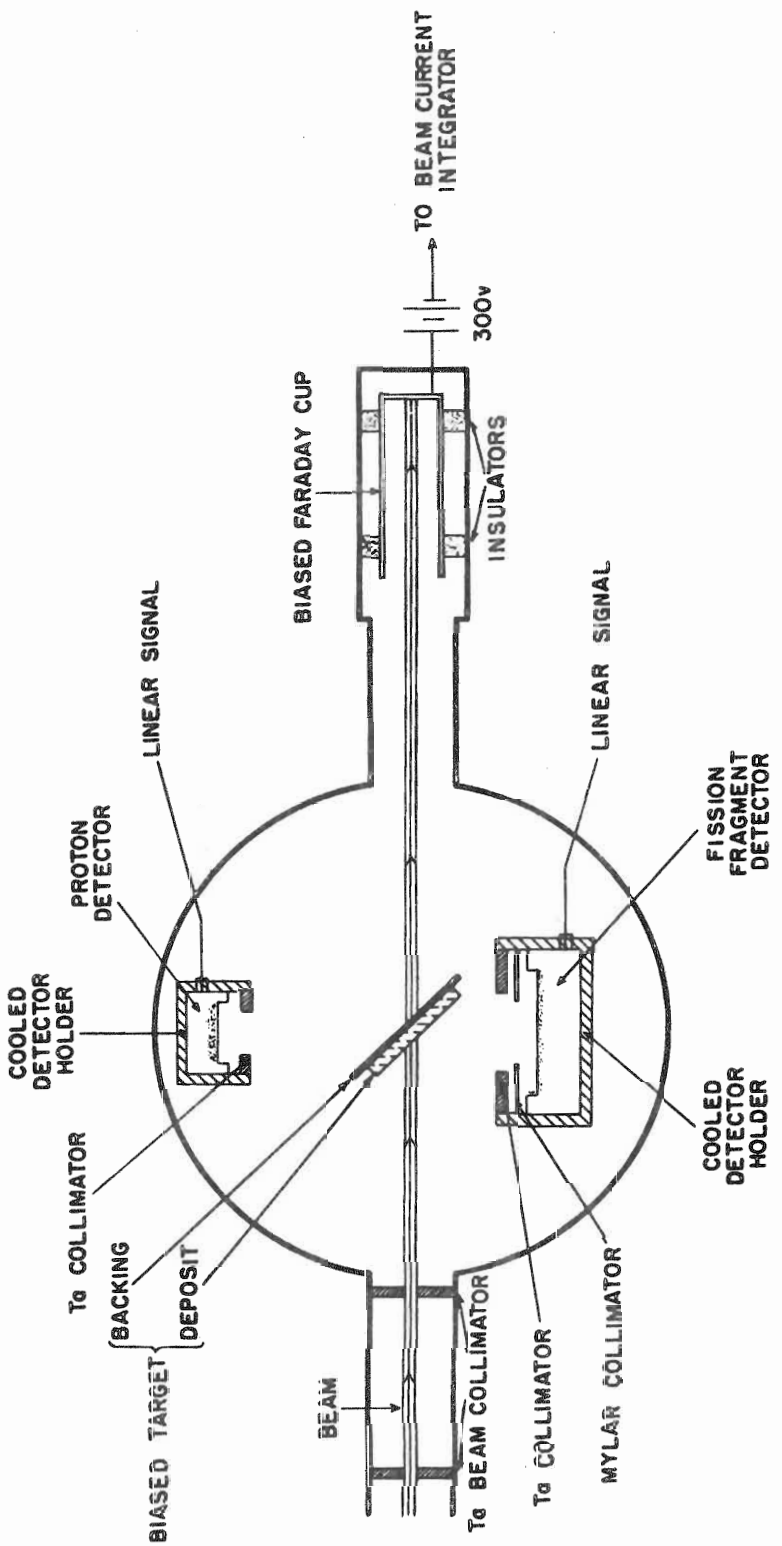
TO BEAM CURRENT INTEGRATOR
300v
BIASED FARADAY CUP
INSULATORS
LINEAR SIGNAL
PROTON DETECTOR
COOLED DETECTOR HOLDER
To COLLIMATOR
BACKING
DEPOSIT
BIASED TARGET
BEAM
To BEAM COLLIMATOR
To COLLIMATOR
MYLAR COLLIMATOR
LINEAR SIGNAL
FISSION FRAGMENT DETECTOR
COOLED DETECTOR HOLDER

beam was tightly collimated to minimize beam spot wander on target. Targets were biased to suppress electron emission and the beam was collected in a well isolated Faraday cup biased to +300 volts for accurate beam current integration. Tests of integration reliablility conducted with widely varying beam currents and charge collection times revealed no systematic variations.

The targets supplied by Oak Ridge National Laboratory were of isotopic purity greater than 99%. Individual target characteristics are summarized in Table I. Each target was positioned at 45° to the beam in the center of the chamber with the uranium deposit facing both the incoming beam and the detector. The beam energy loss in the target was estimated to be less than 3 keV at E_p = 5 MeV and less at higher energies.

Aluminum gauge blocks were used to position the detector collimators to an accuracy of ± 0.004" with respect to the center of the chamber. The solid angle for fission fragments was determined by 0.2 mm thick mylar collimators. Thick (1.5 mm) tantalum collimators were used to prevent high energy proton interactions in the nonuniform areas of the detectors. The inner diameter of the tantalum collimators was chosen so that fission fragments scattered from the tantalum were intercepted by the mylar collimators.

Fission fragment detectors used were commercial surface barrier detectors 70 μ thick. They were cooled to dry ice temperatures to improve their lifetimes. Two 2-mm Si surface barrier detectors were used for target thickness and uniformity measurements and for the elastically scattered proton angular distribution measurements.

TABLE I.

Target Characteristics

Target (backing)	Batch Composition A percent	Thickness at 45° (μg/cm²) a	b	c
^{233}U (carbon)	233 99.998 234 <0.001 235 <0.001 236 <0.001 238 <0.001	78.80 ±0.74	82.64 ±0.53	80.20 ±0.74
^{234}U (nickel)	233 0.038 234 99.420 235 0.303 236 0.077 238 0.162	101.48 ±1.80	107.79 ±0.91	102.28 ±0.95
^{235}U (carbon)	233 <0.001 234 <0.939 235 99.44 236 0.454 238 0.067	72.34 ±0.42	73.53 ±0.28	74.66 ±0.97
^{236}U (nickel)	233 0.010 234 0.001 235 0.199 236 99.680 238 0.110	139.72 ±0.95	147.06 ±1.35	139.70 ±1.21
^{238}U (carbon)	233 <0.01 234 <0.01 235 <0.01 236 <0.01 238 >99.9	25.25 ±0.20	25.00 ±0.34	24.28 ±0.29

Method of Measurement
(See Appendix A)

a: Coulomb scattering of 10.0 MeV alpha particles.
b: Coulomb scattering of 5.0 MeV protons.
c: The 5 MeV proton data corrected for contaminant.

A block diagram of the electronic circuitry is shown in Figure 3. Amplified and shaped detector signals were collected by an ADC (analog to digital converter) interrupted DDP-224 on-line computer (Fig. 3a). Up to four detector circuits could be accommodated in this manner. Pulses from the beam current integrator (BCI) were counted by a scaler bank (Fig. 3b). One scaler was gated off by the ADC busy signal to correct for dead time. Another scaler measured the total charge. An average beam monitor was used to gate off all counting devices if the beam level exceeded allowable bounds. The computer clock was connected to a scaler to record the elapsed time for each run.

In general the devices were turned on simultaneously at the start of each run and were gated off when a preset scaler count was reached. Their information was then read into the computer and stored on magnetic tape. The information was also printed out on the line printer as a safety precaution.

Acceptable beam current levels were established to minimize dead time effects. Beam currents were computer monitored and all data devices were disabled if the acceptable limits were exceeded. The dead time correction was held below 5% in all cases.

Figure 3. Block diagram of the electronic circuitry.
a. Detector signal circuit.
b. Beam integration circuit.
c. Data storage circuit.

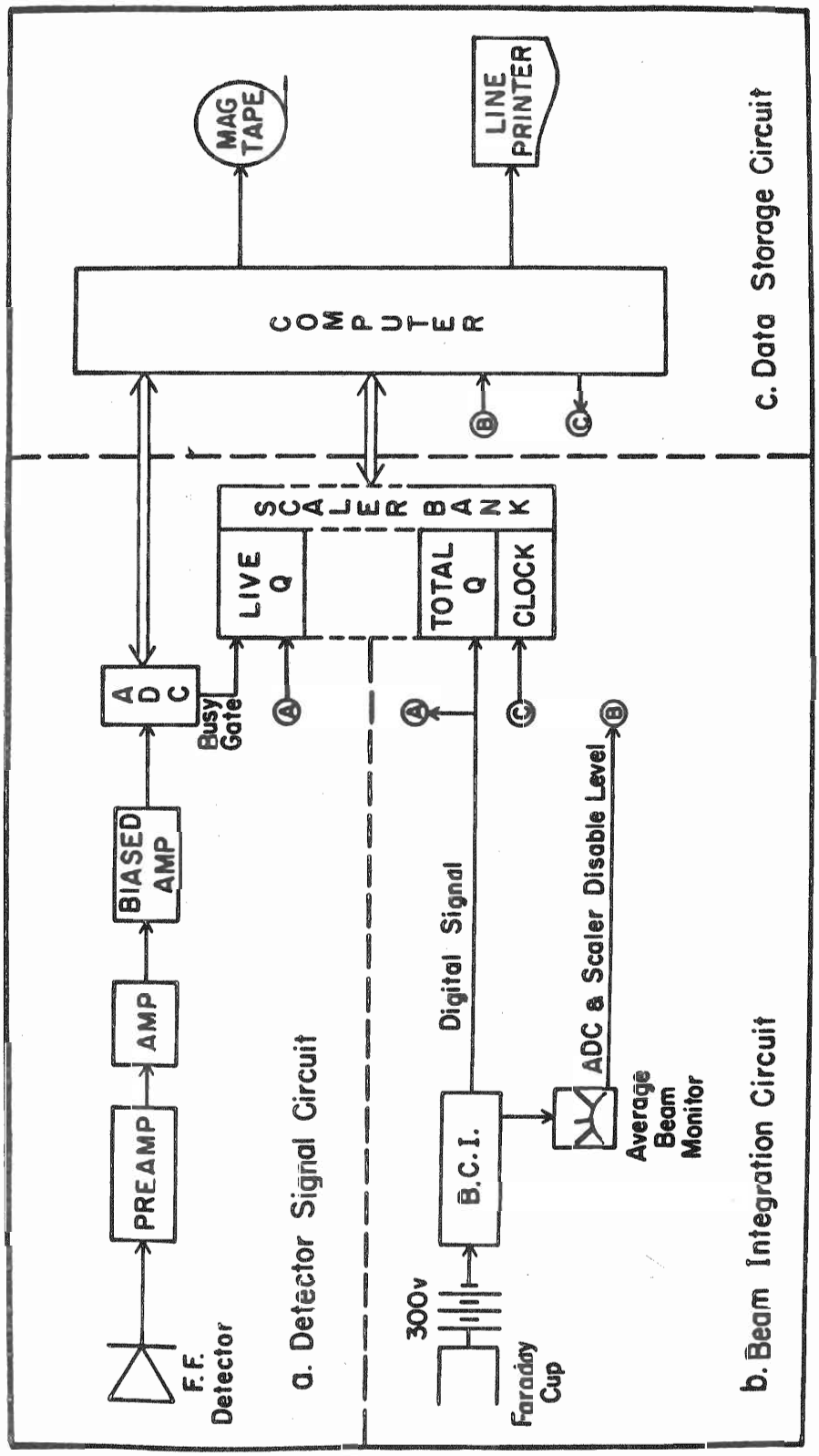
MAG TAPE
LINE PRINTER
COMPUTER
SCALER BANK
LIVE Q
TOTAL Q
CLOCK
ADC
Busy Gate
BIASED AMP
AMP
PREAMP
F.F. Detector
a. Detector Signal Circuit
Digital Signal
B.C.I.
300v
Faraday Cup
ADC & Scaler Disable Level
Average Beam Monitor
b. Beam Integration Circuit
c. Data Storage Circuit
A
B
C

B. Data Collection and Reduction

1. The fission differential cross section measurements.

The procedure for measuring the differential cross section yield curves was designed to ensure accuracy in the determination of the absolute cross sections and to minimize any possible systematic errors in the results. The basic procedure involved three steps. First; the uranium target thicknesses were measured by Coulomb scattering of alpha particles and protons as is described in detail in Appendix A. Second; the proton beam energy was increased and fission yields were measured at 10, 11, 12, and 13 MeV. Great care was taken to ensure that target, detector and beam geometry was not changed between the Coulomb scattered proton measurements and the fission yield measurements, and sufficient counts were accumulated at each energy to make the associated statistical uncertainty negligible. Third; the relative fission yields at 90° were measured and the results normalized to the very accurately determined calibration points at 10, 11, 12, and 13 MeV. During each extended data run the four calibration points were periodically measured and, when necessary, new normalization factors were calculated before the data were incorporated in the final yield curves. This technique eliminates any effect on the data due to erosion of the target by the beam.

An additional check on target erosion was made for the ^{235}U data. The initial yield curve was measured in ascending 500 keV steps to the highest energy point. Intermediate points were then measured in descending 500 keV steps and were found to be completely consistent over the entire energy range with the data taken initially.

A final check on the accuracy of the cross section results was made by repeating most of the yield curve data over a period of several months. In every case the data were reproducible within the accuracy quoted.

Figure 4 shows three sample spectra in which each count represents a fission event. Straightforward application of the definition of differential cross section gives the basic formula used to convert counts to cross section:

$$\sigma(90^\circ) = \frac{N_e}{N_i \times N_t \times \Delta\Omega} ,$$

where: N_e is the number of events.
N_i is the number of incident beam particles.
N_t is the number of nuclei per unit area in the target.
$\Delta\Omega$ is the solid angle subtended by the detector. Note that $\Delta\Omega$ is twice the geometrical solid angle defined by the collimators because there are two fission fragments per fission event.

N_e was taken to be the sum of all counts in the spectrum since background counts were of low energy compared to the fission fragment counts and they were biased out prior to the ADC. Thus the uncertainty of N_e was statistical and was kept below 1% whenever possible. In the low energy region the low counting rate forced acceptance of statistical uncertainties larger than this. Beam current integration gives the value of N_i. Reproducibility tests using various beam intensities indicated an upper limit in the uncertainty of N_i of 0.5%. Target uniformity and thickness measurements discussed in Appendix A gives an uncertainty of about 1.0% in N_t. The accuracy in positioning the detectors and collimators resulted in a solid angle uncertainty of about 1.0%.

Figure 4. Representative fission fragment pulse height spectra.

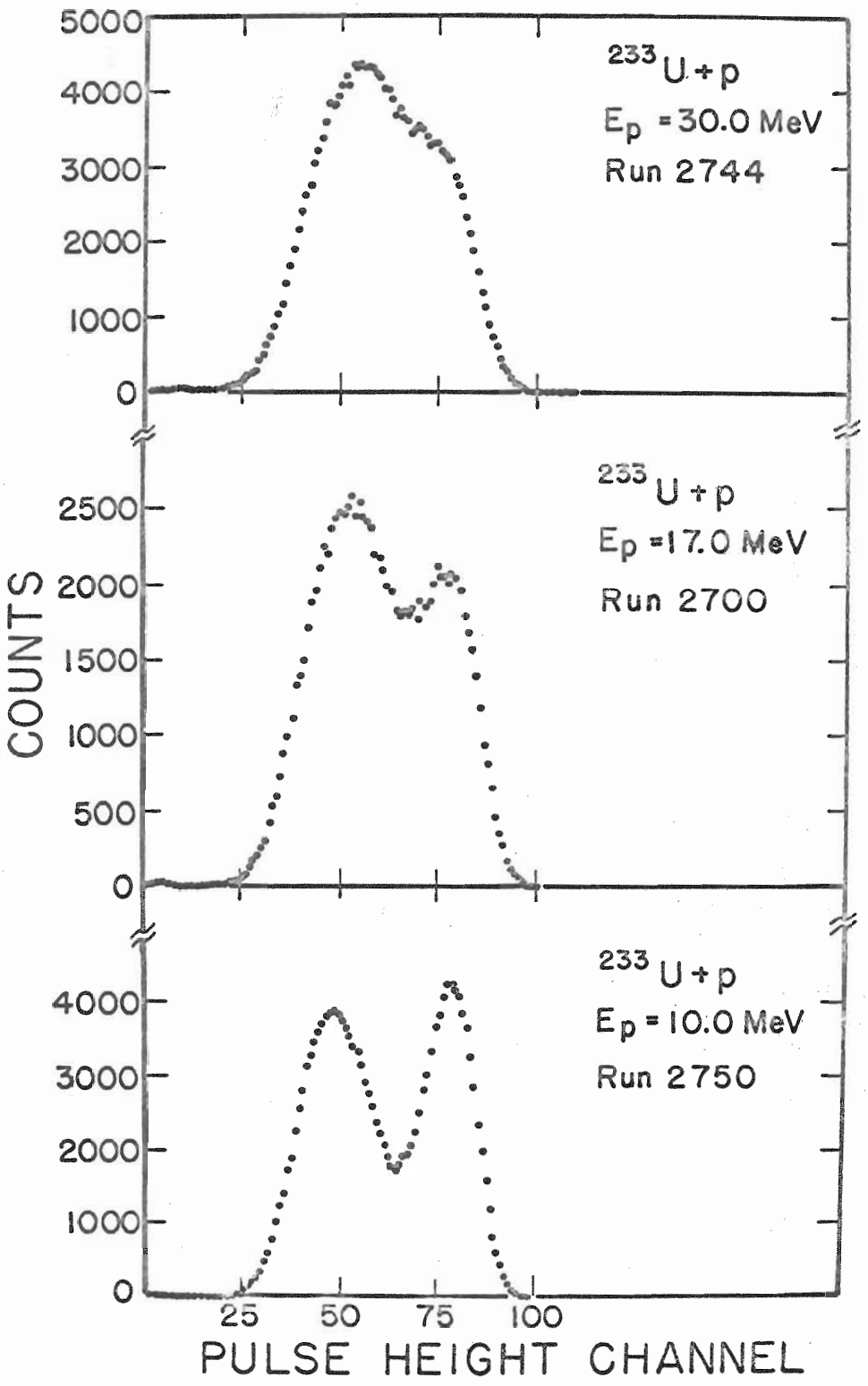
5000
4000
3000
2000
1000
0
^{233}U + p
E_p = 30.0 MeV
Run 2744
2500
2000
1500
1000
500
0
^{233}U + p
E_p = 17.0 MeV
Run 2700
COUNTS
4000
3000
2000
1000
0
^{233}U + p
E_p = 10.0 MeV
Run 2750
25
50
75
100
PULSE HEIGHT CHANNEL

Figure 5 shows the final results for the 90° differential fission cross sections. Note that in this figure the data for the five isotopes as shown contain a scale factor f which allows adequate visual separation. The overall similarity of these curves is evident.

2. The fission angular distribution measurements.

For most of the fission fragment angular distributions two detectors were positioned 180° apart in the 24" diameter chamber, one on either side of the target. Data were taken at 10° intervals between 20° and 160° with data taken by each detector at 80°, 90°, and 100°. The back angle detector counts were normalized to the forward detector counts at the overlapping angles. This was to correct for discrepancies in the solid angles defined by each detector and to correct any effects of fragment scattering by the backing. A typical distribution is shown in Figure 6. Further discussion of the analysis of these distributions is given in Appendix B.

The main result of the analysis is that in the center of mass all angular distributions have the form

$$\sigma(\theta) = W(\theta)\,\sigma(90°) = (1 + \epsilon \cos^2\theta)\,\sigma(90°) \quad .$$

The extensive fitting procedures discussed in Appendix B show that higher order coefficients in the expansion are consistent with zero. Table II contains the final values for the anisotropy coefficient, ϵ, and Figure 7 shows these coefficients as functions of incident beam energy. The smooth line drawn through the points represents only a visual fit through these data.

Figure 5. Final differential cross sections for the five targets ^{233}U, ^{234}U, ^{235}U, ^{236}U, and ^{238}U. The proton energy region from 16 to 17 MeV is normally inaccessible to the TUNL facility as it is above the rated energy of the FN tandem alone and below the lowest available Cyclo-Graaff energy. This is responsible for the missing data in the figure for ^{233}U and ^{234}U.

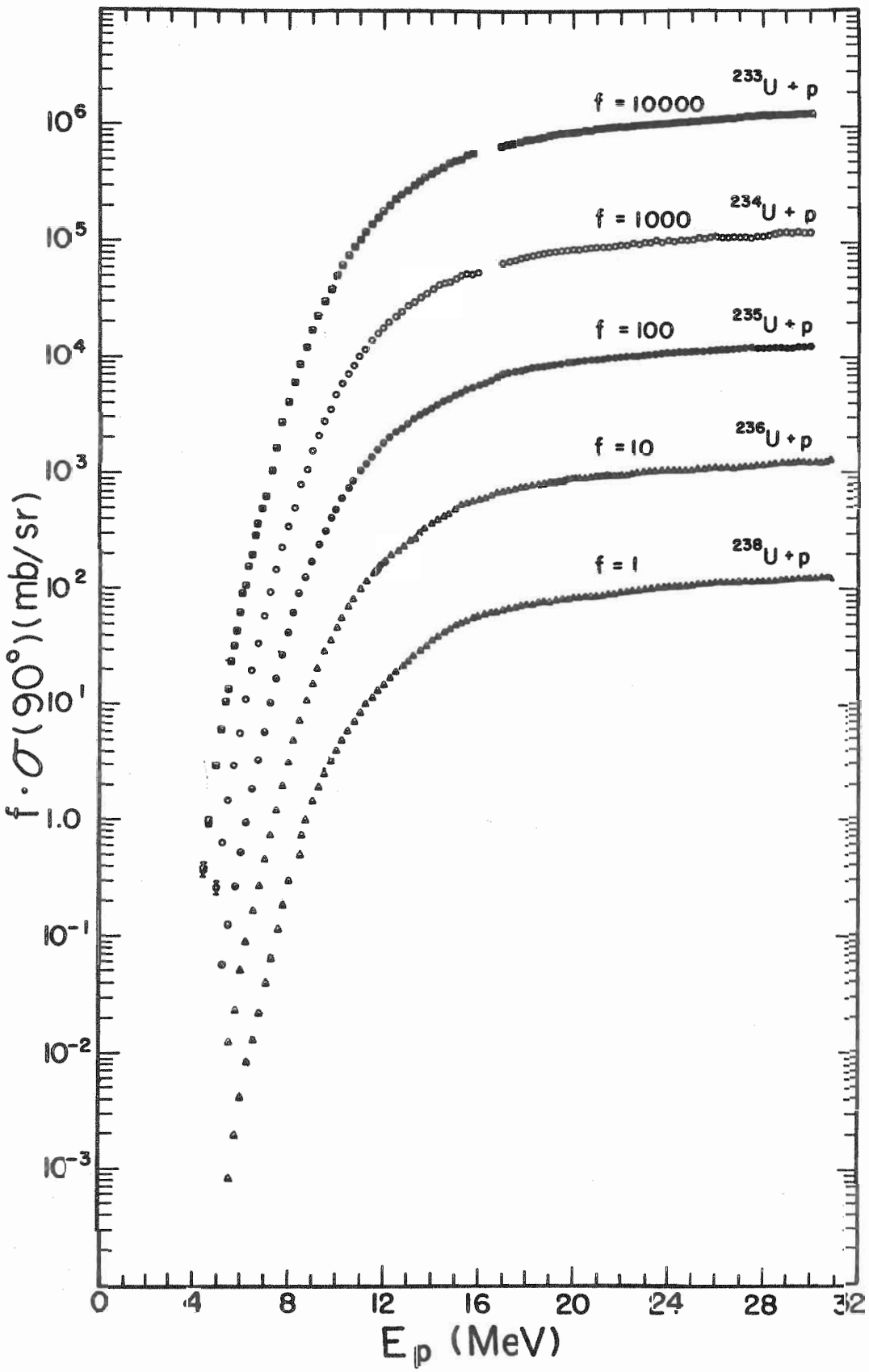
f = 10000
233U + p
f = 1000
234U + p
f = 100
235U + p
f = 10
236U + p
f = 1
238U + p
f · σ(90°) (mb/sr)
E_p (MeV)
10^6
10^5
10^4
10^3
10^2
10^1
1.0
10^-1
10^-2
10^-3
0
4
8
12
16
20
24
28
32

Figure 6. Typical fission fragment angular distribution.

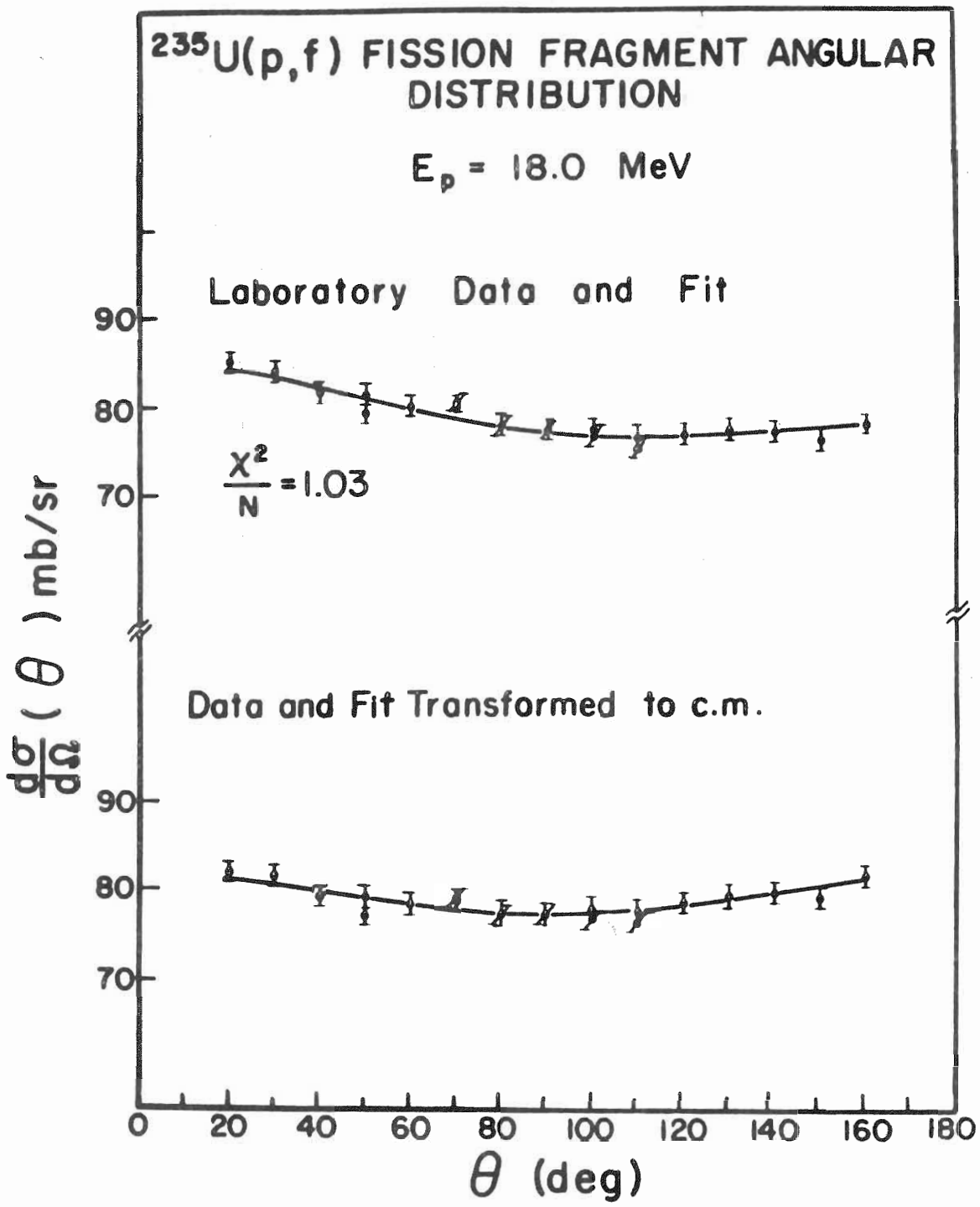
^{235}U(p,f) FISSION FRAGMENT ANGULAR DISTRIBUTION
E_p = 18.0 MeV
Laboratory Data and Fit
$\frac{\chi^2}{N}$ = 1.03
Data and Fit Transformed to c.m.
$\frac{d\sigma}{d\Omega}(\theta)$ mb/sr
90
80
70
0
20
40
60
80
100
120
140
160
180
θ (deg)

TABLE II

Experimental Fission Fragment Anisotropy Coefficients

Proton Energy (MeV)	^{233}U + p Anisotropy Coefficient	^{234}U + p Anisotropy Coefficient
10.000	0.46850E-01 ± 0.23E-01	0.70230E-01 ± 0.10E-01
12.000	0.61590E-01 ± 0.12E-01	0.60660E-01 ± 0.52E-02
14.000	0.49690E-01 ± 0.82E-02	0.39480E-01 ± 0.61E-02
15.000	0.46000E-01 ± 0.21E-01	0.57010E-01 ± 0.54E-02
16.000	0.63680E-01 ± 0.94E-02	0.70220E-01 ± 0.50E-02
17.000		0.55520E-01 ± 0.65E-02
18.000	0.88120E-01 ± 0.12E-01	0.78400E-01 ± 0.62E-02
20.000	0.96060E-01 ± 0.11E-01	0.99380E-01 ± 0.58E-02
22.000	0.68860E-01 ± 0.10E-01	0.81750E-01 ± 0.55E-02
24.000	0.86000E-01 ± 0.98E-02	0.11150E 00 ± 0.53E-02
26.000	0.97520E-01 ± 0.96E-02	0.10460E 00 ± 0.62E-02
28.000	0.11080E 00 ± 0.94E-02	0.10510E 00 ± 0.61E-02
30.000	0.11720E 00 ± 0.92E-02	0.91710E-01 ± 0.59E-02

TABLE II
(continued)
Experimental Fission Fragment Anisotropy Coefficients

Proton Energy (MeV)	^{235}U + p Anisotropy Coefficient	^{236}U + p Anisotropy Coefficient
9.000	0.00000E-02 ± 0.13E-01	0.53710E-01 ± 0.85E-02
10.000	0.39160E-01 ± 0.11E-01	0.58180E-01 ± 0.71E-02
11.000		0.49470E-01 ± 0.44E-02
12.000	0.52500E-01 ± 0.84E-02	0.48680E-01 ± 0.41E-02
13.000		0.52250E-01 ± 0.38E-02
13.500		0.51900E-01 ± 0.50E-02
14.000	0.58610E-01 ± 0.52E-02	0.64130E-01 ± 0.45E-02
15.000	0.50010E-01 ± 0.71E-02	0.74501E-01 ± 0.32E-02
15.500		0.80940E-01 ± 0.37E-02
16.000	0.64690E-01 ± 0.65E-02	0.88240E-01 ± 0.28E-02
16.500		0.92620E-01 ± 0.34E-02
17.000		0.90240E-01 ± 0.32E-02
17.500		0.92330E-01 ± 0.31E-02
18.000	0.55930E-01 ± 0.79E-02	0.94910E-01 ± 0.26E-02
18.500		0.92880E-01 ± 0.21E-02
19.000		0.95820E-01 ± 0.21E-02
19.500		0.96390E-01 ± 0.21E-02
20.000	0.60290E-01 ± 0.56E-02	0.94180E-01 ± 0.19E-02
20.500		0.90530E-01 ± 0.20E-02
21.000		0.10730E 00 ± 0.25E-02
22.000	0.82680E-01 ± 0.12E-01	0.10460E 00 ± 0.26E-02
23.000		0.10730E 00 ± 0.28E-02
24.000	0.75700E-01 ± 0.67E-02	0.11070E 00 ± 0.25E-02
24.500		0.97740E-01 ± 0.26E-02
25.000		0.10410E 00 ± 0.27E-02
25.500		0.10590E 00 ± 0.26E-02
26.000	0.10060E 00 ± 0.83E-02	0.11190E 00 ± 0.29E-02
27.000		0.11090E 00 ± 0.29E-02
28.000	0.11300E 00 ± 0.81E-02	0.11860E 00 ± 0.29E-02
29.000		0.11030E 00 ± 0.28E-02
29.500		0.12190E 00 ± 0.24E-02
30.000	0.10500E 00 ± 0.80E-02	0.12190E 00 ± 0.28E-02

TABLE II
(continued)
Experimental Fission Fragment Anisotropy Coefficients

Proton Energy (MeV)	^{238}U + p Anisotropy Coefficient
9.000	0.12110E 00 ± 0.48E-01
10.000	0.48280E-01 ± 0.15E-01
12.000	0.79550E-01 ± 0.11E-01
14.000	0.11370E 00 ± 0.15E-01
15.000	0.96910E-01 ± 0.14E-01
17.000	0.10430E 00 ± 0.80E-02
18.000	0.11690E 00 ± 0.96E-02
19.000	0.10730E 00 ± 0.73E-02
19.500	0.82360E-01 ± 0.12E-01
20.000	0.90340E-01 ± 0.71E-02
21.000	0.10740E 00 ± 0.69E-02
22.000	0.12530E 00 ± 0.84E-02
23.000	0.13360E 00 ± 0.66E-02
24.000	0.12260E 00 ± 0.11E-01
25.000	0.11270E 00 ± 0.57E-02
26.000	0.13150E 00 ± 0.62E-02
27.000	0.14330E 00 ± 0.61E-02
28.000	0.14470E 00 ± 0.61E-02
30.000	0.14980E 00 ± 0.60E-02

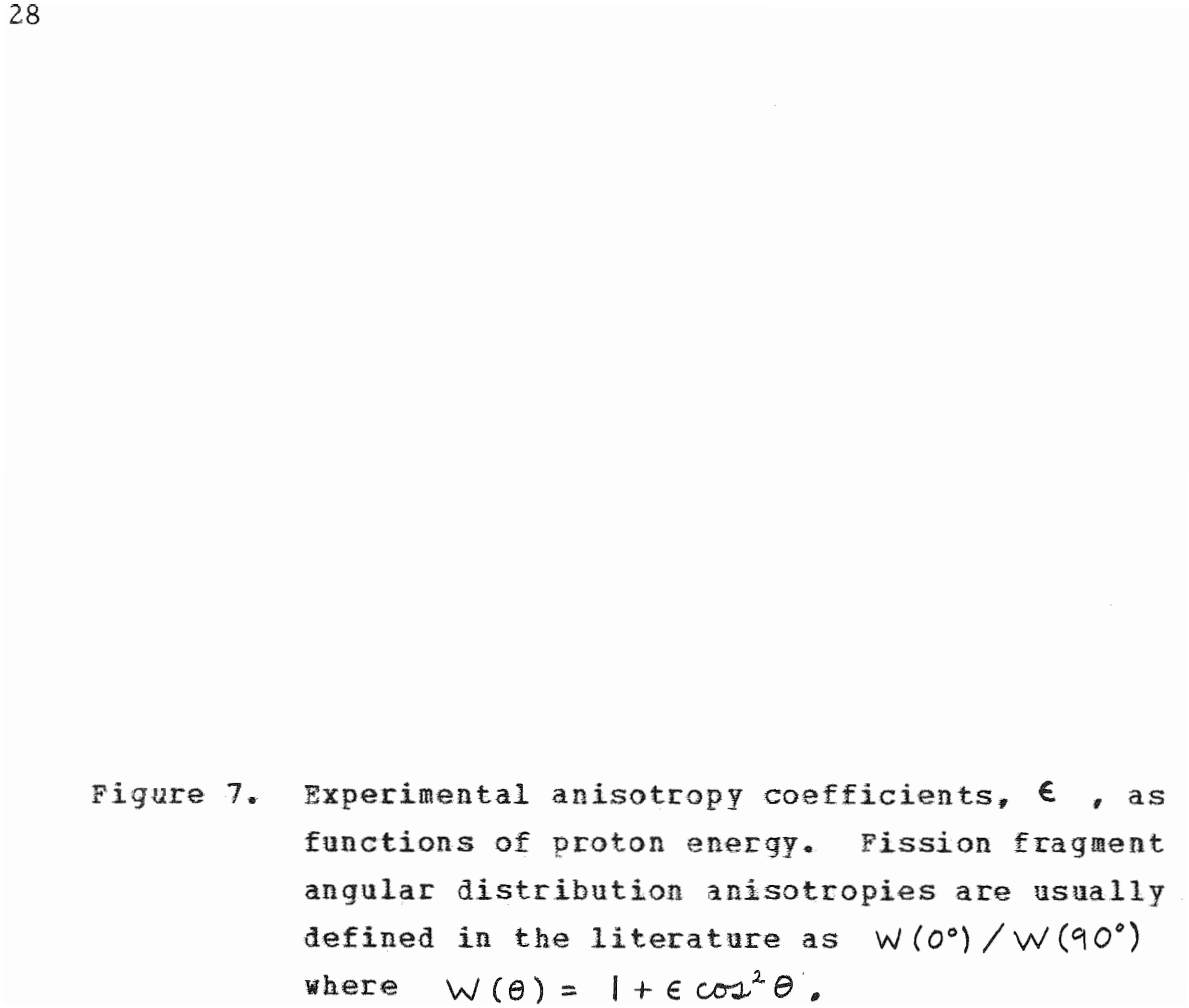

Figure 7. Experimental anisotropy coefficients, ϵ , as functions of proton energy. Fission fragment angular distribution anisotropies are usually defined in the literature as $W(0°)/W(90°)$ where $W(\theta) = 1 + \epsilon \cos^2\theta$.

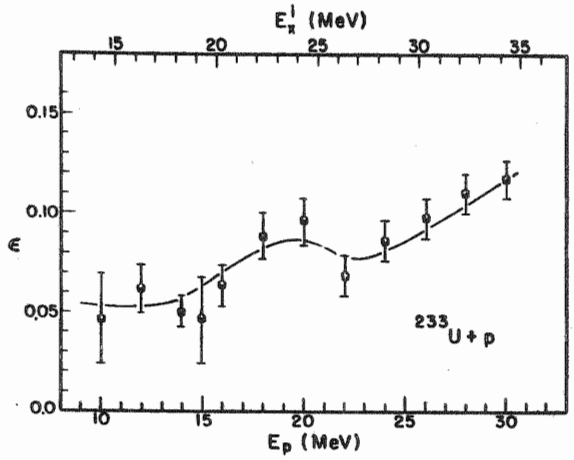
E_x^1 (MeV)
15 20 25 30 35
0.15
0.10
0.05
0.0
ϵ
$^{233}U + p$
10 15 20 25 30
E_p (MeV)

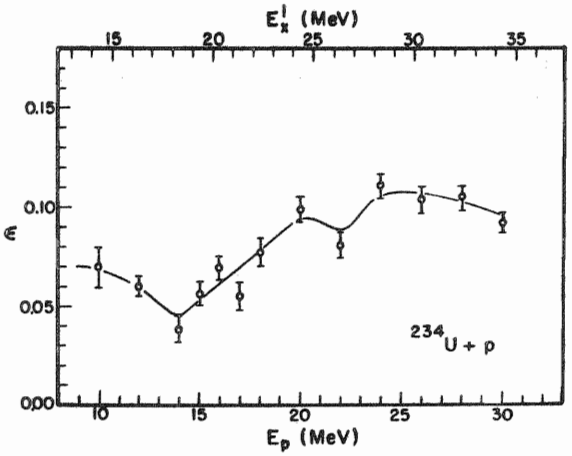
E_x^1 (MeV)
15 20 25 30 35
0.15
0.10
0.05
0.00
ϵ
$^{234}U + p$
10 15 20 25 30
E_p (MeV)

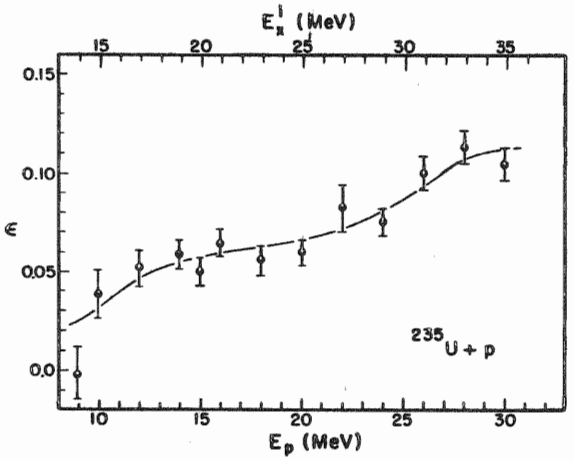
E_x^1 (MeV)
15 20 25 30 35
0.15
0.10
0.05
0.0
ϵ
$^{235}U + p$
10 15 20 25 30
E_p (MeV)

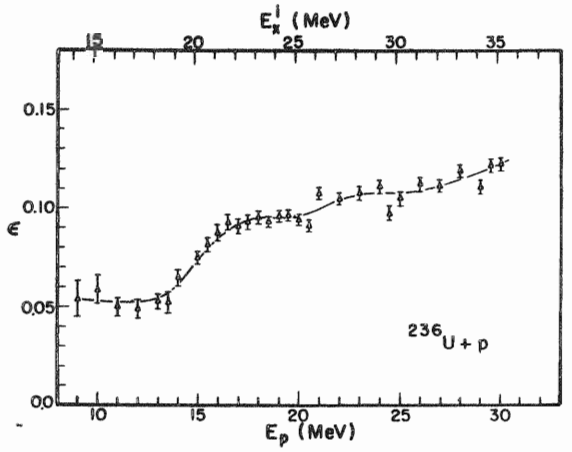
E_x^1 (MeV)
15 20 25 30 35
0.15
0.10
0.05
0.0
ϵ
$^{236}U + p$
10 15 20 25 30
E_p (MeV)

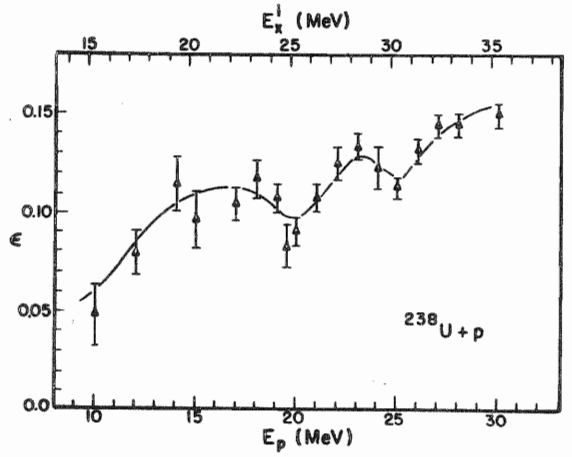
E_x^1 (MeV)
15 20 25 30 35
0.15
0.10
0.05
0.0
ϵ
$^{238}U + p$
10 15 20 25 30
E_p (MeV)

3. The total fission cross sections.

The total fission cross section is given by

$$\sigma_F = \int \sigma(\theta)\, d\Omega = 4\pi\left(1 + \frac{\epsilon}{3}\right)\sigma(90^\circ) \quad .$$

The values of ϵ used in obtaining the total cross sections were taken from the smooth lines in Figure 7. Since the anisotropy is a small correction to the total cross section the values actually used may differ somewhat from the true values without affecting the final cross sections appreciably.

Table III summarizes the experimental uncertainties in these data. The uncertainties were all combined in quadrature to give an upper limit of 2.0% total uncertainty in the cross section except where statistics made this number larger.

The total proton induced fission cross sections are listed in Table IV. When plotted on a semi-log scale these cross sections look identical to the curves of Figure 5 except for a vertical scale change. They look much like all other charged particle induced fission cross sections in that there is no apparent structure in the data. At low energies the behavior is dominated by the Coulomb barrier penetration whereas at high energies the fission cross section approaches the total reaction cross section.

Figure 8 shows these data as a function of excitation energy in the initial compound nucleus. The lower region of this graph has been expanded and is shown in Figure 9.

TABLE III

Experimental Uncertainties

Uncertainty	Target				
	^{233}U	^{234}U	^{235}U	^{236}U	^{238}U
Statistical*	1.00 %	1.00 %	1.00 %	1.00 %	1.00 %
Beam integration	0.50 %	0.50 %	0.50 %	0.50 %	0.50 %
Target thickness	0.93 %	0.93 %	1.30 %	0.87 %	1.20 %
Solid angle	1.00 %	1.00 %	1.00 %	1.00 %	1.00 %
Normalization	0.50 %	0.50 %	0.50 %	0.50 %	0.50 %
Anisotropy	0.50 %	0.50 %	0.50 %	0.50 %	0.50 %
Total uncertainty	1.87 %	1.87 %	2.08 %	1.84 %	2.00 %

*The statistical uncertainty of 1 % was arbitrarily set for the number of events, N_e, when $N_e \geq 10000$. When $N_e \leq 10000$ the uncertainty used was $100./\sqrt{N_e}$ %.

TABLE IV

Total Fission Cross Sections

Proton Energy (MeV)	^{233}U + p Cross Section (mb)	^{234}U + p Cross Section (mb)
4.500	0.48108E-03 ± 0.71E-04	
4.750	0.12375E-02 ± 0.10E-03	
5.000	0.38043E-02 ± 0.23E-03	0.35158E-02 ± 0.45E-03
5.250	0.79637E-02 ± 0.28E-03	0.85060E-02 ± 0.70E-03
5.375	0.13992E-01 ± 0.81E-03	
5.500	0.17511E-01 ± 0.97E-03	0.20075E-01 ± 0.14E-02
5.625	0.30309E-01 ± 0.15E-02	
5.750	0.41557E-01 ± 0.19E-02	0.38944E-01 ± 0.22E-02
5.875	0.57546E-01 ± 0.21E-02	
6.000	0.80849E-01 ± 0.28E-02	0.76739E-01 ± 0.31E-02
6.125	0.12030E 00 ± 0.42E-02	
6.250	0.13591E 00 ± 0.44E-02	0.15050E 00 ± 0.43E-02
6.375	0.20110E 00 ± 0.56E-02	
6.500	0.25288E 00 ± 0.23E-01	0.26632E 00 ± 0.82E-02
6.625	0.36489E 00 ± 0.11E-01	
6.750	0.47020E 00 ± 0.31E-01	0.45110E 00 ± 0.17E-01
6.875	0.63349E 00 ± 0.15E-01	
7.000	0.80551E 00 ± 0.17E-01	0.76504E 00 ± 0.17E-01
7.250	0.13470E 01 ± 0.27E-01	0.12255E 01 ± 0.30E-01
7.500	0.22043E 01 ± 0.44E-01	0.19126E 01 ± 0.51E-01
7.750	0.36180E 01 ± 0.72E-01	0.30204E 01 ± 0.66E-01
8.000	0.54155E 01 ± 0.11E 00	0.45560E 01 ± 0.91E-01
8.250	0.80080E 01 ± 0.16E 00	0.67132E 01 ± 0.15E 00
8.500	0.11633E 02 ± 0.23E 00	0.10480E 02 ± 0.21E 00
8.750	0.16039E 02 ± 0.32E 00	0.14297E 02 ± 0.32E 00
9.000	0.22701E 02 ± 0.45E 00	0.20533E 02 ± 0.41E 00
9.250	0.31335E 02 ± 0.63E 00	0.28084E 02 ± 0.56E 00
9.500	0.41102E 02 ± 0.82E 00	0.36917E 02 ± 0.74E 00
9.750	0.52317E 02 ± 0.10E 01	0.47415E 02 ± 0.95E 00
10.000	0.66879E 02 ± 0.13E 01	0.63138E 02 ± 0.13E 01
10.250	0.81803E 02 ± 0.16E 01	0.77380E 02 ± 0.15E 01
10.500	0.10027E 03 ± 0.20E 01	0.94068E 02 ± 0.19E 01
10.750	0.12004E 03 ± 0.24E 01	0.11357E 03 ± 0.23E 01
11.000	0.13737E 03 ± 0.27E 01	0.13481E 03 ± 0.27E 01
11.250	0.16255E 03 ± 0.33E 01	0.15584E 03 ± 0.31E 01
11.500	0.18790E 03 ± 0.38E 01	0.18182E 03 ± 0.36E 01
11.750	0.21258E 03 ± 0.43E 01	0.20833E 03 ± 0.42E 01
12.000	0.23745E 03 ± 0.47E 01	0.23208E 03 ± 0.46E 01
12.250	0.27237E 03 ± 0.54E 01	0.26403E 03 ± 0.53E 01

TABLE IV
(continued)
Total Fission Cross Sections

Proton Energy (MeV)	^{233}U + p Cross Section (mb)	^{234}U + p Cross Section (mb)
12.500	0.30098E 03 ± 0.60E 01	0.29321E 03 ± 0.59E 01
12.750	0.33620E 03 ± 0.67E 01	0.32851E 03 ± 0.66E 01
13.000	0.36547E 03 ± 0.73E 01	0.35577E 03 ± 0.71E 01
13.250	0.40008E 03 ± 0.80E 01	0.39213E 03 ± 0.78E 01
13.500	0.43218E 03 ± 0.86E 01	0.42393E 03 ± 0.85E 01
13.750	0.47492E 03 ± 0.95E 01	0.45940E 03 ± 0.92E 01
14.000	0.50692E 03 ± 0.10E 02	0.49660E 03 ± 0.99E 01
14.250	0.53970E 03 ± 0.11E 02	0.55193E 03 ± 0.11E 02
14.500	0.57362E 03 ± 0.11E 02	0.57155E 03 ± 0.11E 02
14.750	0.61409E 03 ± 0.12E 02	0.59559E 03 ± 0.12E 02
15.000	0.64624E 03 ± 0.13E 02	0.62897E 03 ± 0.13E 02
15.250	0.68028E 03 ± 0.14E 02	0.66267E 03 ± 0.13E 02
15.500	0.72166E 03 ± 0.14E 02	0.69995E 03 ± 0.14E 02
15.750	0.74707E 03 ± 0.15E 02	0.70596E 03 ± 0.14E 02
16.000	0.00000E 00 ± 0.00E 00	0.75016E 03 ± 0.15E 02
17.000	0.91235E 03 ± 0.18E 02	0.86058E 03 ± 0.17E 02
17.250	0.92427E 03 ± 0.18E 02	0.89273E 03 ± 0.18E 02
17.500	0.95283E 03 ± 0.19E 02	0.90432E 03 ± 0.18E 02
17.750	0.97816E 03 ± 0.20E 02	0.93676E 03 ± 0.19E 02
18.000	0.10041E 04 ± 0.20E 02	0.97220E 03 ± 0.19E 02
18.250	0.10084E 04 ± 0.20E 02	0.97970E 03 ± 0.20E 02
18.500	0.10223E 04 ± 0.20E 02	0.10101E 04 ± 0.20E 02
18.750	0.10712E 04 ± 0.21E 02	0.10331E 04 ± 0.21E 02
19.000	0.10900E 04 ± 0.22E 02	0.10681E 04 ± 0.21E 02
19.250	0.11130E 04 ± 0.22E 02	0.10791E 04 ± 0.22E 02
19.500	0.11361E 04 ± 0.23E 02	0.10939E 04 ± 0.22E 02
19.750	0.11598E 04 ± 0.23E 02	0.10999E 04 ± 0.22E 02
20.000	0.11762E 04 ± 0.24E 02	0.11370E 04 ± 0.23E 02
20.250	0.11902E 04 ± 0.24E 02	0.11440E 04 ± 0.23E 02
20.500	0.12151E 04 ± 0.24E 02	0.11603E 04 ± 0.23E 02
20.750	0.12216E 04 ± 0.24E 02	0.11905E 04 ± 0.24E 02
21.000	0.12512E 04 ± 0.25E 02	0.11843E 04 ± 0.24E 02
21.250	0.12563E 04 ± 0.25E 02	0.11956E 04 ± 0.24E 02
21.500	0.12626E 04 ± 0.25E 02	0.12050E 04 ± 0.24E 02
21.750	0.12793E 04 ± 0.26E 02	0.12080E 04 ± 0.24E 02
22.000	0.13156E 04 ± 0.26E 02	0.12539E 04 ± 0.25E 02
22.250	0.13157E 04 ± 0.26E 02	0.12325E 04 ± 0.25E 02
22.500	0.13272E 04 ± 0.27E 02	0.12828E 04 ± 0.26E 02
22.750	0.13339E 04 ± 0.27E 02	0.12734E 04 ± 0.25E 02
23.000	0.13694E 04 ± 0.27E 02	0.12918E 04 ± 0.26E 02

TABLE IV
(continued)
Total Fission Cross Sections

Proton Energy (MeV)	^{233}U + p Cross Section (mb)	^{234}U + p Cross Section (mb)
23.250	0.13790E 04 ± 0.28E 02	0.12930E 04 ± 0.26E 02
23.500	0.13680E 04 ± 0.27E 02	0.13739E 04 ± 0.27E 02
23.750	0.13814E 04 ± 0.28E 02	0.13176E 04 ± 0.26E 02
24.000	0.14144E 04 ± 0.28E 02	0.13805E 04 ± 0.28E 02
24.250	0.14207E 04 ± 0.28E 02	0.13506E 04 ± 0.27E 02
24.500	0.14362E 04 ± 0.29E 02	0.13923E 04 ± 0.28E 02
24.750	0.14674E 04 ± 0.29E 02	0.13909E 04 ± 0.28E 02
25.000	0.14679E 04 ± 0.29E 02	0.14252E 04 ± 0.29E 02
25.250	0.14655E 04 ± 0.29E 02	0.14393E 04 ± 0.29E 02
25.500	0.14835E 04 ± 0.30E 02	0.14558E 04 ± 0.29E 02
25.750	0.15147E 04 ± 0.30E 02	0.14646E 04 ± 0.29E 02
26.000	0.15267E 04 ± 0.31E 02	0.14985E 04 ± 0.30E 02
26.250	0.15320E 04 ± 0.31E 02	0.14954E 04 ± 0.30E 02
26.500	0.15678E 04 ± 0.31E 02	0.14802E 04 ± 0.30E 02
26.750	0.15518E 04 ± 0.31E 02	0.15171E 04 ± 0.30E 02
27.000	0.15850E 04 ± 0.32E 02	0.14817E 04 ± 0.30E 02
27.250	0.15891E 04 ± 0.32E 02	0.15101E 04 ± 0.30E 02
27.500	0.16190E 04 ± 0.32E 02	0.14803E 04 ± 0.30E 02
27.750	0.16024E 04 ± 0.32E 02	0.15331E 04 ± 0.31E 02
28.000	0.16020E 04 ± 0.32E 02	0.15278E 04 ± 0.31E 02
28.250	0.15951E 04 ± 0.32E 02	0.15408E 04 ± 0.31E 02
28.500	0.16512E 04 ± 0.33E 02	0.15571E 04 ± 0.31E 02
28.750	0.16424E 04 ± 0.33E 02	0.15847E 04 ± 0.32E 02
29.000	0.15952E 04 ± 0.32E 02	0.15243E 04 ± 0.30E 02
29.250	0.15937E 04 ± 0.32E 02	0.15243E 04 ± 0.30E 02
29.500	0.15978E 04 ± 0.32E 02	0.15574E 04 ± 0.31E 02
29.750	0.16274E 04 ± 0.33E 02	0.15499E 04 ± 0.31E 02
30.000	0.16122E 04 ± 0.32E 02	0.15312E 04 ± 0.31E 02

TABLE IV
(continued)
Total Fission Cross Sections

Proton Energy (MeV)	$^{235}U + p$ Cross Section (mb)	$^{236}U + p$ Cross Section (mb)
5.250	0.73827E-02 ± 0.57E-03	
5.500	0.16169E-01 ± 0.95E-03	0.16306E-01 ± 0.10E-02
5.750	0.34537E-01 ± 0.13E-02	0.30273E-01 ± 0.14E-02
6.000	0.68804E-01 ± 0.29E-02	0.66207E-01 ± 0.21E-02
6.250	0.12604E 00 ± 0.40E-02	0.11605E 00 ± 0.39E-02
6.500	0.23946E 00 ± 0.78E-02	0.21462E 00 ± 0.55E-02
6.750	0.42617E 00 ± 0.85E-02	0.35417E 00 ± 0.73E-02
7.000	0.77389E 00 ± 0.15E-01	0.59131E 00 ± 0.12E-01
7.250	0.13070E 01 ± 0.26E-01	0.93774E 00 ± 0.19E-01
7.500	0.21860E 01 ± 0.44E-01	0.15629E 01 ± 0.31E-01
7.750	0.34682E 01 ± 0.69E-01	0.25443E 01 ± 0.51E-01
8.000	0.53983E 01 ± 0.11E 00	0.40469E 01 ± 0.81E-01
8.250	0.80549E 01 ± 0.16E 00	0.63586E 01 ± 0.13E 00
8.500	0.11763E 02 ± 0.24E 00	0.96229E 01 ± 0.19E 00
8.750	0.16647E 02 ± 0.33E 00	0.14090E 02 ± 0.28E 00
9.000	0.22499E 02 ± 0.45E 00	0.19803E 02 ± 0.40E 00
9.250	0.30414E 02 ± 0.61E 00	0.27105E 02 ± 0.54E 00
9.500	0.39869E 02 ± 0.80E 00	0.37033E 02 ± 0.74E 00
9.750	0.51246E 02 ± 0.10E 01	0.47494E 02 ± 0.95E 00
10.000	0.63397E 02 ± 0.13E 01	0.61217E 02 ± 0.12E 01
10.250	0.78159E 02 ± 0.16E 01	0.75272E 02 ± 0.15E 01
10.500	0.96141E 02 ± 0.19E 01	0.91532E 02 ± 0.18E 01
10.750	0.11328E 03 ± 0.23E 01	0.10927E 03 ± 0.22E 01
11.000	0.13363E 03 ± 0.27E 01	0.12820E 03 ± 0.26E 01
11.250	0.15263E 03 ± 0.31E 01	0.14514E 03 ± 0.29E 01
11.500	0.17814E 03 ± 0.36E 01	0.17297E 03 ± 0.35E 01
11.750	0.20240E 03 ± 0.40E 01	0.20161E 03 ± 0.40E 01
12.000	0.22757E 03 ± 0.46E 01	0.22126E 03 ± 0.44E 01
12.250	0.25476E 03 ± 0.51E 01	0.24868E 03 ± 0.50E 01
12.500	0.28458E 03 ± 0.57E 01	0.27479E 03 ± 0.55E 01
12.750	0.31547E 03 ± 0.63E 01	0.30042E 03 ± 0.60E 01
13.000	0.34535E 03 ± 0.69E 01	0.33419E 03 ± 0.67E 01
13.250	0.37485E 03 ± 0.75E 01	0.35804E 03 ± 0.72E 01
13.500	0.40517E 03 ± 0.81E 01	0.39239E 03 ± 0.78E 01
13.750	0.43928E 03 ± 0.88E 01	0.43252E 03 ± 0.87E 01
14.000	0.47149E 03 ± 0.94E 01	0.46654E 03 ± 0.93E 01
14.250	0.50795E 03 ± 0.10E 02	0.51691E 03 ± 0.10E 02
14.500	0.54531E 03 ± 0.11E 02	0.54577E 03 ± 0.11E 02
14.750	0.57205E 03 ± 0.11E 02	0.57524E 03 ± 0.12E 02
15.000	0.61254E 03 ± 0.12E 02	0.62476E 03 ± 0.12E 02

TABLE IV
(continued)
Total Fission Cross Sections

Proton Energy (MeV)	$^{235}U + p$ Cross Section (mb)	$^{236}U + p$ Cross Section (mb)
15.250	0.63634E 03 ± 0.13E 02	0.68485E 03 ± 0.14E 02
15.500	0.68760E 03 ± 0.14E 02	0.70758E 03 ± 0.14E 02
15.750	0.71388E 03 ± 0.14E 02	0.74641E 03 ± 0.15E 02
16.000	0.75212E 03 ± 0.15E 02	0.75820E 03 ± 0.15E 02
16.250	0.77007E 03 ± 0.15E 02	0.79931E 03 ± 0.16E 02
16.500	0.81070E 03 ± 0.16E 02	0.83075E 03 ± 0.17E 02
16.750	0.86564E 03 ± 0.17E 02	0.88580E 03 ± 0.18E 02
17.000	0.88800E 03 ± 0.18E 02	0.90017E 03 ± 0.18E 02
17.250	0.93333E 03 ± 0.19E 02	0.93204E 03 ± 0.19E 02
17.500	0.95060E 03 ± 0.19E 02	0.95590E 03 ± 0.19E 02
17.750	0.98723E 03 ± 0.20E 02	0.98869E 03 ± 0.20E 02
18.000	0.10026E 04 ± 0.20E 02	0.99165E 03 ± 0.20E 02
18.250	0.10410E 04 ± 0.21E 02	0.10087E 04 ± 0.20E 02
18.500	0.10472E 04 ± 0.21E 02	0.10268E 04 ± 0.21E 02
18.750	0.10836E 04 ± 0.22E 02	0.10731E 04 ± 0.21E 02
19.000	0.10887E 04 ± 0.22E 02	0.10797E 04 ± 0.22E 02
19.250	0.11250E 04 ± 0.22E 02	0.11062E 04 ± 0.22E 02
19.500	0.11249E 04 ± 0.22E 02	0.11239E 04 ± 0.22E 02
19.750	0.11567E 04 ± 0.23E 02	0.11579E 04 ± 0.23E 02
20.000	0.11643E 04 ± 0.23E 02	0.11537E 04 ± 0.23E 02
20.250	0.11959E 04 ± 0.24E 02	0.11802E 04 ± 0.24E 02
20.500	0.12057E 04 ± 0.24E 02	0.11997E 04 ± 0.24E 02
20.750	0.12329E 04 ± 0.25E 02	0.12126E 04 ± 0.24E 02
21.000	0.12506E 04 ± 0.25E 02	0.12231E 04 ± 0.24E 02
21.250	0.12702E 04 ± 0.25E 02	0.12311E 04 ± 0.25E 02
21.500	0.12835E 04 ± 0.26E 02	0.12146E 04 ± 0.24E 02
21.750	0.13011E 04 ± 0.26E 02	0.12546E 04 ± 0.25E 02
22.000	0.13079E 04 ± 0.26E 02	0.12648E 04 ± 0.25E 02
22.250	0.13294E 04 ± 0.27E 02	0.12809E 04 ± 0.26E 02
22.500	0.13456E 04 ± 0.27E 02	0.13059E 04 ± 0.26E 02
22.750	0.13620E 04 ± 0.27E 02	0.13213E 04 ± 0.26E 02
23.000	0.13809E 04 ± 0.28E 02	0.13524E 04 ± 0.27E 02
23.250	0.13910E 04 ± 0.28E 02	0.13578E 04 ± 0.27E 02
23.500	0.14017E 04 ± 0.28E 02	0.13386E 04 ± 0.27E 02
23.750	0.14258E 04 ± 0.29E 02	0.13457E 04 ± 0.27E 02
24.000	0.14402E 04 ± 0.29E 02	0.13788E 04 ± 0.28E 02
24.250	0.14549E 04 ± 0.29E 02	0.13889E 04 ± 0.28E 02
24.500	0.14593E 04 ± 0.29E 02	0.14183E 04 ± 0.28E 02
24.750	0.14643E 04 ± 0.29E 02	0.14083E 04 ± 0.28E 02
25.000	0.14910E 04 ± 0.30E 02	0.14174E 04 ± 0.28E 02

TABLE IV
(continued)
Total Fission Cross Sections

Proton Energy (MeV)	^{235}U + p Cross Section (mb)	^{236}U + p Cross Section (mb)
25.250	0.15066E 04 ± 0.30E 02	0.14437E 04 ± 0.29E 02
25.500	0.15209E 04 ± 0.30E 02	0.14527E 04 ± 0.29E 02
25.750	0.15249E 04 ± 0.30E 02	0.14632E 04 ± 0.29E 02
26.000	0.15486E 04 ± 0.31E 02	0.14769E 04 ± 0.30E 02
26.250	0.15423E 04 ± 0.31E 02	0.14601E 04 ± 0.29E 02
26.500	0.15508E 04 ± 0.31E 02	0.14630E 04 ± 0.29E 02
26.750	0.15559E 04 ± 0.31E 02	0.14965E 04 ± 0.30E 02
27.000	0.15854E 04 ± 0.32E 02	0.15422E 04 ± 0.31E 02
27.250	0.15712E 04 ± 0.31E 02	0.15353E 04 ± 0.31E 02
27.500	0.15874E 04 ± 0.32E 02	0.15381E 04 ± 0.31E 02
27.750	0.16065E 04 ± 0.32E 02	0.15228E 04 ± 0.30E 02
28.000	0.16273E 04 ± 0.33E 02	0.15871E 04 ± 0.32E 02
28.250	0.16260E 04 ± 0.33E 02	0.15606E 04 ± 0.31E 02
28.500	0.16374E 04 ± 0.33E 02	0.15646E 04 ± 0.31E 02
28.750	0.16415E 04 ± 0.33E 02	0.16409E 04 ± 0.33E 02
29.000	0.15869E 04 ± 0.32E 02	0.15533E 04 ± 0.31E 02
29.250	0.15903E 04 ± 0.32E 02	0.15654E 04 ± 0.31E 02
29.500	0.15936E 04 ± 0.32E 02	0.15789E 04 ± 0.32E 02
29.750	0.16080E 04 ± 0.32E 02	0.15843E 04 ± 0.32E 02
30.000	0.16024E 04 ± 0.32E 02	0.15438E 04 ± 0.31E 02
30.250		0.15725E 04 ± 0.31E 02
30.500		0.15521E 04 ± 0.31E 02
30.750		0.15598E 04 ± 0.31E 02
31.000		0.16054E 04 ± 0.32E 02

TABLE IV
(continued)
Total Fission Cross Sections

Proton Energy (MeV)	^{238}U + p Cross Section (mb)
5.500	0.11088E-01 ± 0.97E-03
5.625	0.15994E-01 ± 0.14E-02
5.750	0.25818E-01 ± 0.13E-02
6.000	0.53919E-01 ± 0.24E-02
6.250	0.98306E-01 ± 0.34E-02
6.500	0.16583E 00 ± 0.56E-02
6.750	0.28218E 00 ± 0.76E-02
7.000	0.51363E 00 ± 0.17E-01
7.250	0.83105E 00 ± 0.19E-01
7.500	0.14584E 01 ± 0.38E-01
7.750	0.24074E 01 ± 0.67E-01
8.000	0.39403E 01 ± 0.93E-01
8.250	0.60301E 01 ± 0.12E 00
8.500	0.93637E 01 ± 0.19E 00
8.750	0.13157E 02 ± 0.26E 00
9.000	0.18152E 02 ± 0.36E 00
9.250	0.25082E 02 ± 0.50E 00
9.500	0.33078E 02 ± 0.66E 00
9.750	0.42353E 02 ± 0.85E 00
10.000	0.53301E 02 ± 0.11E 01
10.250	0.64447E 02 ± 0.13E 01
10.500	0.78999E 02 ± 0.16E 01
10.750	0.93679E 02 ± 0.19E 01
11.000	0.11091E 03 ± 0.22E 01
11.250	0.13017E 03 ± 0.26E 01
11.500	0.14961E 03 ± 0.30E 01
11.750	0.17106E 03 ± 0.34E 01
12.000	0.19592E 03 ± 0.39E 01
12.250	0.22132E 03 ± 0.44E 01
12.500	0.24755E 03 ± 0.50E 01
12.750	0.27574E 03 ± 0.55E 01
13.000	0.30247E 03 ± 0.60E 01
13.250	0.34420E 03 ± 0.69E 01
13.500	0.38020E 03 ± 0.76E 01
13.750	0.41775E 03 ± 0.84E 01
14.000	0.45987E 03 ± 0.92E 01
14.250	0.49934E 03 ± 0.10E 02
14.500	0.54839E 03 ± 0.11E 02
14.750	0.58869E 03 ± 0.12E 02
15.000	0.63766E 03 ± 0.13E 02

TABLE IV
(continued)
Total Fission Cross Sections

Proton Energy (MeV)	^{238}U + p Cross Section (mb)
15.250	0.66808E 03 ± 0.13E 02
15.500	0.69378E 03 ± 0.14E 02
15.750	0.73191E 03 ± 0.15E 02
16.000	0.76491E 03 ± 0.15E 02
16.250	0.78591E 03 ± 0.16E 02
16.500	0.81661E 03 ± 0.16E 02
16.750	0.81861E 03 ± 0.16E 02
17.000	0.86657E 03 ± 0.17E 02
17.250	0.88891E 03 ± 0.18E 02
17.500	0.90875E 03 ± 0.18E 02
17.750	0.96987E 03 ± 0.19E 02
18.000	0.97154E 03 ± 0.19E 02
18.250	0.97735E 03 ± 0.20E 02
18.500	0.99988E 03 ± 0.20E 02
18.750	0.10168E 04 ± 0.20E 02
19.000	0.10170E 04 ± 0.20E 02
19.250	0.10492E 04 ± 0.21E 02
19.500	0.10725E 04 ± 0.21E 02
19.750	0.10647E 04 ± 0.21E 02
20.000	0.10977E 04 ± 0.22E 02
20.250	0.11196E 04 ± 0.22E 02
20.500	0.11171E 04 ± 0.22E 02
20.750	0.11387E 04 ± 0.23E 02
21.000	0.11605E 04 ± 0.23E 02
21.250	0.11775E 04 ± 0.24E 02
21.500	0.12064E 04 ± 0.24E 02
21.750	0.12281E 04 ± 0.25E 02
22.000	0.12411E 04 ± 0.25E 02
22.250	0.12522E 04 ± 0.25E 02
22.500	0.12814E 04 ± 0.26E 02
22.750	0.12992E 04 ± 0.26E 02
23.000	0.13207E 04 ± 0.26E 02
23.250	0.13447E 04 ± 0.27E 02
23.500	0.13520E 04 ± 0.27E 02
23.750	0.13645E 04 ± 0.27E 02
24.000	0.13783E 04 ± 0.28E 02
24.250	0.13971E 04 ± 0.28E 02
24.500	0.14074E 04 ± 0.28E 02
24.750	0.14220E 04 ± 0.28E 02
25.000	0.14221E 04 ± 0.28E 02

TABLE IV
(continued)
Total Fission Cross Sections

Proton Energy (MeV)	^{238}U + p Cross Section (mb)
25.250	0.14555E 04 ± 0.29E 02
25.500	0.14560E 04 ± 0.29E 02
25.750	0.14588E 04 ± 0.29E 02
26.000	0.14664E 04 ± 0.29E 02
26.250	0.14863E 04 ± 0.30E 02
26.500	0.14802E 04 ± 0.30E 02
26.750	0.14987E 04 ± 0.30E 02
27.000	0.14981E 04 ± 0.30E 02
27.250	0.15196E 04 ± 0.30E 02
27.500	0.15237E 04 ± 0.30E 02
27.750	0.15329E 04 ± 0.31E 02
28.000	0.15498E 04 ± 0.31E 02
28.250	0.15318E 04 ± 0.31E 02
28.500	0.15476E 04 ± 0.31E 02
28.750	0.15685E 04 ± 0.31E 02
29.000	0.15214E 04 ± 0.30E 02
29.250	0.15273E 04 ± 0.31E 02
29.500	0.15322E 04 ± 0.31E 02
29.750	0.15264E 04 ± 0.31E 02
30.000	0.15362E 04 ± 0.31E 02
30.250	0.15378E 04 ± 0.31E 02
30.500	0.15773E 04 ± 0.32E 02
30.750	0.15758E 04 ± 0.32E 02
31.000	0.15906E 04 ± 0.32E 02

Figure 8. Final proton induced total fission cross sections as functions of excitation energy in the initial compound nucleus.

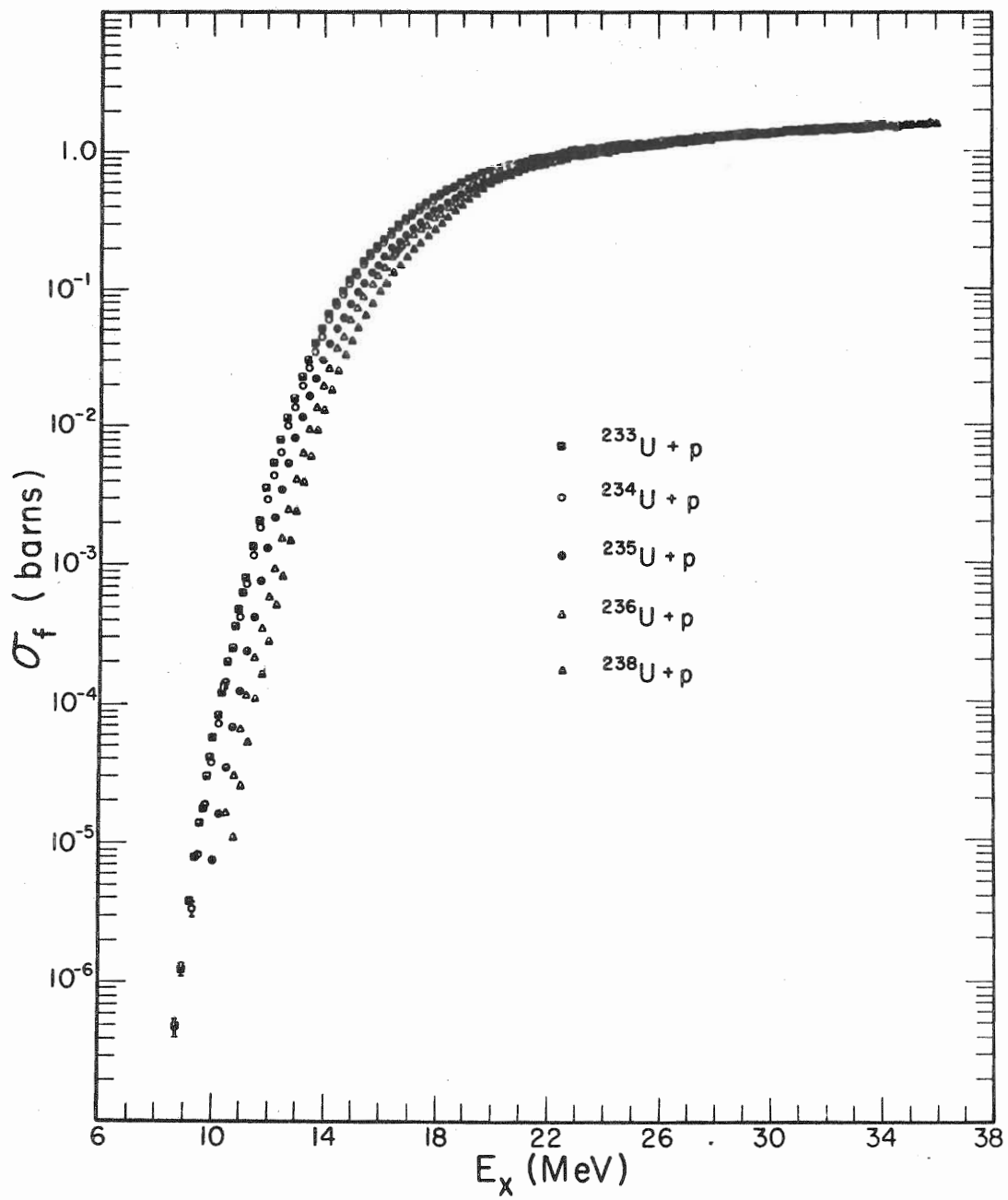
1.0
10^{-1}
10^{-2}
10^{-3}
10^{-4}
10^{-5}
10^{-6}
σ_f (barns)
6
10
14
18
22
26
30
34
38
E_x (MeV)
$^{233}U + p$
$^{234}U + p$
$^{235}U + p$
$^{236}U + p$
$^{238}U + p$

Figure 9. Expanded lower energy region of Figure 8.

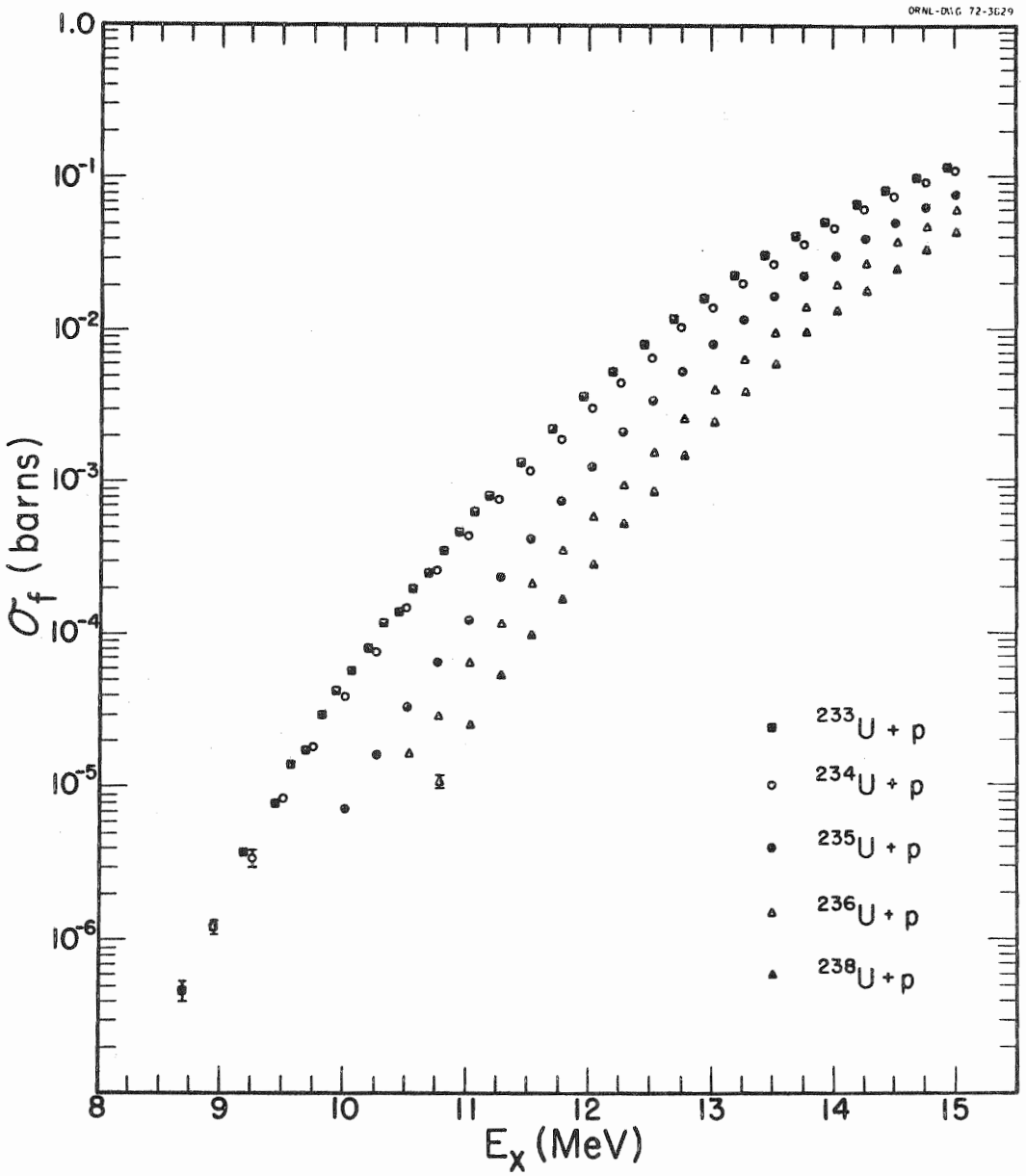
ORNL-DWG 72-3629
1.0
10^{-1}
10^{-2}
10^{-3}
10^{-4}
10^{-5}
10^{-6}
σ_f (barns)
8
9
10
11
12
13
14
15
E_x (MeV)
$^{233}U + p$
$^{234}U + p$
$^{235}U + p$
$^{236}U + p$
$^{238}U + p$

The final step in the data reduction removes these obvious effects in a manner similar to the "Ratio to Rutherford" technique used to remove Coulomb scattering effects in ordinary charged particle angular distributions. The fission cross section is divided by the total reaction cross section calculated from the optical model. Because of the large energy range, energy dependent optical model parameters are required. The parameter formulas of Becchetti and Greenlees[5] were chosen for this step as they are based on a comprehensive review of the literature. Further discussion of the choice of parameters can be found in Appendix C.

Figure 10 shows the result of this technique. These data indicate the total probability that the compound nucleus will fission either directly or following the evaporation of one or more neutrons. The data, so reduced, exhibits definite structure: steps which can be correlated to the onset of second and third chance fission appear.

The goal of analysis from this point on is to resolve each curve of Figure 10 into its individual components representing at least three different fissioning nuclei. The proposed model for this reduction is discussed in the next section.

Figure 10. The total experimental fission probabilities based upon a reaction cross section calculated with the optical model.

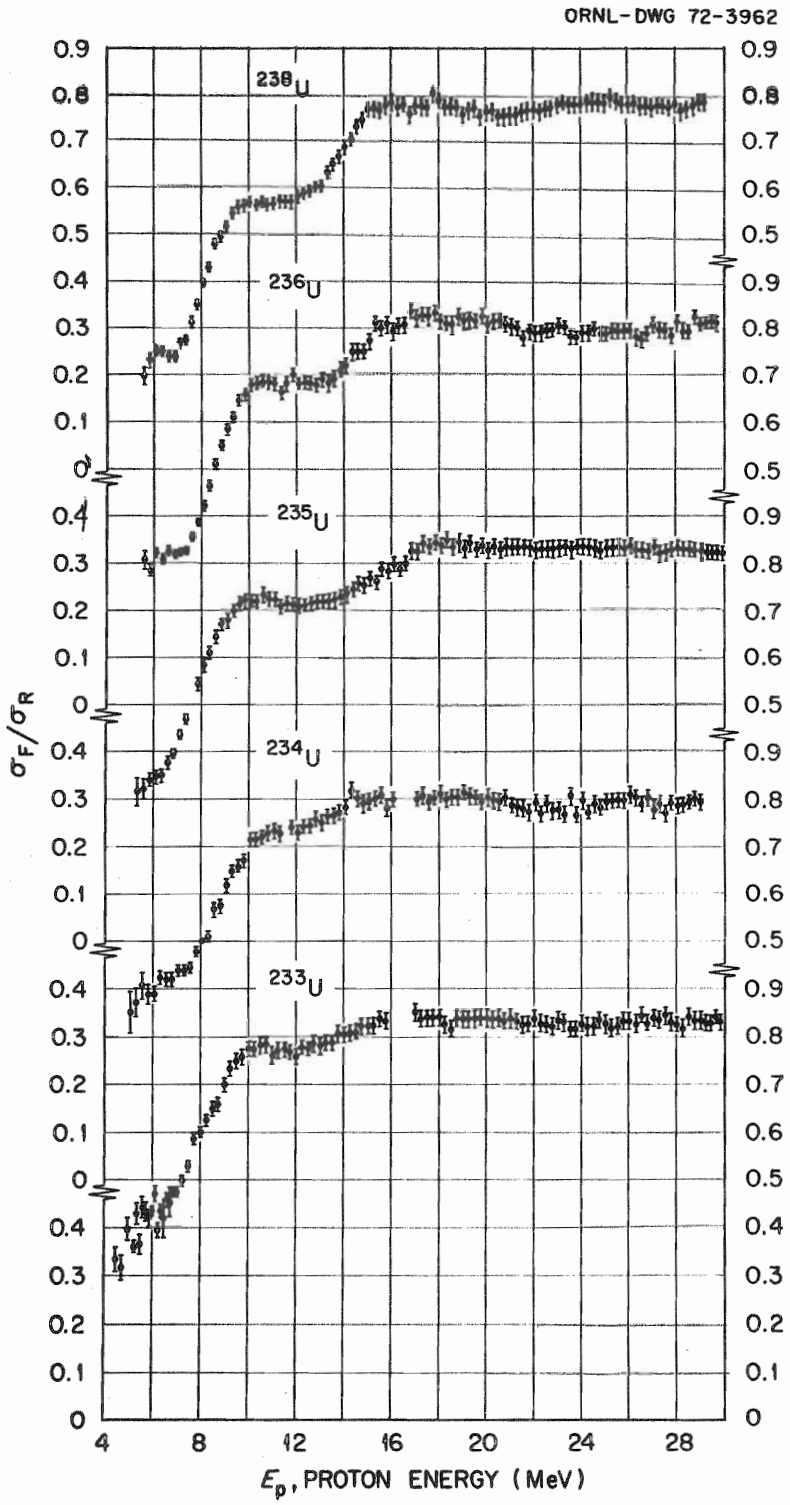
ORNL-DWG 72-3962
238U
236U
235U
234U
233U
σF/σR
Ep, PROTON ENERGY (MeV)
4
8
12
16
20
24
28

Chapter III
THEORETICAL MODEL

The analysis of the present experimental data requires essentially two aspects of nuclear reaction theory; one is the theory describing the formation of the compound nucleus, and the other is the theory describing the decay of the compound nucleus following its formation. We will rely heavily on the current description of the optical model for a picture of the formation process. For the decay process we will use a statistical model first proposed by Bohr and Wheeler[6] and later expanded by Huizenga and Vandenbosch.[7]

A. Compound Nucleus Formation

According to the optical model the interaction between an incident particle and a nucleus can be treated as that of a wave packet incident on a complex potential well. The reaction cross section is the ratio of the flux absorbed by the well to the incident flux per unit area.

The parameters describing the complex potential have generally been obtained by fitting the diffraction patterns of elastic scattering data for energies above the Coulomb barrier. Several reviews[5,8,9] of these parameters conclude that they are A, Z, and energy dependent. While these parameters give good agreement with data above the Coulomb barrier, extrapolation to energies below the barrier is questionable.

In the present experiments we are able to place an additional constraint on the reaction cross sections calculated with these parameters. If we assume that the optical model reaction cross section, σ_R, calculated with these standard parameters, gives a good representation of the cross section for compound nucleus formation, σ_c, at proton energies 5-30 MeV, then the first chance fission probabilities from $E_p \approx 5$-7 MeV are always considerably smaller than predicted on the basis of empirical systematics.[4] Yet the same fission probabilities implied by the cross section increase at the second chance fission threshold tend to be too large by the same criterion. Consequently the fission probabilities for neighboring targets are not consistent with each other and with the requirement that the fission probability of a given isotope should have a definite value at a given excitation energy. This indicates a failure of the energy dependence of the optical model parameters for the nuclei studied. The discrepancy can be removed by assuming that the cross section for compound nucleus formation at energies well below the Coulomb barrier is considerably smaller than the optical model reaction cross section calculated with standard parameter sets. Similar conclusions have been reached in an analysis of low-energy (p,n) cross sections for medium mass nuclei.[10]

The exact functional form of the required correction to the optical model reaction cross section could not be determined. However the correction must be a smooth function of incident proton energy, must have its maximum effect at energies well below the Coulomb barrier, and finally must approximately vanish for those energies well above the barrier for which the optical model parameters should be accurately determined. A function satisfying these criteria is given by

$$\frac{\sigma_c}{\sigma_R} = a + \frac{b}{E_p} + \frac{c}{E_p^2} = f_c(E_p)$$

In this equation initial values for the coefficients were

estimated by assuming that Γ_n/Γ_f does not change rapidly with nuclear excitation energy for energies well above the fission barrier. Estimates were obtained on this basis for each of the five yield curves. The final coefficients used were the same for all target nuclei and are the result of small changes made to improve the overall fit to the data.

B. Statistical Decay Model.

The model on which statistical calculations were based is illustrated in Figure 11. An initial compound nucleus is formed at excitation energy E_x^{A+1}. This nucleus may decay via an open neutron channel to residual nucleus A; alternatively, the initial compound nucleus may decay to saddle point states E_s^{A+1} and subsequently fission. The competition between neutron emission and fission in the decay of the excited compound nucleus is influenced by the level densities available to the respective decay channels.

The actual form of the nuclear level density remains a matter of conjecture. Various expressions have been proposed[7 11 12] and debated; however, most fission excitation functions have been analyzed using either the Fermi gas or constant temperature level density formalism. We have chosen the level density scheme of Gilbert and Cameron[11] for this thesis since it includes both pairing and ground state shell corrections and since parameters for the stable ground state deformation have been deduced by comparison with a variety of experimental data for nuclei throughout the periodic table.

In particular, the level densities used are:

$$\rho(E) = \begin{cases} \rho_1(E) = \frac{1}{T}\exp\left(\frac{E-E_0}{T}\right)\frac{1}{2\sigma^2} & \text{for } E < E_x \\ \rho_2(E) = \frac{\exp\left(2\sqrt{aU}\right)}{12\,a^{1/4}\,U^{5/4}}\,\frac{1}{2\sqrt{2}\,\sigma^3} & \text{for } E > E_x \end{cases}$$

where

$$E_x = U_x + P(Z) + P(N) \qquad \text{(MeV)}$$

$$U_x = 2.5 + 150/A \qquad \text{(MeV)}$$

Figure 11. Basic idea of the decay model.

E_x^{A+1} = excitation energy in the compound nucleus.

E_x^{A} = excitation energy in the residual nucleus (A).

B_n^{A+1} = neutron binding energy in (A+1)

E_f^{A+1} = fission barrier height in (A+1)

E_s^{A+1} = saddle point energy state.

ε_n = kinetic energy of the evaporated neutron

$E_{max} = E_x^{A+1} - B_n^{A+1}$

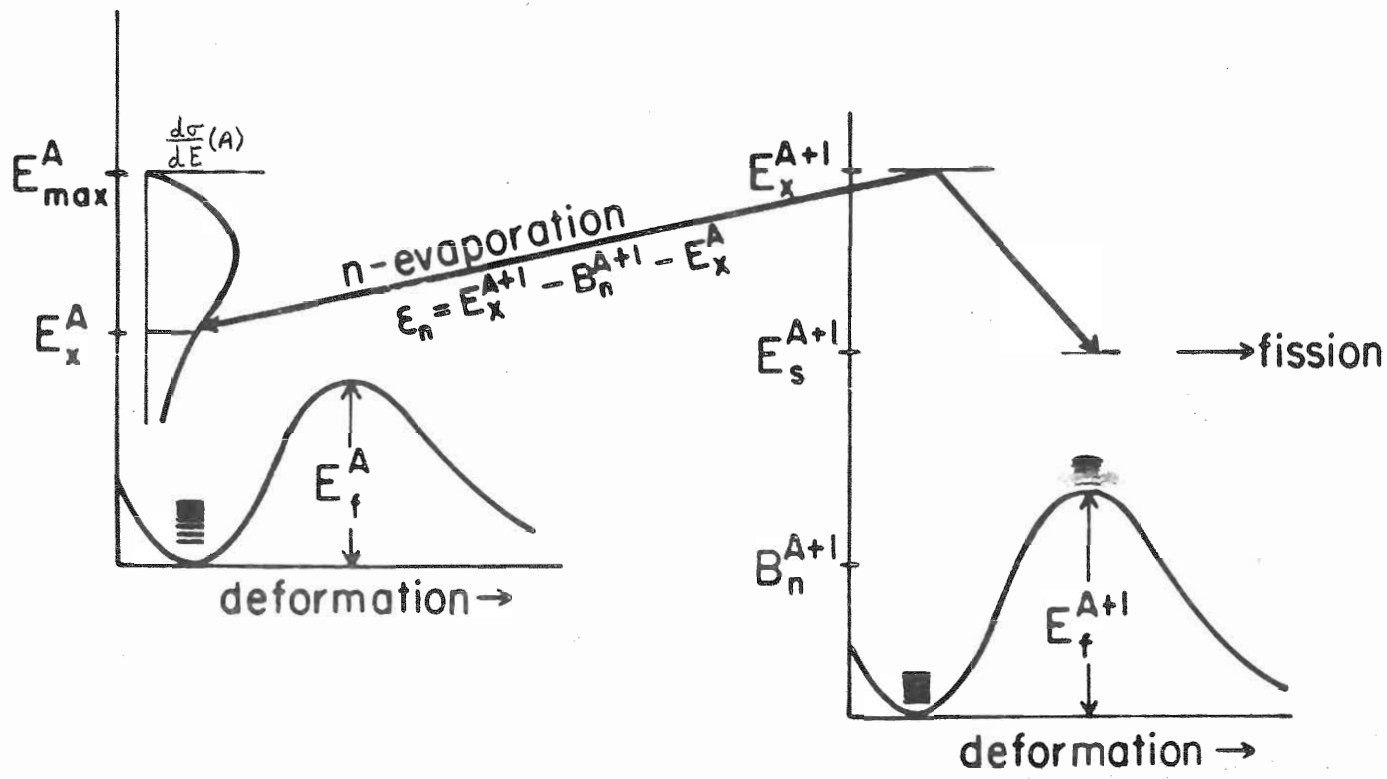

RESIDUAL NUCLEUS A

COMPOUND NUCLEUS A+1

P(Z) and P(N) being pairing energies empirically determined by Gilbert and Cameron.[11] The value of the nuclear temperature T and the parameter E_0 are determined by requiring that ρ_1 and ρ_2 be matched in value and slope at the transition energy E_x. Other parameters were determined by

$$U = E - P(Z) - P(N) \qquad \text{(MeV)}$$

$$\sigma^2 = \begin{cases} 0.0888\,(a\,U_x)^{1/2} A^{2/3} , & \text{for } E < E_x \\ 0.0888\,(a\,U)^{1/2} A^{2/3} , & \text{for } E > E_x \end{cases}$$

$$a/A = 0.00917\,S + 0.120 \qquad \text{(MeV}^{-1}\text{)}$$

$$S = S(Z) + S(N)$$

where S(Z) and S(N) are shell corrections determined empirically from comparison with experimental data.[11] This formulation is for the spin zero case. The effects of higher spins are discussed in Appendix D.

The above level density formulation is for the ground state deformation which influences particle emission. It is stretching a point to think that the level density of the highly deformed nucleus about to fission can be expressed by the same prescription as that of the ground state level density. Since shell corrections have a strong influence on the fission barrier characteristics it is natural to let the level density parameter a be a function of deformation. Thus for the saddle point level densities we determine a_f by $a_f/a_m = \alpha(A)$. This is in agreement with heavy ion induced fission[13] and shape isomer[14] results. Apart from this assumption, for lack of better information the same prescription is followed for the calculation of the saddle point level densities as that for the ground state deformation.

1. The fission channel.

The probability for a compound nucleus A+1 with excitation energy E_x^{A+1} to undergo fission is the ratio of the partial decay width, Γ_f , to the total decay width Γ_T . We define the saddle point as that deformation beyond which fission is assured. The fission process is visualized as first decaying to the deformed saddle point state of intrinsic excitation energy E_S^{A+1} , and then completing the splitting process.

For this thesis the deformation barrier is taken to be a single inverted harmonic oscillator with circular frequency ω_f . Hill and Wheeler[15] derived the expression for the transmission through such a barrier:

$$T_f(E_x, E_s) = \left\{ 1.0 + exp\left(\frac{E_s - E_x}{\hbar \omega_f} \right) \right\}^{-1} .$$

The total decay width for fission is given by

$$\Gamma_f^{A+1} = \frac{1}{2\pi \rho(E_x^{A+1})} \int_{E_f^{A+1}}^{\infty} T_f(E_x^{A+1}, E_s^{A+1}) \, \rho(E_x^{A+1} - E_s^{A+1}) \, d E_s^{A+1}$$

where T_f is the barrier penetration transmission via saddle point energy E_S^{A+1} , $\rho(E_x^{A+1})$ is the level density of the compound nucleus excited to E_x^{A+1} , $\rho(E_x^{A+1} - E_S^{A+1})$ is the level density at the saddle point configuration, and the integration is over all available saddle point energies.

2. The neutron channel.

The expression for the partial decay width for the neutron evaporation from a nucleus (A+1) of excitation energy E_x^{A+1} was first derived by Weisskopff:[16]

$$\Gamma_m^{A+1} = \frac{1}{2\pi\rho(E_x^{A+1})} \int_0^{E_x^{A+1} - B_m^{A+1}} T_m(\varepsilon_m)\, \rho(E_x^A)\, d\varepsilon_m$$

where $T_m(\varepsilon_m) = \frac{4 m_m}{\pi \hbar^2} \varepsilon_m \sigma_m(\varepsilon_m)$

m_m = mass of the neutron

$\sigma_m(\varepsilon_m)$ = the reverse process cross section

$\rho(E_x^{A+1})$ = excited compound nucleus level density

$\rho(E_x^A)$ = level density of the residual nucleus

$\varepsilon_m = E_x^{A+1} - B_m^{A+1} - E_x^A$.

The inverse cross section σ_m is that between a neutron of kinetic energy ε_m and a nucleus in an excited state. Since information about such cross sections is not available, the ground state cross sections are used as calculated by the optical model.

The probabilities for the two primary decay channels are:

$$G_m = \frac{\Gamma_m}{\Gamma_T} \quad \text{and} \quad G_f = \frac{\Gamma_f}{\Gamma_T} .$$

The total decay width Γ_T is the sum of all partial widths for all decay channels:

$$\Gamma_T = \Gamma_f + \Gamma_m + \Gamma_\gamma + \Gamma_p + \cdots .$$

We neglected Γ_p and other charged particle decay widths. Γ_γ is taken to be a constant 0.03 eV.[17]

The cross section for first chance fission is then the probability for first chance fission, G_f^1, times the compound nucleus formation cross section:

$$\sigma_f^1(E_x^{A+1}) = G_f^1(E_x^{A+1})\, \sigma_c(E_x^{A+1}) .$$

3. Second chance fission.

A neutron must be evaporated for a nucleus to undergo second chance fission. Thus the excitation energy E_x^{A+1} must satisfy the inequality

$$E_x^{A+1} > B_m^{A+1}$$

where B_m^{A+1} is the neutron binding energy. When neutron evaporation does occur the residual nucleus is left with a statistical distribution of energies. Let us define $P(E_x^A)$ to be the probability that a neutron has evaporated with energy

$$\varepsilon_m = E_x^{A+1} - B_m^{A+1} - E_x^A$$

leaving the nucleus A with energy E_x^A . In particular

$$P(E_x^A) = \frac{1}{2\pi\rho(E_x^{A+1})} T_m(\varepsilon_m)\,\rho(E_x^A) .$$

The probability for the residual nucleus to then undergo fission is $G_f(E_x^A)$. These two probabilities are independent but sequential. Thus the probability for the compound nucleus to decay via n-emission of energy ε_m and fission is the product

$$P(E_x^A)\,G_f(E_x^A) .$$

Therefore the probability for second chance fission, G_f^2 , is the integral of the above product over the energy distribution of the residual nucleus A:

$$G_f^2(E_x^{A+1}) = \int_0^{E_x^{A+1} - B_m^{A+1}} P(E_x^A)\,G_f(E_x^A)\,d(E_x^A) .$$

The cross section for second chance fission is

$$\sigma_f^2(E_x^{A+1}) = G_f^2(E_x^{A+1})\,\sigma_c(E_x^{A+1}) .$$

The total fission cross section below the onset of third chance is

$$\sigma_F(E_x^{A+1}) = \sigma_f^1(E_x^{A+1}) + \sigma_f^2(E_x^{A+1}) .$$

4. Third chance fission.

Two neutrons must be evaporated for third chance fission to occur. The energy E_x^{A+1} must satisfy the inequality

$$E_x^{A+1} > B_m^{A+1} + B_m^{A} \quad .$$

Let $P(E_x^A)$ be the probability of neutron evaporation leaving nucleus A with excitation energy E_x^A as defined in the previous section. Moreover let $P(E_x^{A-1})$ be the probability that the second neutron evaporated with energy

$$\varepsilon_m = E_x^A - B_m^A - E_x^{A-1} \quad .$$

Then the probability that nucleus (A-1) will undergo fission after these two sequential evaporations is the product

$$P(E_x^A)\, P(E_x^{A-1})\, G_f(E_x^{A-1}) \quad .$$

The probability for third chance fission, G_f^3, is the double integral over the distribution of energies in the final nucleus (A-1), and over the distribution of energies in the intermediate nucleus (A):

$$G_f^3(E_x^{A+1}) = \int_0^{E_x^{A+1} - B_m^{A+1}} P(E_x^A) \int_0^{E_x^A - B_m^A} P(E_x^{A-1})\, G_f(E_x^{A-1})\, dE_x^{A-1}\, dE_x^A .$$

The cross section for third chance is

$$\sigma_f^3(E_x^{A+1}) = G_f^3(E_x^{A+1})\, \sigma_c(E_x^{A+1}) \quad .$$

Below the onset of fourth chance fission the total fission cross section is

$$\sigma_F(E_x^{A+1}) = \sigma_f^1(E_x^{A+1}) + \sigma_f^2(E_x^{A+1}) + \sigma_f^3(E_x^{A+1}) \quad .$$

This formalism can be extended to higher chance fission and in general

$$\sigma_F(E_x^{A+1}) = \sum_i \sigma_f^i(E_x^{A+1}) \quad .$$

Chapter IV
ANALYSIS RESULTS AND DISCUSSION

In order to obtain the desired information concerning the relevant fission to neutron emission branching ratios and the fission thresholds the analysis of the data relied heavily on two computer codes. The first, MERLIN, is a modification of the optical model code OPTICS which is unique in that it can be used with relatively small computers such as the DDP-224 at TUNL.[18] A second and larger code, PHROG, was written to perform those calculations relating to the decay of the excited compound nucleus using the formalism developed in Chapter III.

Figure 12 is a simplified layout of the calculation. MERLIN uses coefficients of the optical model parameter formulas of Appendix B as input data and calculates the reaction cross section for each energy step. These cross sections are then punched on cards for part of the input data required by PHROG. The latter code then modifies the reaction cross section to obtain a compound nucleus formation cross section. The remainder of the input data is read in and the code then proceeds with calculations describing the decay of the compound nucleus.

A nine point Gaussian quadrature was used to numerically evaluate the integrals needed for calculating the probabilities and cross sections for the compound nucleus (A+1) to undergo fission or to emit the first neutron leaving a residual nucleus with an energy distribution $\frac{d\sigma}{dE}(A)$. The probabilities and cross sections for the decay channels of nucleus (A) are obtained by similar integration techniques over the energy distribution $\frac{d\sigma}{dE}(A-1)$. The process is repeated for the nucleus (A-1). In

Figure 12. Simplified layout of the calculations. The solid lines represent the present status. Planned additions are indicated by dashed lines.

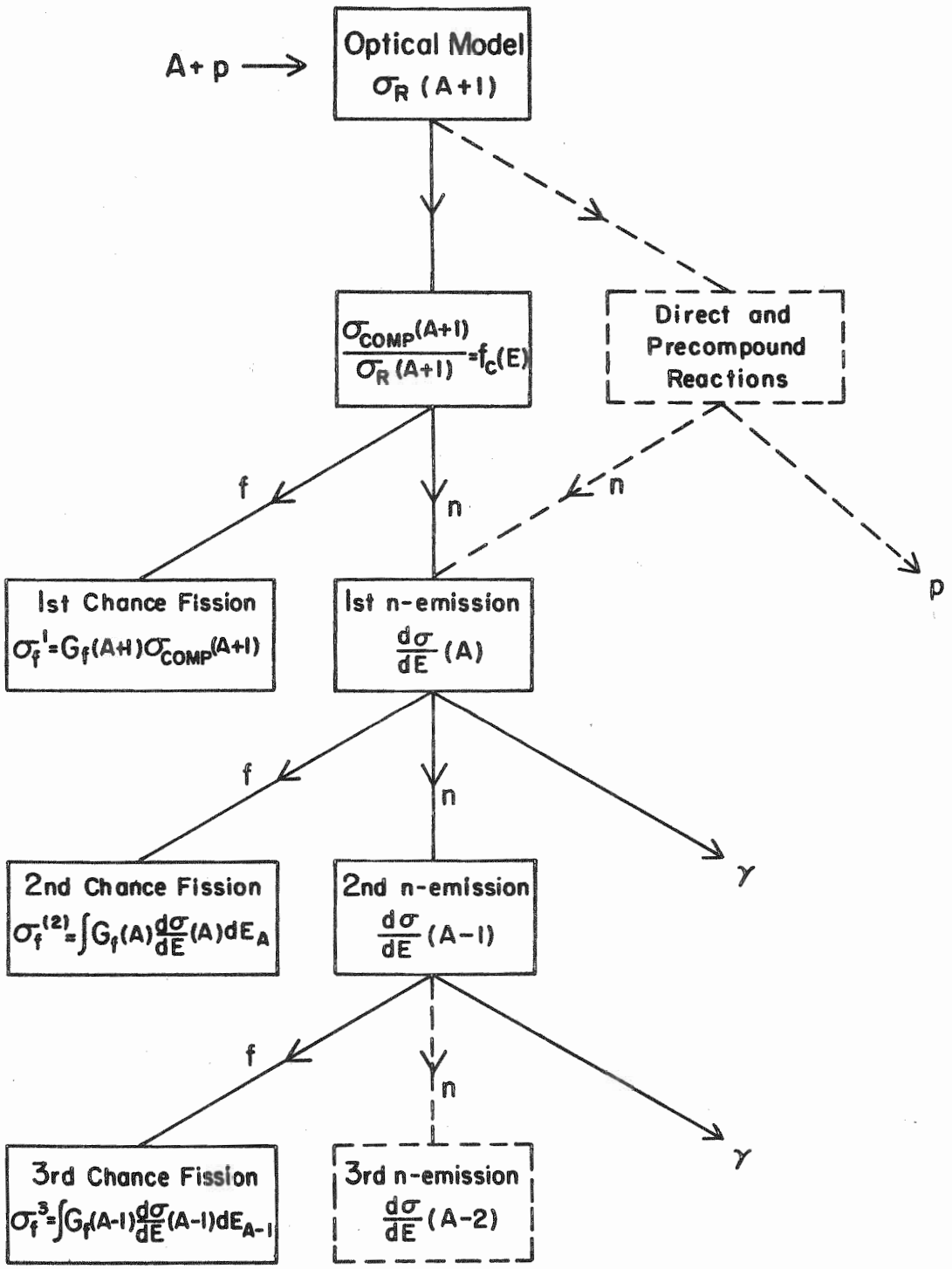
A+p
Optical Model
σ_R (A+1)
$\frac{\sigma_{COMP}(A+1)}{\sigma_R(A+1)} = f_c(E)$
Direct and Precompound Reactions
f
n
n
p
1st Chance Fission
$\sigma_f^1 = G_f(A+1)\sigma_{COMP}(A+1)$
1st n-emission
$\frac{d\sigma}{dE}(A)$
f
n
γ
2nd Chance Fission
$\sigma_f^{(2)} = \int G_f(A)\frac{d\sigma}{dE}(A)dE_A$
2nd n-emission
$\frac{d\sigma}{dE}(A-1)$
f
n
γ
3rd Chance Fission
$\sigma_f^3 = \int G_f(A-1)\frac{d\sigma}{dE}(A-1)dE_{A-1}$
3rd n-emission
$\frac{d\sigma}{dE}(A-2)$

this manner the contributions to the total fission cross section from first, second, and third chance fission are obtained.

Extensive testing of each subroutine in the computer codes were performed to insure computational accuracy. Whenever possible, tables were calculated and quadratic interpolation was used to evaluate the integrands in the numerical quadrature routines. Thus the amount of computer time used for integration evaluation was kept to a bare minimum: one minute with table interpolation as opposed to 30 minutes used by straight evaluation.

It should be noted that the analysis philosophy of these calculations is not to fit the details of the data. Instead the calculations attempt to reproduce the major features of the data by proceeding from certain fundamental assumptions. PHROG is not a data fitting program in the sense of searching for a minimum χ^2 by freely varying relevant parameters.

The assumptions basic to the analysis are: (1) that with relatively minor adjustments, the optical model correctly describes the compound nucleus formation cross section, (2) that the formalism developed by Weisskopf[16] and Bohr and Wheeler[6] correctly describes the decay of the excited compound nucleus, and (3) that only minor and systematic modifications are necessary to extend to the saddle point configuration the level density formalism valid for stable ground state deformation. In this framework the calculations were performed with the goal of departing as little as possible from established nuclear systematics readily available in the literature. The initial calculations utilized the optical model parameters of Becchetti and Greenlees,[5] the fission thresholds of Viola and Wilkins,[19] and the level density formulation and parameters of Gilbert and Cameron.[11] The fission barrier is treated throughout the

calculations as a single peaked barrier. Complete listings of the parameters used for all calculations reported herein are presented in Appendix E.

The first calculations of fission probabilities used unadjusted parameters available in the literature and are shown in Figure 13. The solid lines representing the predicted contributions from first, second, and third chance fisssion are respectively labeled 1, 2, and 3, and the total fission probability is represented by the darker heavy line. The data are shown as dots with error bars. The results of the code when applied to previously reported[20,21] neutron data on ^{237}Np are also shown.

Reproduction of the major features exibited by the data is not very good with the most striking discrepancy being the failure to reproduce the plateaus evident in the data after the opening of the second and third chance fission channels. The behavior shown by the calculated fission probabilities indicates that the energy dependence of the neutron emission to fission decay widths is strongly overestimated. This difficulty has been previously reported by others[13,14] and possibly reflects the fact that the ground state level density formalism does not properly describe that of the saddle point configuration. Deformation dependent level density calculations such as that of Decowski et al,[22] have been utilized by some authors[23] in treating the fission problem. However, it has been shown[13,14] that for a given nucleus one may approximate these results by simply varying the saddle point level density parameter a by the relation $a_f/a_n = \alpha(A)$.

The calculated effect of varying this ratio upon the neutron emission to fission widths is shown in Figure 14. It is evident that small changes in this parameter ratio can

Figure 13. Initial fission probabilities predicted by the model. The data are shown as dots with error bars. First, second and third chance fission probability curves are labeled respectively 1, 2, and 3. Reproduction of major features is very poor. In this calculation $\sigma_c = \sigma_R$. For $^{237}Np + n$ the neutron optical model parameters of Becchetti and Greenlees[5] were used. Parameters for these calculations are given in Appendix E, Table E1.

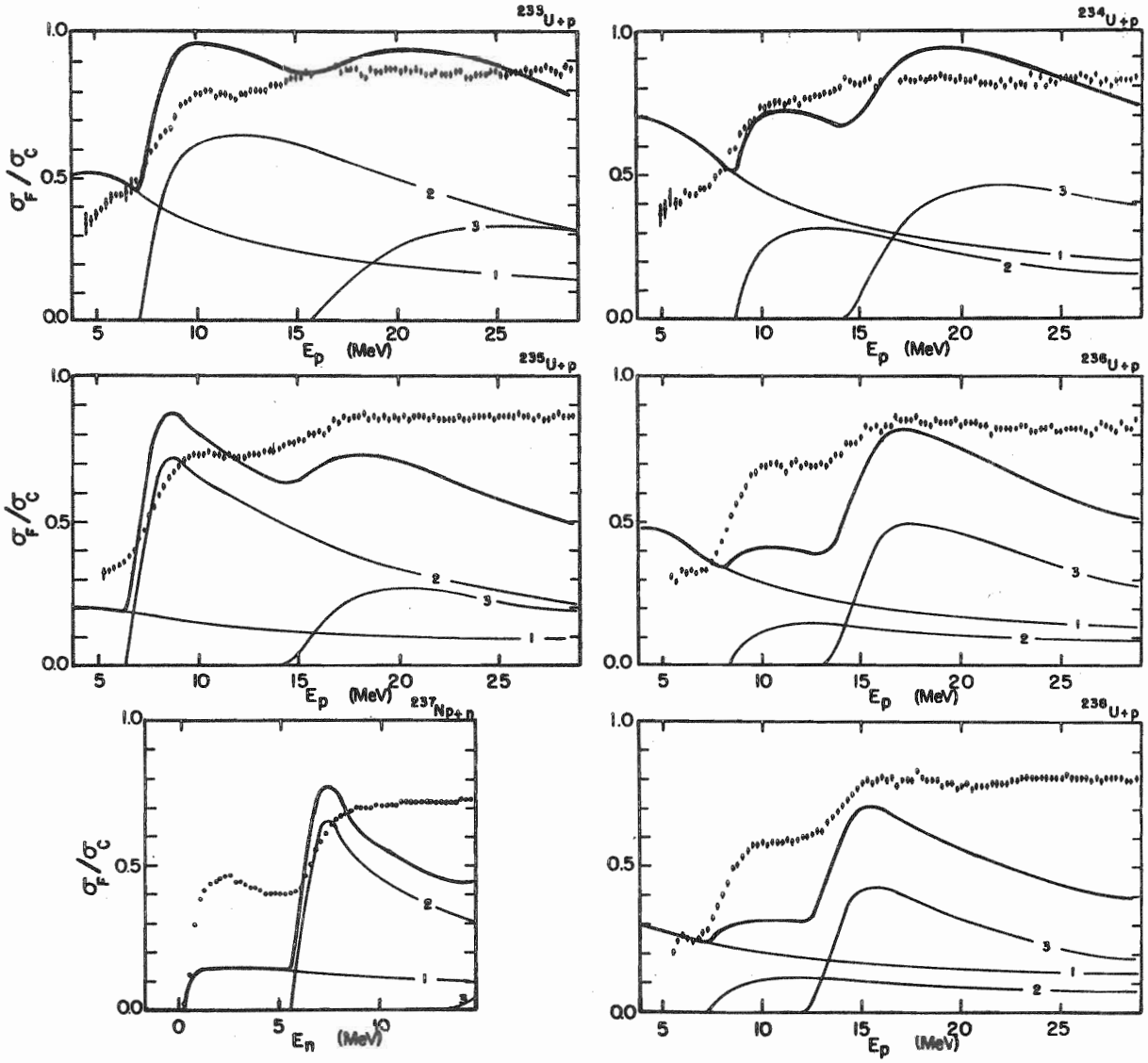
$^{233}U+p$
$^{234}U+p$
$^{235}U+p$
$^{236}U+p$
$^{237}Np+n$
$^{238}U+p$
σ_f/σ_c
E_p (MeV)
E_n (MeV)
1
2
3

Figure 14. An example of calculated Γ_n/Γ_f sensitivity to small variations in the level density parameter ratio as functions of nuclear excitation energy.

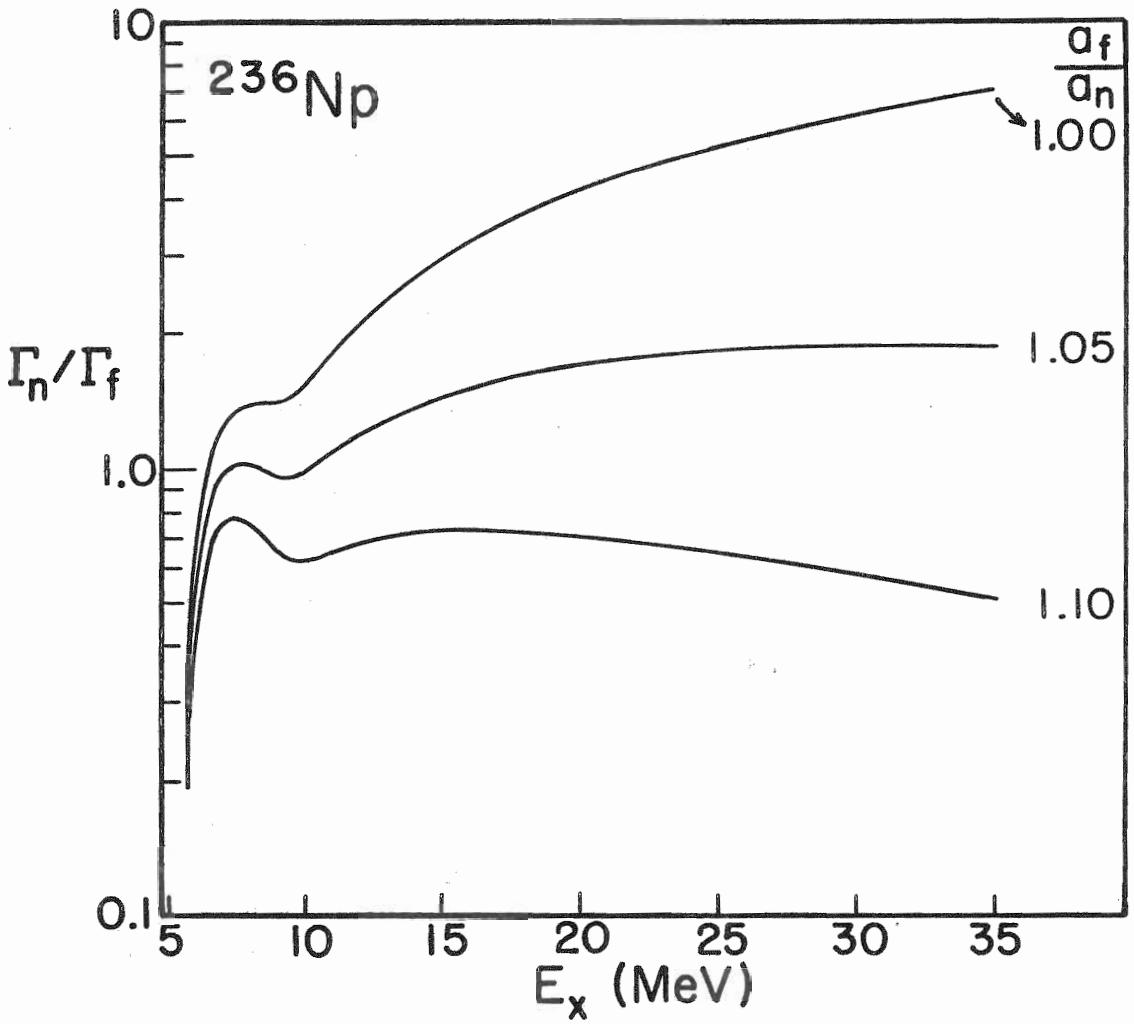
10
1.0
0.1
^{236}Np
$\frac{a_f}{a_n}$
1.00
1.05
1.10
Γ_n/Γ_f
5
10
15
20
25
30
35
E_x (MeV)

dramatically alter the energy dependence of the branching ratios.

The calculations shown in Figure 13 also indicate that many of the theoretical fission thresholds given by Viola and Wilkins are inconsistent with the data. For all subsequent calculations these thresholds were fixed by requiring that the calculated increase in fission yields associated with second and third chance fission occur at the energies at which the onset of these processes is revealed by the data.

The result of changing the effective fission threshold and setting $a_f/a_n = 1.075$ are shown in Figure 15. The calculated onset of each additional fission chance now occurs at the correct energy and the energy dependence now reflects the plateau-like behavior shown by the data. However gross discrepancies still exist in the magnitudes of the plateau heights.

The experimental plateau heights shown in Figures 13 and 15 which indicate small first chance fission probabilities and relatively larger second chance probabilities are not consistent with the systematics of previous analyses.[4] In addition, the experimental data as shown would indicate that the fission decay width of a given nucleus depends upon the method of forming that nucleus, i. e., whether it is a first chance or second chance fission event. These apparent inconsistencies can be greatly reduced by applying a correction to the optical model reaction cross section used to calculate the compound nucleus formation cross section as was discussed in Chapter III. The result of applying this correction is shown in Figure 16. Here the compound nucleus formation cross section used to reduce the data has been obtained from the following assumed relation:

$$\sigma_c(E_p) = f_c(E_p)\,\sigma_R(E_p) = 1.0 - \frac{2.0}{E_p} - \frac{3.0}{E_p^2}$$

Figure 15. Fission probabilities using $a_f/a_n = 1.075$, and a more reasonable set of fission thresholds. The shapes of the total probability curves are much improved over the results in Figure 13. For this calculation $\sigma_c = \sigma_R$. Parameters for these calculations are given in Appendix E, Table E2.

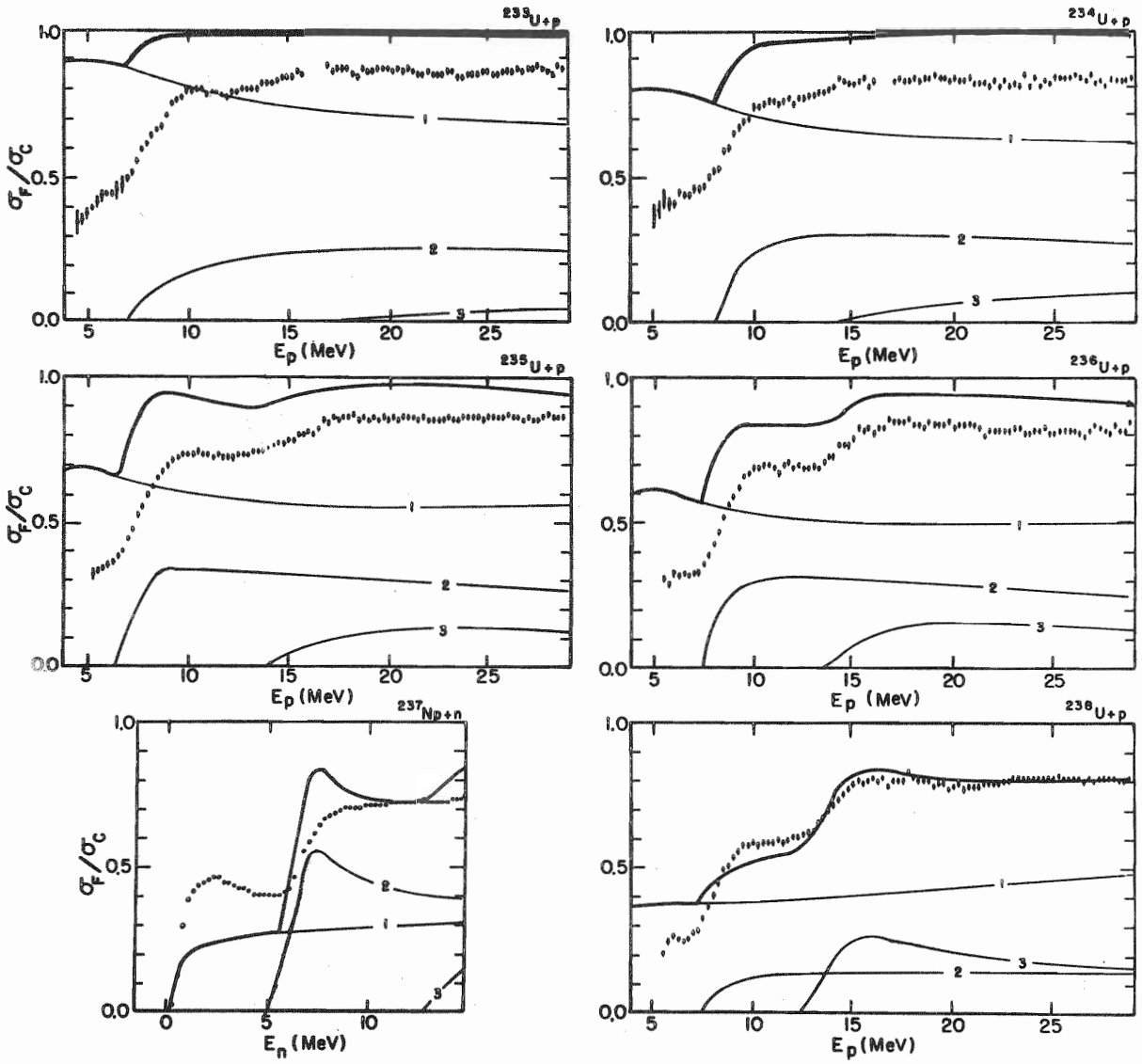
233U+p
234U+p
235U+p
236U+p
237Np+n
238U+p
σF/σC
Ep (MeV)
En (MeV)
1
2
3

Figure 16. Fission probabilities calculated by applying a correction to the optical model reaction cross section. The decay parameters are the same as those used for Figure 15. Parameters for these calculations are given in Appendix E, Table E3.

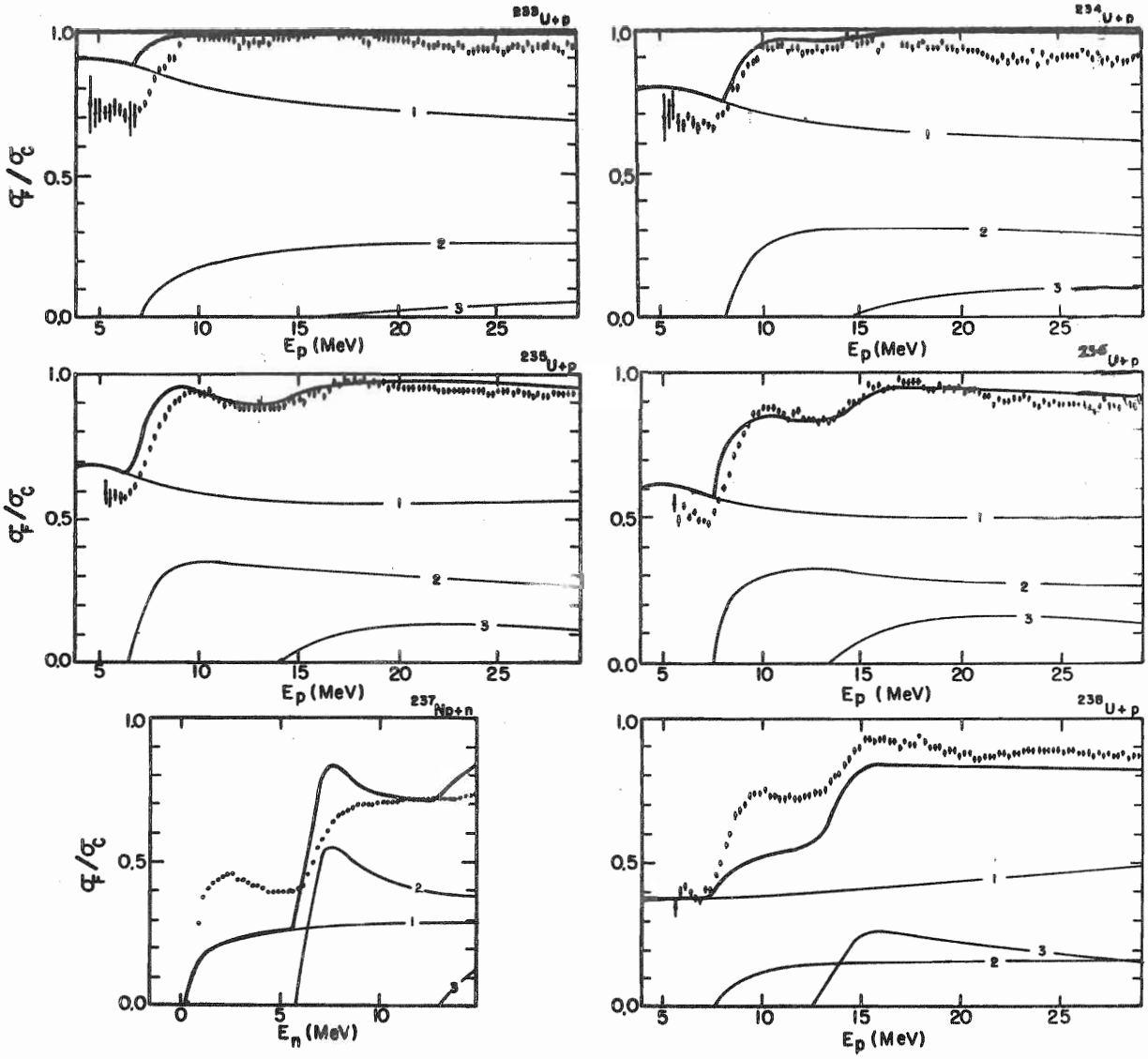
233U+p
234U+p
235U+p
236U+p
237Np+n
238U+p
σf/σc
Ep (MeV)
En (MeV)
1
2
3

where the coefficients have been determined in a manner described in Chapter III. Extensive searches on the coefficients have not been performed; however, the marked improvement of the "fit" to the data shown in Figure 16 is strong evidence for the validity of this approach. In the absence of reliable data for this energy region, it is felt that self consistent reaction cross sections derived in this manner are more reliable that those obtained by extrapolating the optical model parameters based on data taken at much higher energies.

At this point in the analysis considerable doubt exists as to the intrinsic significance of further parameter variations undertaken to improve the quality of the fit. The present version of the code PHROG is limited in that it considers only a single peaked fission barrier and it does not yet allow independent variation of the ground state and saddle point level density schemes except through the parameter ratio a_f/a_n. The fission thresholds and branching ratios resulting from the calculations shown in Figure 16 probably are as well determined as possible with the present computer codes. These fission thresholds are given in Appendix E and the Γ_n/Γ_f ratios are shown in Figure 17.

The branching ratio curves generally show the expected dependence on fissionability and the difficulty encountered in obtaining agreement for the ^{238}Np fission probability is reflected by the unusually large Γ_n/Γ_f ratio for this isotope. The anomalous behavior or bump in each curve for excitation energies between 5 and 10 MeV is a result of the hybrid nature of the Gilbert and Cameron level density formalism.[11] Γ_f is basically controlled by $\rho(A+1)$ while Γ_n is influenced by $\rho(A)$. For these two nuclei the matching energy, E_x, at

Figure 17. Calculated neutron emission to fission branching ratios for eight neptunium isotopes as functions of nuclear excitation energy. The parameters used for these calculations are the same as those used for Figures 15 and 16.

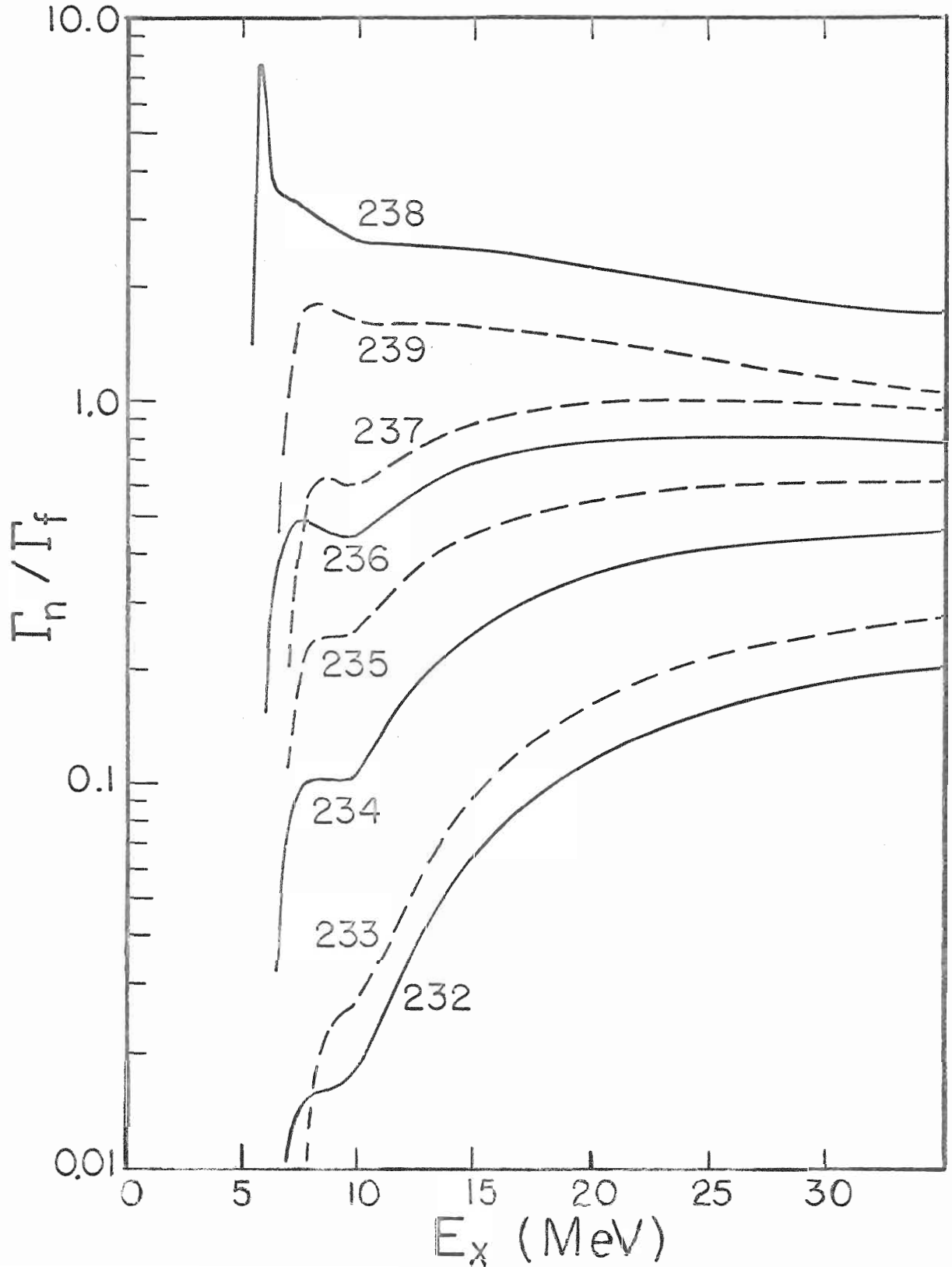
10.0
1.0
0.1
0.01
Γ_n / Γ_f
238
239
237
236
235
234
233
232
0
5
10
15
20
25
30
E_x (MeV)

which the level density prescription changes from the constant temperature model to a Fermi gas model, is different. Since the energy dependence of the two models is quite different, a ratio of the decay widths will show an inflection point for any energy region where the two different models are used.

One possibility for further parameter variation was suggested by the work of Moretto et al.[24] These authors found it necessary to include strongly increased pairing energies at saddle point configurations to explain fission angular distribution data. The present computer code does not allow independent variation of the saddle point pairing energies; therefore, let us consider qualitatively the effect of changing the pairing energy in the present calculation. The decay of the $^{A+1}$Np nucleus is primarily governed by the level densities at the saddle point deformation of $^{A+1}$Np and that of the stable ground state deformation of the residual nucleus ^{A}Np after neutron emission.

If $^{A+1}$Np has an even number of neutrons then an increase in pairing energy will reduce the available levels at the saddle point. At the same time the levels available for neutron emission remain the same since the pairing energy for ^{A}Np is zero in this case. Hence the fission probability will be reduced slightly causing a lower plateau for the total fission probability of $^{A+1}$Np.

If $^{A+1}$Np has an odd number of neutrons then the situation is reversed. There are fewer levels in ^{A}Np since N(A) is even and P(N) is increased. The pairing energy for the fissioning nucleus $^{A+1}$Np is zero and thus the levels for fission remain as before. Therefore an increase in the pairing energy for the $^{A+1}$Np nucleus increases the total fission probability.

If an overall increase of P(N) were applied to the parameters the effect on the fission probability curves would be an alternating increase and decrease in the plateaus for the theoretical curve. Utilizing this effect the level density pairing energies were varied for the individual nuclei and the results are shown in Figure 18. Although there remains some problem with the two extreme nuclei, $^{233}U + p$ and $^{238}U + p$, the overall fit has indeed been improved by this change in parameters.

It is reasonable to expect small variations in the actual shape of the fission barrier as a function of A. This effect can perhaps be approximately included by allowing small changes in a_f/a_n for the different mass isotopes. The results are shown in Figure 19. Improvements are readily seen in the first chance plateaus, and in fact, there is an overall improvement for all isotopes and all energies.

Within the limitations of the present calculations, the results shown in Figures 14 through 18 may indicate either a stronger A dependence on the absorption potential of the optical model, which would be reflected in an A dependence in the correction function $f_c(E_p)$; a different A dependence in the level density parameter ratio a_f/a_n ; or a different dependence of the pairing energies on A. Systematic study of these effects will be undertaken following refinement of the present calculation.

Figure 18. Fission probabilities obtained by changing the pairing energy as discussed in the text. Parameters used for these calculations are listed in Appendix E, Table E4.

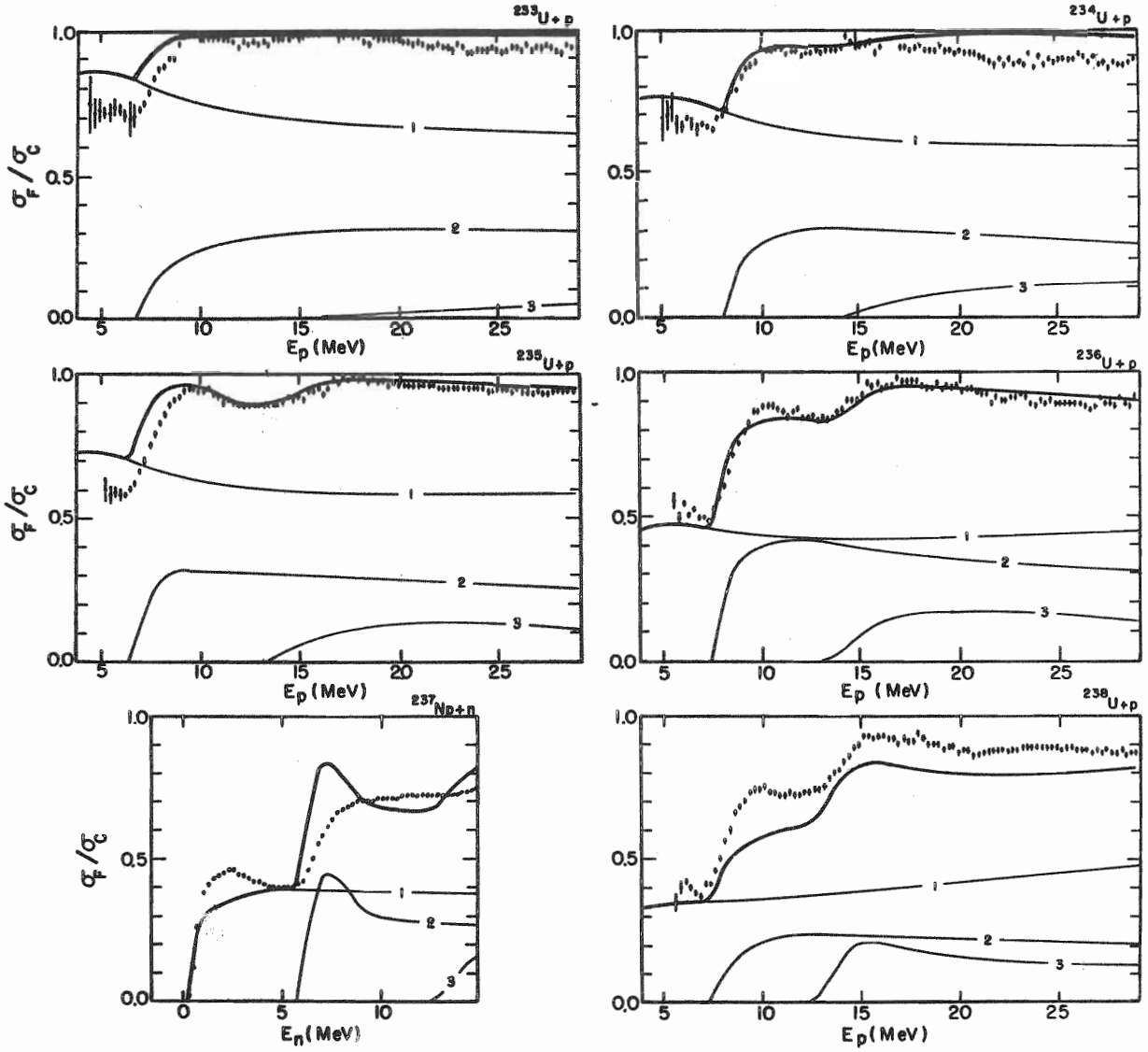
233U+p
234U+p
235U+p
236U+p
237Np+n
238U+p
σF/σC
Ep (MeV)
En (MeV)
1
2
3

Figure 19. Fission probabilities obtained by changing the level density parameter ratio $a_f/a_n=\alpha(A)$. Parameters used for these calculations are given in Appendix E, Table E5.

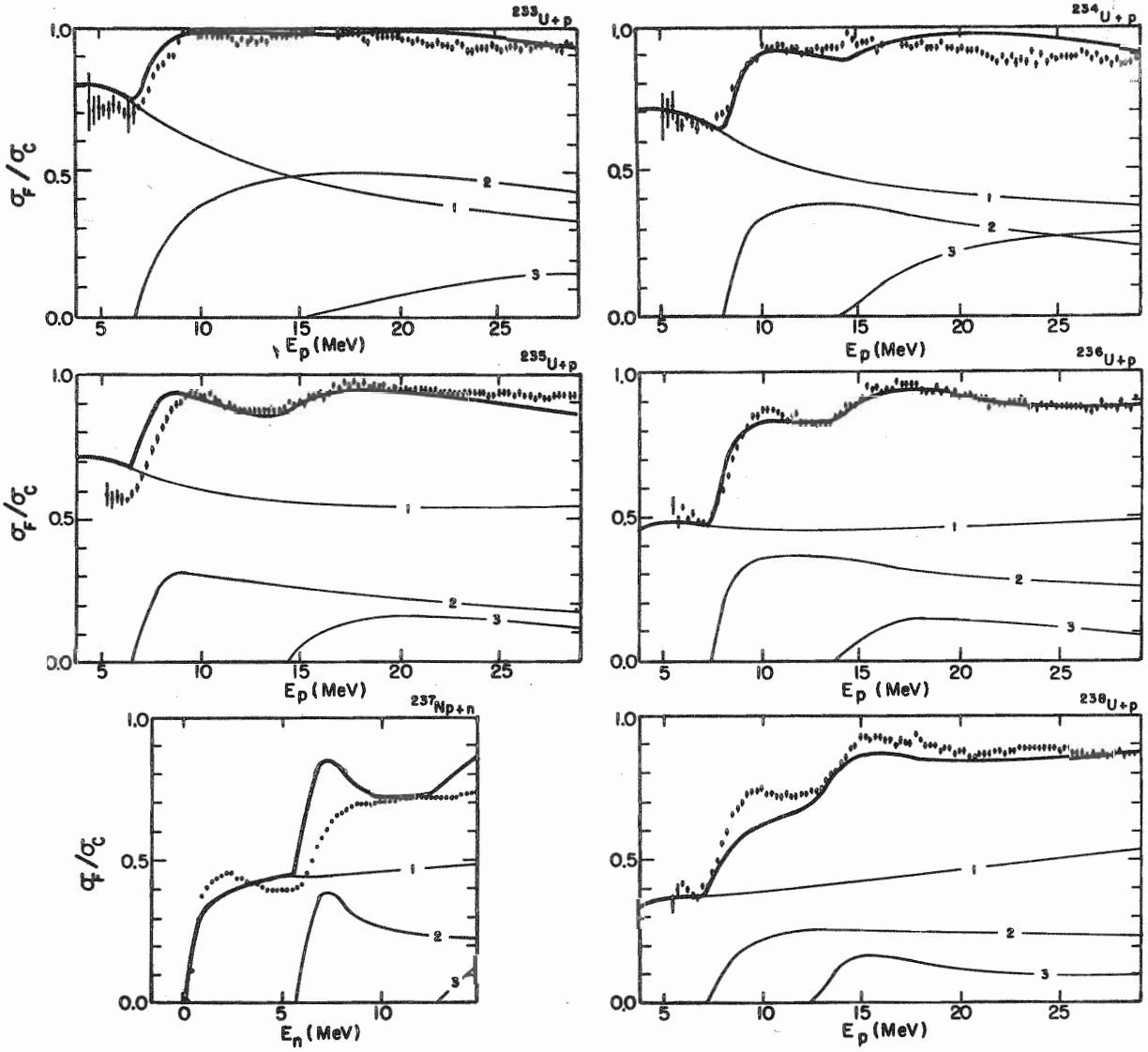
233U+p
234U+p
235U+p
236U+p
237Np+n
238U+p
σf/σc
Ep (MeV)
En (MeV)
1
2
3

Chapter V
CONCLUSIONS

Total proton induced fission cross sections of the stable uranium isotopes have been accurately measured for a wide range of excitation energies. A method of analysis has been formulated and demonstrated which makes use of the extended energy range of the data and selection of an isotopic sequence of target nuclei to unfold the contributions to the measured cross section from first, second, and third chance fission. Using this method, previously undetermined fission thresholds are estimated and Γ_n/Γ_f ratios have been deduced for individual fissioning nuclei as functions of excitation energy. Results of preliminary analyses indicate that while these branching ratios are not strongly energy dependent for energies above thresholds, the precise energy dependence at higher excitation energies is probably dependent upon the mass number of the fissioning nucleus. A more detailed study of the systematics is underway.

In addition, it has been shown that the conventional optical model parameters overestimate proton reaction cross sections for incident proton energies below the Coulomb barrier. Further investigation of the energy dependence of charged particle optical model parameters is in order.

Our method of analysis is general enough to allow inclusion of many refinements based on the current state of fission theory. Planned improvements will incorporate a double humped fission barrier, a deformation dependent level density formalism, and the effect of fourth chance fission. It is hoped that these improvements will make unnecessary the somewhat artificial variation of pairing energies and level density

parameters required in this initial analysis to reproduce the data more closely.

The ability to unfold the contributions of individual fissioning nuclei to the total experimental fission cross sections will lead naturally to more precise information concerning the dynamics of the fission process. Applied to angular distribution data, fragment mass yields, neutron multiplicity, and kinetic energy studies, the analysis method will serve to remove much of the ambiguity which presently obscures most fission data taken at medium excitation energies. Results of these studies can yield information about the fission process which can be reapplied to the cross section analysis. Thus in a bootstrap type of calculation one can hope to achieve convergence to an unambiguous understanding of the multiple fission processes.

APPENDIX

Appendix A
Target Thickness Measurements

A measurement of the number of nuclei exposed to the beam is necessary for obtaining absolute cross sections. In this appendix we will detail the method used to determine this quantity for each target.

Initially each target was investigated by measuring 5 MeV elastically scattered protons at several angles with a surface barrier particle detector. The energy of these protons is about 10 MeV below the Coulomb barrier for uranium. The target backings were either nickel or carbon. The isotopic purity of the targets was measured at ORNL and was better than 99% as given in table I. Thus the highest energy peak in the pulse height spectrum should be due only to the protons elastically scattered from the uranium isotope. This peak is well separated from that due to protons scattered by the target backing material.

However, using the results of these initial efforts the value of the measured fission cross section for the first ^{233}U target was barely half the result obtained for any other isotope and was inconsistent with previously reported work.[25] After checking solid angles, detectors, beam integration, and electronics, it was decided to investigate the target with a 10 MeV alpha beam. For alphas the uranium Coulomb barrier is about 24 MeV. Kinematically it would be possible to separate from the uranium peak one due to any stable contaminant.

The result of the measurement on this target confirmed the suspicion that a high Z contaminant was present, either tungsten

or tantalum. Both of these metals are commonly used as evaporation boats in the preparation of targets.

Subsequently all other targets were investigated by the following experimental procedure. Rutherford scattering angular distributions were measured first using 10 MeV alpha particles and then using 5 MeV protons. The requirement that the contaminant peak be kinematically separated restricted the measurements to angles $\geq 100^{\circ}$ while chamber geometry limited the extreme scattering angle to 150°. Pulse height spectra were accumulated at 100°, 110°, 120°, 130°, 140°, and 150° for both projectiles. Both alpha and proton spectra were stored on magnetic tape for later analysis.

The analysis consisted of determining the number of scattering events for a peak in a pulse height spectrum. This was accomplished by a sum of the counts in the peak minus a linear background of counts. The value thus obtained was checked by fitting the peak to a Gaussian shape, then subtracting a linear background from the area of the Gaussian. The two methods yielded essentially identical results.

Once the number of events has been determined the target thickness is found by

$$\tau_A = \frac{K \times A_{wt} \times N_e}{B \times P \times \Delta\Omega \times R^A} \qquad (A1)$$

where K = unit correction constant
A_{wt} = atomic weight of the target
N_e^A = number of counts in the peak
B = full scale beam current integrator setting
P = preset live charge setting
$\Delta\Omega$ = solid angle subtended by the detector in sr.
R^A = Rutherford scattering cross section in mb/sr.

$$R^A = 1.296 \left(\frac{z_1 z_2}{E}\right)^2 \csc^4(\Psi/2) . \qquad (A2)$$

The unit correction constant, K, contains N_0 (Avogadro's number) as well as other constants required to express τ in $\mu g/cm^2$. The product $B \times P$ represents the total integrated charge.

If a contaminant cannot be resolved and is in the proton peak then

$$N_p^{U+\alpha} = N_p^U + N_p^\alpha = \left(\frac{B_p P_p \Delta\Omega_p R_p^U}{K}\right)\frac{\tau_U}{A_U} + \left(\frac{B_p P_p \Delta\Omega_p R_p^\alpha}{K}\right)\frac{\tau_\alpha}{A_\alpha} . \qquad (A3)$$

Solving for τ_U

$$\tau_U = \left\{ N_p^{U+\alpha} - \left(\frac{B_p P_p \Delta\Omega_p R_p^\alpha}{K}\right)\frac{\tau_\alpha}{A_\alpha} \right\} \frac{K A_U}{B_p P_p \Delta\Omega_p R_p^U} . \qquad (A4)$$

The ratio τ_α/A_α can be determined from the 10 MeV Coulomb scattered alpha spectra:

$$\frac{\tau_\alpha}{A_\alpha} = \frac{K N_\alpha^\alpha}{B_\alpha P_\alpha \Delta\Omega_\alpha R_\alpha^\alpha} . \qquad (A5)$$

For the target thickness measurements the same detector, solid angle, and BCI setting were used for both protons and alphas. Noting that $E_\alpha = 2E_p$, substituting (A5) into (A4), and using (A2) for the ratio of $R_p^\alpha/R_\alpha^\alpha$ we have the equation finally used:

$$\tau_U = \left\{ N_p^{U+\alpha} - \frac{P_p}{P_\alpha} N_\alpha^\alpha \right\} \frac{K A_U}{B_p P_p \Delta\Omega_p R_p^U} . \qquad (A6)$$

Note that is is not necessary to determine what the contaminant actually is. All that is required is to be able to resolve it with the alpha beam.

The results of this method are shown in Figure A1. The amount of contaminant in each target except ^{238}U was enough to

Figure A1. Target thickness measurements. Numerical results for the three methods shown are given in Chapter II, Table I.

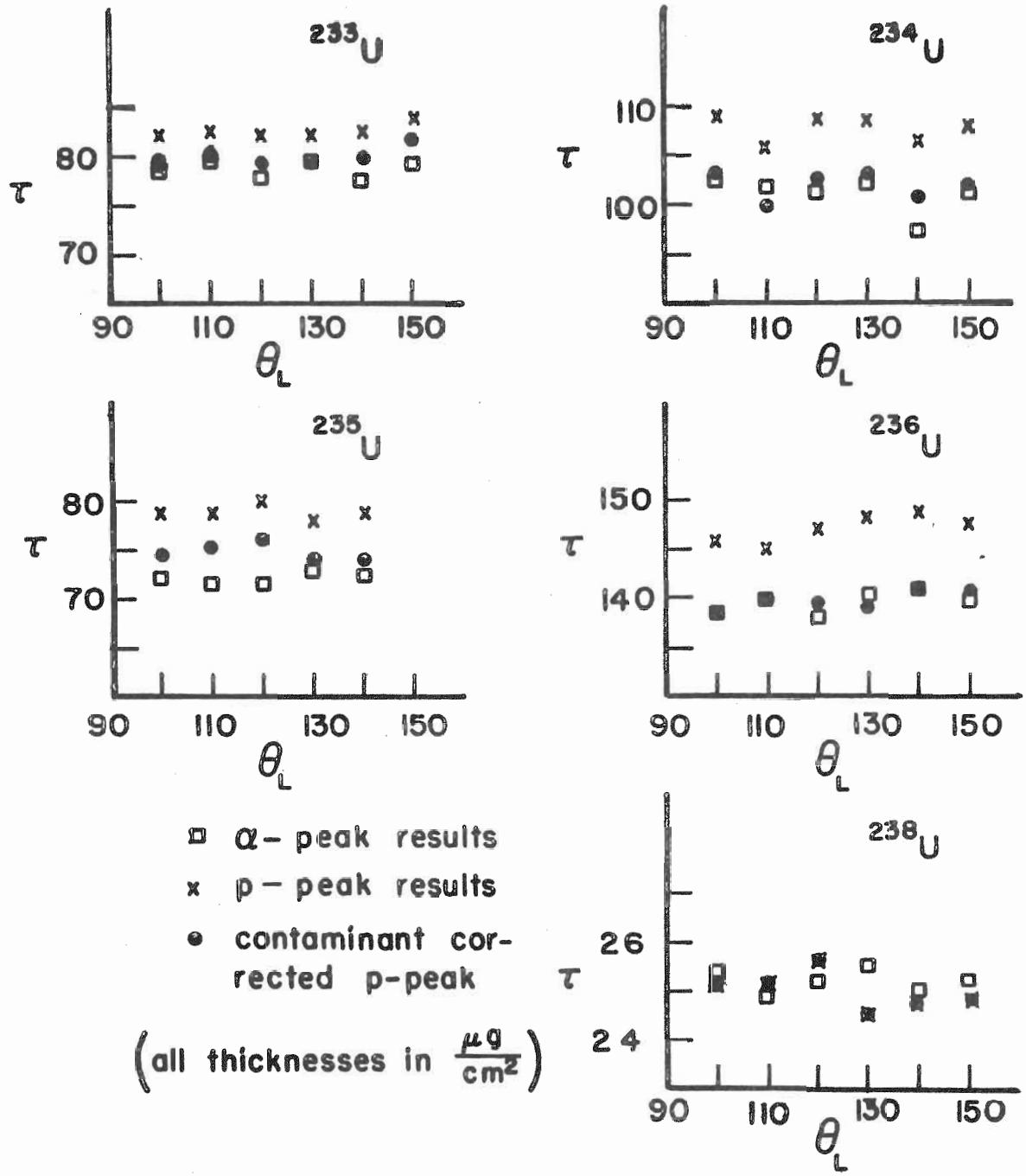

TARGET THICKNESS MEASUREMENTS

introduce a significant systematic error in the determination of total cross section. The contaminant corrected proton results are seen to be in good agreement with the thicknesses obtained with alphas. A root mean square average of the corrected proton results was used to determine the target thicknesses actually used to calculate the final cross section values.

Appendix B
Discussion of Optical Model Parameters

In this appendix we will discuss the various optical model parameter sets used in the data analysis. The results of five elastic scattering proton angular distribution measurements are also presented.

The optical model describes the nuclear potential as the sum of the Coulomb potential, a real potential, a volume imaginary potential, a surface imaginary potential, and a spin orbit potential. Each potential except the Coulomb is described by a well depth, radius, and diffuseness.

The explicit formulation of the potential is shown in the upper left hand quadrant of Figure B1. The other three quadrants of the figure contain three of the current optical model parameter formula sets found in the literature.

The Perey set reported in 1963 represents the analysis of 35 elastic scattering angular distributions for incident proton energies 9 to 22 MeV.[8] More recently, in 1968, Becchetti and Geeenlees reported the result of a global search over all parameters for proton elastic scattering data in the mass range $40 \leq A \leq 208$ and energy range $E_p \leq 50$ MeV.[5] The Menet et al., set was reported in 1971 and represents an analysis of total proton reaction cross section measurements for the energy range 30 to 60 MeV and for the mass range $12 \leq A \leq 208$.[7]

Figure B1. Optical model potential formulation and three sets of current parameter formulas reported in the literature.

OPTICAL MODEL POTENTIAL

$$V(r) = V_c(r) + V_R \frac{1}{1+e^{x}} - i W_{VOL} \frac{1}{1+e^{x'}}$$

$$- 4 i W_{SURF} \frac{d}{dx'} \frac{1}{1+e^{x'}} + U_{so}(r)$$

where

$$V_c(r) = \begin{cases} \frac{Z z e^2}{2R_c}\left[3 - \left(\frac{r}{R_c}\right)^2\right], & r \le R_c = r_c A^{1/3} \\ \frac{Z z e^2}{r}, & r \ge R_c \end{cases}$$

$$U_{so}(r) = 2 V_{so} \frac{1}{r} \frac{d}{dr}(1+e^{x''})^{-1} 2 \vec{L}\cdot\vec{s}$$

$$x = (r - r_R A^{1/3})/a_R$$

$$x' = (r - r_W A^{1/3})/a_W$$

$$x'' = (r - r_{so} A^{1/3})/a_{so}$$

Becchetti & Greenlees

$$V_R = \left\{58.0 - 0.36 E_p + 0.4\left(\frac{Z}{A^{1/3}}\right) + 25.0\left(\frac{N-Z}{A}\right)\right\} \text{ MeV}$$

$$W_{VOL} = \{0.27 E_p - 2.5\} \text{ MeV}$$

$$W_{SURF} = \left\{10.3 - 0.2 E_p + 12.0\left(\frac{N-Z}{A}\right)\right\} \text{ MeV}$$

$V_S = 6.2$ MeV

$r_R = 1.17$ f $a_R = 0.78$ f

$r_W = 1.34$ f $a_W = \left\{0.45 + 0.7\left(\frac{N-Z}{A}\right)\right\}$ f

$r_{so} = 0.97$ f $a_{so} = 0.75$ f

$r_c = 1.2$ f

Menet, et. al.

$$V_R = \left\{49.9 - 0.22 E_p + 0.4\left(\frac{Z}{A^{1/3}}\right) + 26.4\left(\frac{N-Z}{A}\right)\right\} \text{ MeV}$$

$$W_{VOL} = \{1.2 - 0.09 E_p\} \text{ MeV}$$

$$W_{SURF} = \left\{4.2 - 0.05 E_p + 15.5\left(\frac{N-Z}{A}\right)\right\} \text{ MeV}$$

$V_{so} = 6.04$ MeV

$r_R = 1.16$ f $a_R = 0.75$ f

$r_W = 1.37$ f $a_W = \left\{0.74 - 0.008 E_p + 1.0\left(\frac{N-Z}{A}\right)\right\}$ f

$r_{so} = 1.064$ f $a_{so} = 0.78$ f

$r_c = 1.2$ f

Perey

$$V_R = \left\{53.3 - 0.55 E_p + 0.4\left(\frac{Z}{A^{1/3}}\right) + 27.0\left(\frac{N-Z}{A}\right)\right\} \text{ MeV}$$

$$W_{VOL} = \{0.4 E_p - 3.8\} \text{ MeV}$$

$$W_{SURF} = \left\{14.3 - 0.3 E_p + 48.0\left(\frac{N-Z}{A}\right)\right\} \text{ MeV}$$

$V_{so} = 6.2$ MeV

$r_R = 1.25$ f $a_R = 0.65$ f

$r_W = 1.25$ f $a_W = 0.47$ f

$r_{so} = 1.01$ f $a_{so} = 0.75$ f

$r_c = 1.2$ f

We measured five angular distributions of elastically scattered protons on two of the targets and compared them with optical model calculations using the three sets in Figure B1. The results are shown in Figure B2. By closely inspecting these graphs one can see that only the Menet set gives a reasonable fit to both back and foward angle data. The other two sets underestimate the back angle cross section and overestimate the foward angle cross section.

If one uses these three parameter sets to calculate the total reaction cross section, σ_R , and assumes the compound nucleus formation cross section, σ_c , is equal to σ_R , then one typically obtains fission probabilities shown in Figure B3. The first chance fission probability for either B3(a) or B3(d) is too small, indicating that these two sets tend to overestimate the reaction cross section, whereas the result of Perey's set, B3(c), in this region is reasonable. However, the behavior of B3(c) in the 7-12 MeV range is difficult to explain within our present statistical model without drastically altering the values of the known neutron binding energies or the fission thresholds, or both. The Perey set underestimates the reaction cross section for these energies, in agreement with the results of total neutron cross section measurements of highly deformed nuclei.[26]

We concluded that of the three sets, the Bechetti and Greenlees set represented a reasonable compromise between the results of the angular distribution analysis (See Figure B2) and the reduced cross section analysis. However a correction to the reaction cross section was still necessary in order to obtain a compound nucleus formation cross section which would result in consistent fission probabilities for neighboring isotopes. The result of the correction used is shown in Figure B3(b).

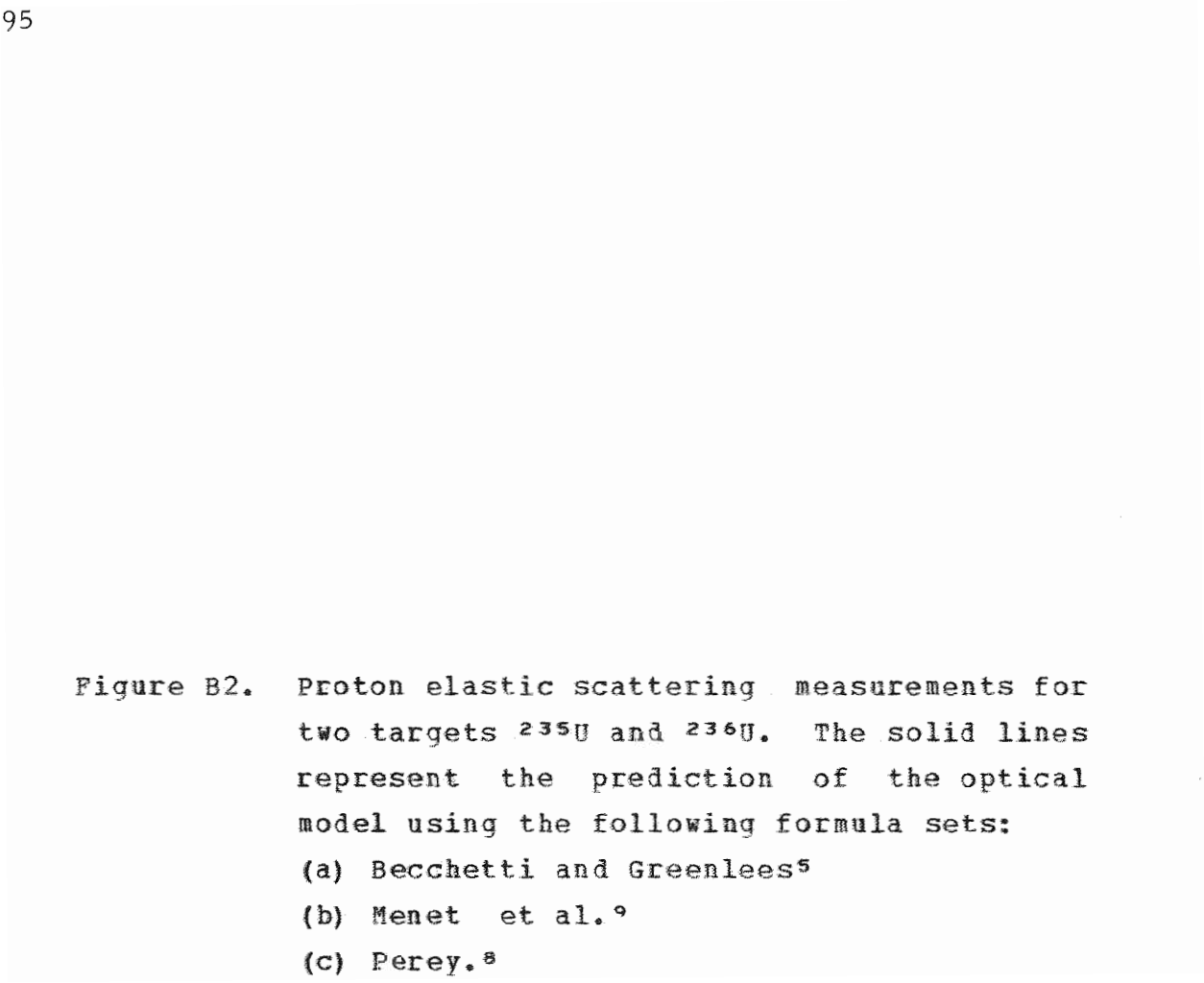

Figure B2. Proton elastic scattering measurements for two targets ^{235}U and ^{236}U. The solid lines represent the prediction of the optical model using the following formula sets:
(a) Becchetti and Greenlees[5]
(b) Menet et al.[9]
(c) Perey.[8]

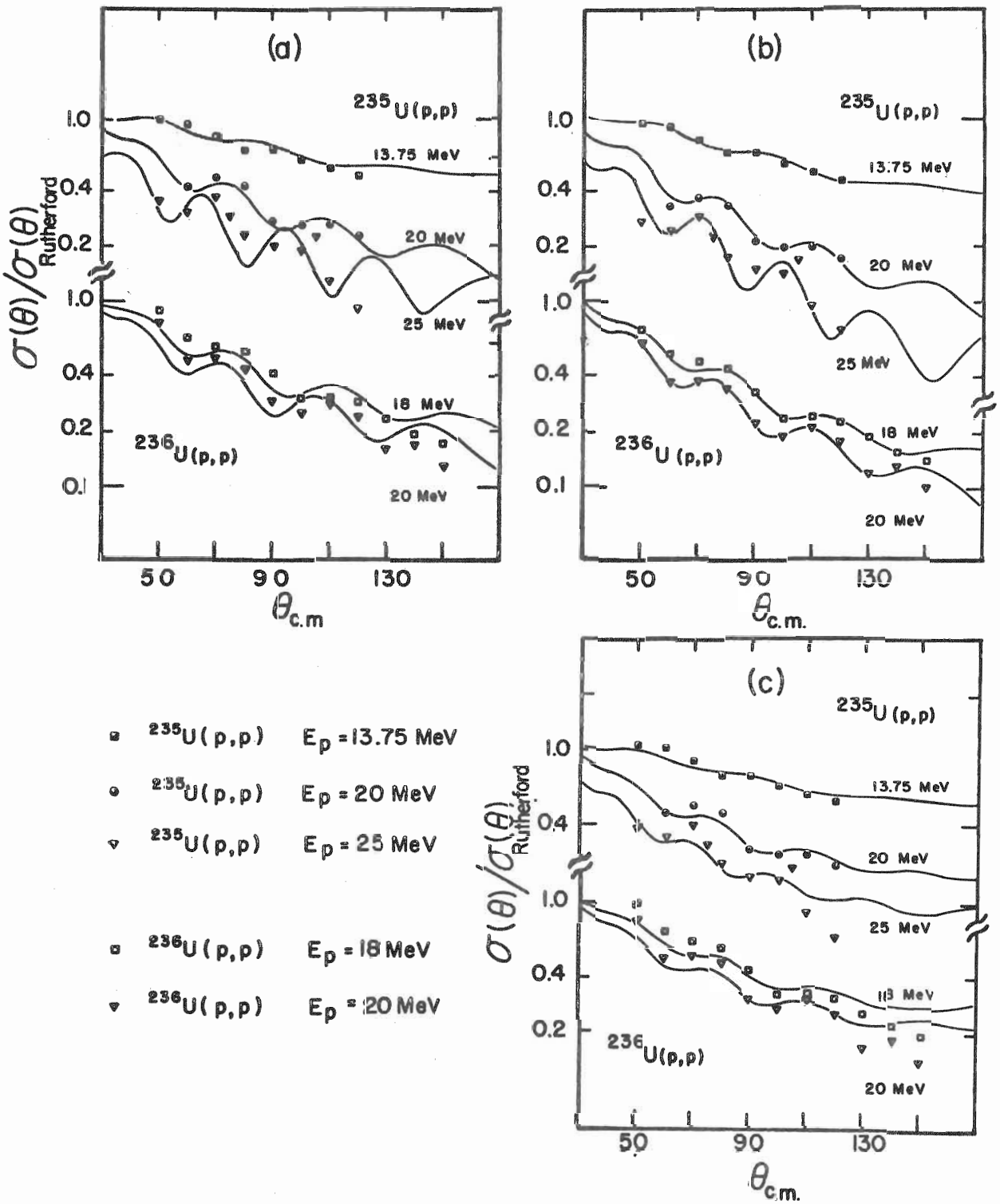
(a)
(b)
(c)
^{235}U(p,p)
13.75 MeV
20 MeV
25 MeV
^{236}U(p,p)
18 MeV
20 MeV
$\sigma(\theta)/\sigma(\theta)_{Rutherford}$
$\theta_{c.m.}$
50
90
130
1.0
0.4
0.2
0.1
^{235}U(p,p) E_p = 13.75 MeV
^{235}U(p,p) E_p = 20 MeV
^{235}U(p,p) E_p = 25 MeV
^{236}U(p,p) E_p = 18 MeV
^{236}U(p,p) E_p = 20 MeV

Figure B3. Total fission probabilities for ^{238}U + p using the following compound nucleus formation cross sections:

(a) $\sigma_c = \sigma_R$ (Becchetti and Greenlees[5])

(b) $\sigma_c = (1.0 - \frac{2.0}{E_p} - \frac{2.0}{E_p^2})\sigma_R$ (Bechetti and Greenlees[5])

(c) $\sigma_c = \sigma_R$ (Perey[8])

(d) $\sigma_c = \sigma_R$ (Menet et al.[9])

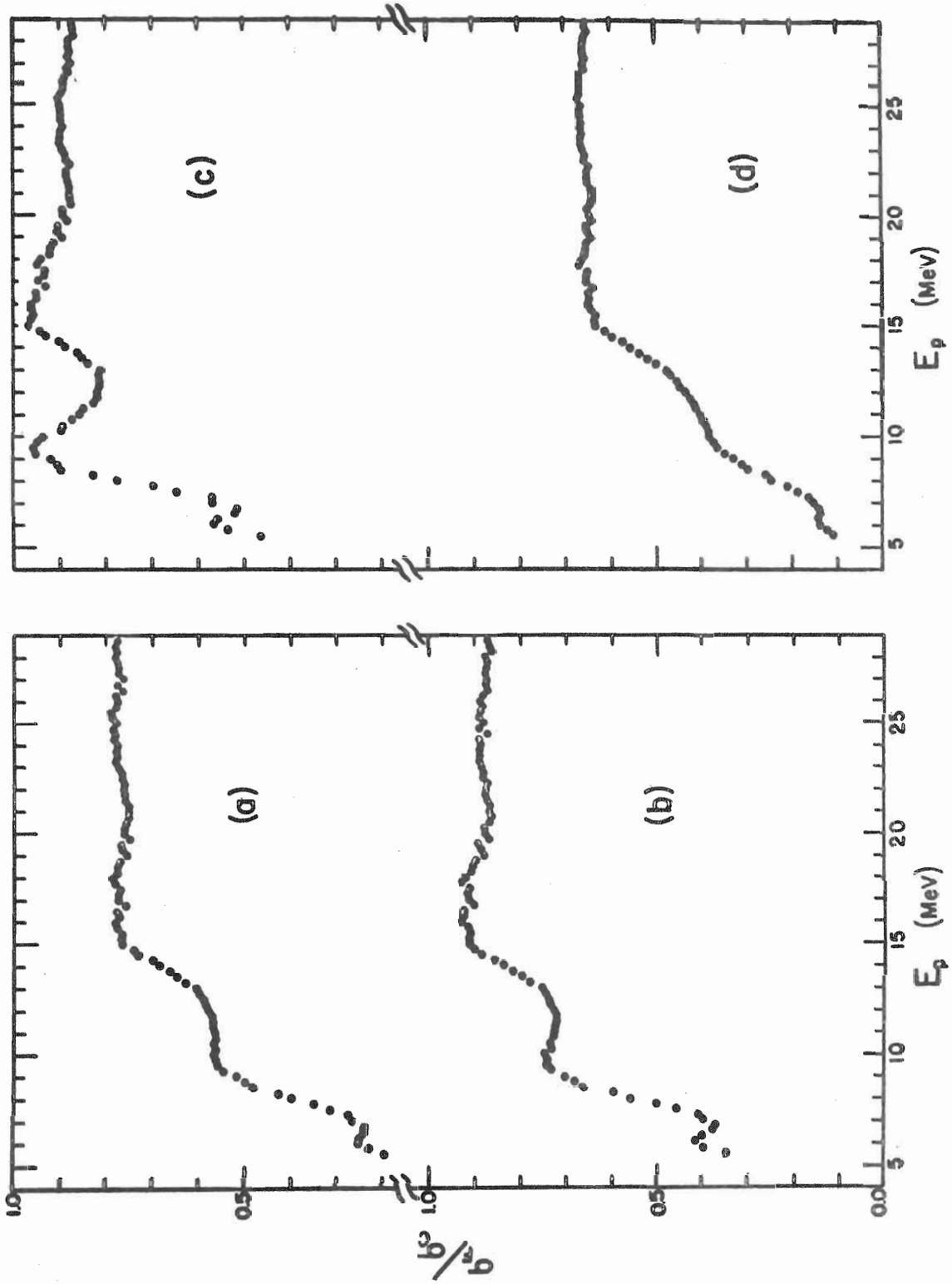
(a)
(b)
(c)
(d)
σ_s/σ_c
E_p (MeV)
E_p (MeV)

For the calculations of $\overline{K_o^2}$ discussed in the following appendix we used the same optical model computer code to calculate J(J+1), the average square of the angular momentum of the compound system. Figure B4 shows the result as a function of beam energy for a spin zero uranium target.

Figure B4. The average square of the angular momentum of the compound system as a fuction of beam energy.

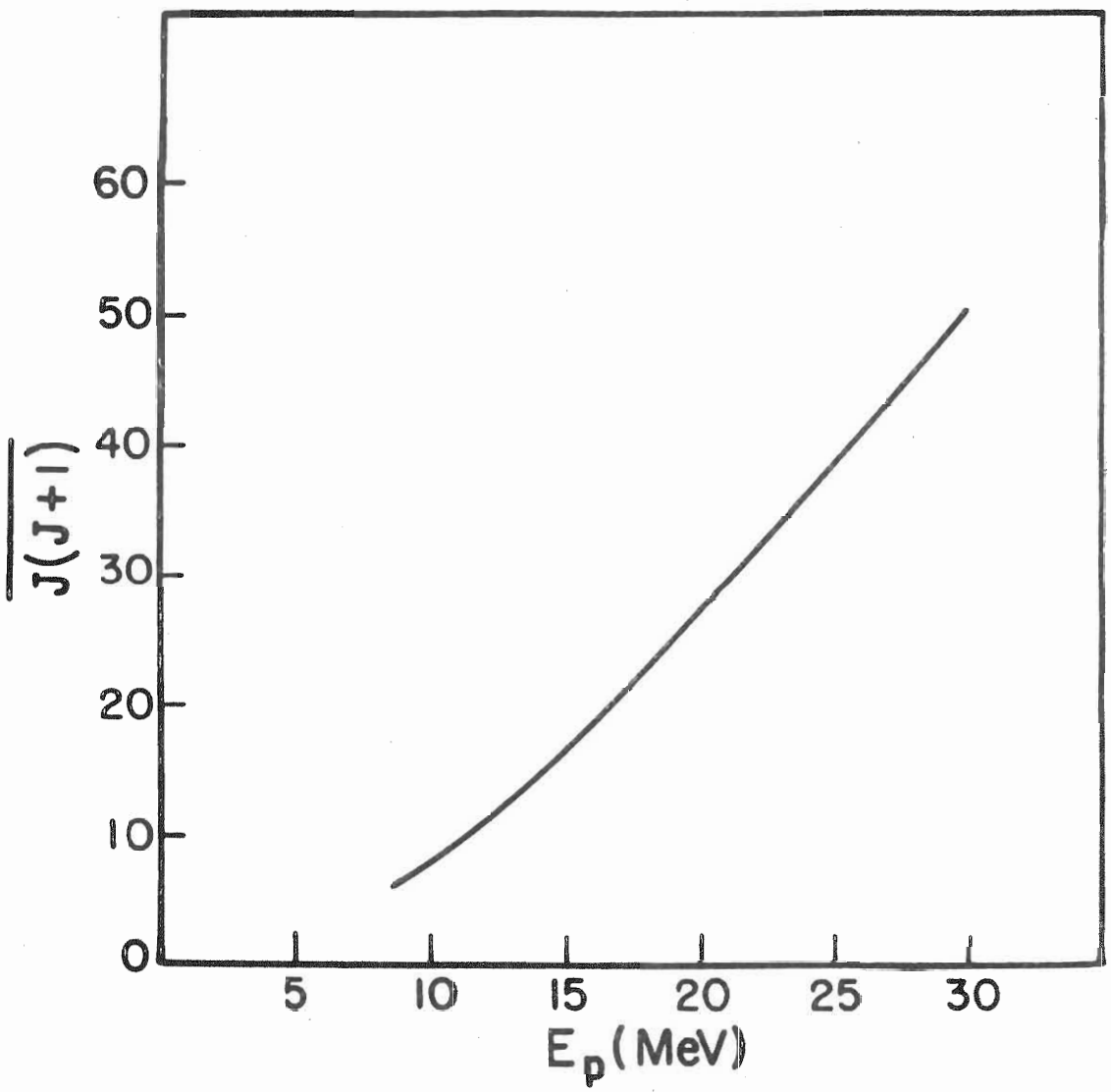
60
50
40
30
20
10
0
$\sqrt{J(J+1)}$
5
10
15
20
25
30
E_p (MeV)

Appendix C
Fission Fragment Angular Distribution Analysis

In this appendix we will discuss the reduction of the angular distribution measurements which were taken in a 24" diameter scattering chamber. The large chamber allowed the fission fragment detectors to be placed sufficiently far from the target so that the angular distributions could be measured over an angular range from 20° to 160° in the lab. In this chamber a freon refrigeration system was used to cool the detectors. Two fragment detectors were placed 180° apart, thus allowing the simultaneous collection of data in the forward and back hemispheres with overlapping data taken by both detectors at 80°, 90°, and 100°. The overlapped data was used to insure consistency between the forward and back angle detectors. More than 100 such angular distributions were taken for the five isotopes.

For the discussion of this appendix it is useful to transform the laboratory angular distributions into the center of mass. The transformation is

$$\sigma(\theta_{cM}) = \sigma(\psi_L)(1-\Delta\cos\psi_L)$$

where:

$$\Delta = \left\{ \frac{M_p M_T}{M_{f1} M_{f2}} \frac{E_p}{E_p + Q} \right\}^{1/2}$$

M_p = mass of proton
M_T = mass of target
M_{f1} = mass of fragment #1
M_{f2} = mass of fragment #2
E_p = proton lab energy
Q = fission energy release.

Detailed information about the fragment masses is not currently available over the entire energy range of the data, however, table C1 indicates that the change in the c.m. factor from symmetric fission to highly asymmetric fission is sufficiently small to have little effect on the resulting distribution.

TABLE C1

Sensitivity of the c.m. Factor to Fragment Mass

(E_0 = 25 MeV, Q = 175 MeV)

(M_{f1}, M_{f2})	Δ
(118, 118)	0.046
(78, 156)	0.049

Once transformed into the center of mass each angular distribution was fitted by an exact least squares with each of the following Legendre Polynomials:

$$f_1(\theta) = A_0 P_0 + A_2 P_2 \qquad (C1)$$

$$f_2(\theta) = A_0 P_0 + A_2 P_2 + A_4 P_4 \qquad (C2)$$

$$f_3(\theta) = A_0 P_0 + A_2 P_2 + A_4 P_4 + A_6 P_6 \qquad (C3)$$

The results of this procedure are shown in figure C1 where we have plotted the value of the highest power coefficient as a function of energy for each of the functions. The overall trend of the coefficients A_4 and A_6 is consistent with zero for all the isotopes and energies considered. The values of A_2, on the other hand, are nonzero and appear to have definite energy dependence. Thus we have shown that the angular distributions have at most a $\cos^2\theta$ dependence. The function $f_1(\theta)$ can be written as

$$W(\theta) = \alpha (1 + \epsilon \cos^2 \theta) \qquad (C4)$$

where

$$\alpha = (A_0 - 1/2\, A_2) \qquad (C5)$$

$$\epsilon = 3/2\, (A_2/\alpha) \qquad (C6)$$

Equation C4 is the usual form assumed for fission fragment angular distribution analyses.

Figure C1. Results of an exact least square fit of the Legendre polynomials $f_1(\theta)$, $f_2(\theta)$, $f_3(\theta)$. The value of the highest order coefficient for each polynomial is plotted as a function of beam energy.

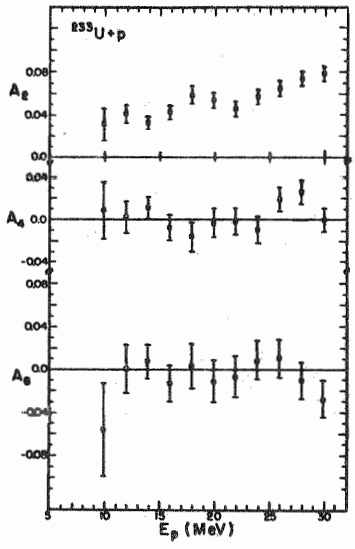
^{233}U+p
A_2
A_4
A_6
E_p (MeV)

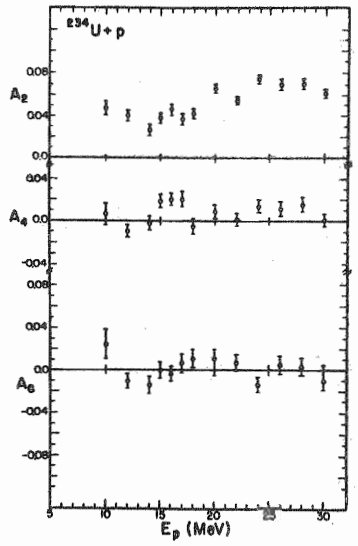
^{234}U+p
A_2
A_4
A_6
E_p (MeV)

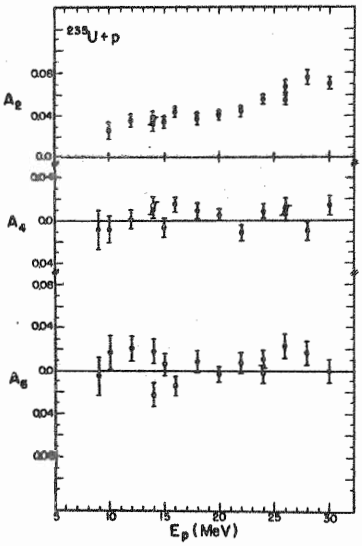
^{235}U+p
A_2
A_4
A_6
E_p (MeV)

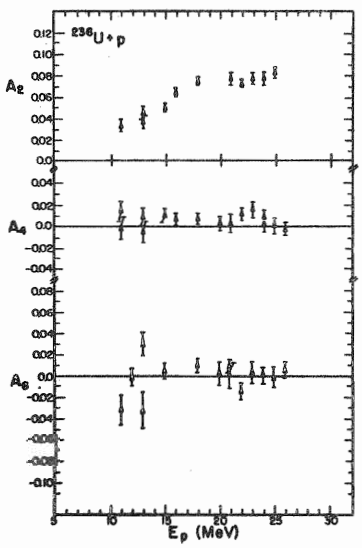
^{236}U+p
A_2
A_4
A_6
E_p (MeV)

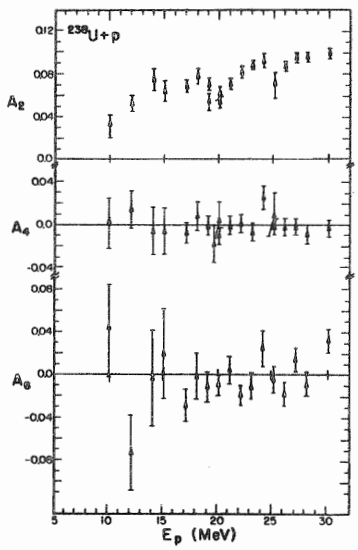
^{238}U+p
A_2
A_4
A_6
E_p (MeV)

The anisotropy in fission fragment angular distributions is generally believed to be due to a nonuniformity in the distribution of the projections K of the total angular momentum J along the direction of fission. Halpern and Srutinsky[27] have predicted a Gaussian distribution of K for a few MeV above the fission barrier of the form

$$P(K) \propto \exp\left\{-\frac{\hbar^2}{2T}\left(\frac{1}{\mathcal{I}_{\parallel}}-\frac{1}{\mathcal{I}_{\perp}}\right)K^2\right\} \qquad (C7)$$

where the $\mathcal{I}$'s are the moments of inertia of the deformed nucleus in its saddle point shape for rotation parallel to and perpendicular to the axis of symmetry. The resulting angular distribution is described by

$$W(\theta) = 1 + \frac{J^2}{4K_0^2}\cos^2\theta \qquad (C8)$$

where J^2 is the average square of the angular momentum of the compound nucleus and K_0^2 the width parameter in the Gaussian distribution of K.[28]

Figure C2 shows the results of fitting each angular distribution by the method of least squares with equation C4. By assuming the angular momentum projection does not change appreciably with neutron evaporation and equating C4 with C7, we obtain the plots on the right hand side of Figure C2. In this picture $\overline{K_0^2}$ is a weighted average of the K^2 contributions from each occurring chance fission. J^2 is calculated from the optical model assuming a spin zero target. As energy is increased, average angular momentum is increased, and fissionability increases.

A word of caution is in order at this point. The anisotropies are obtained from measuring fission fragments due to first and second chance fission at least. Therefore in order

to obtain more than qualitative information from the anisotropies the contribution from each fission chance must be unfolded.

Figure C2. Experimental fission fragment anisotropy coefficients, ϵ , and the corresponding $\overline{K_o^2}$ as functions of excitation energy in the initial compound nucleus.

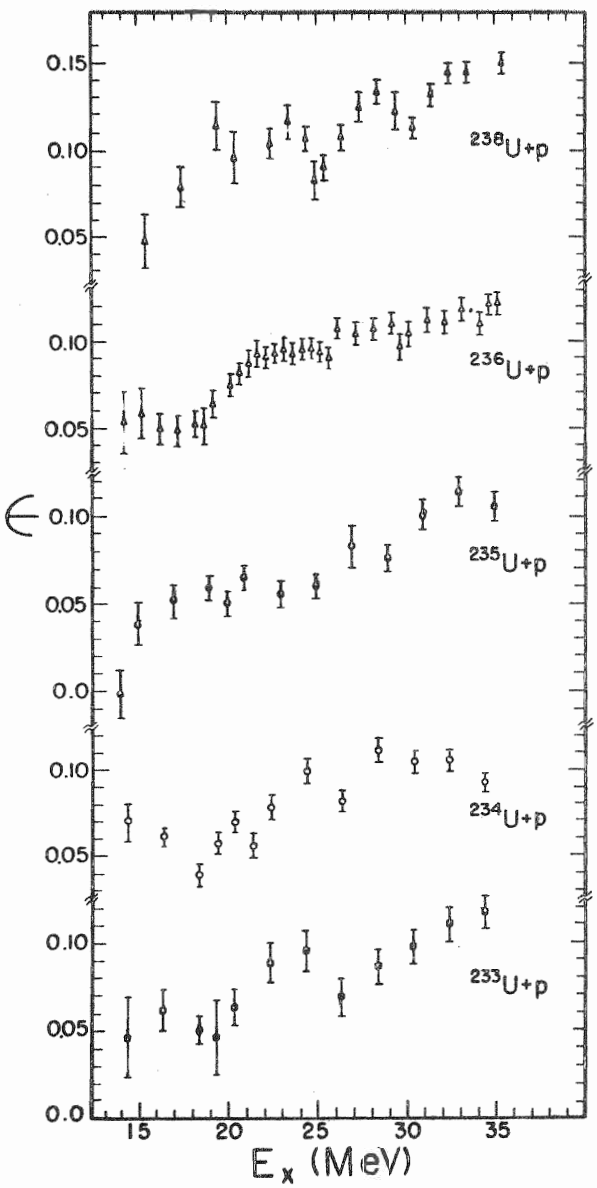
0.15
0.10
0.05
0.10
0.05
0.10
0.05
0.0
0.10
0.05
0.10
0.05
0.0
15
20
25
30
35
E_x (MeV)
^{238}U+p
^{236}U+p
^{235}U+p
^{234}U+p
^{233}U+p

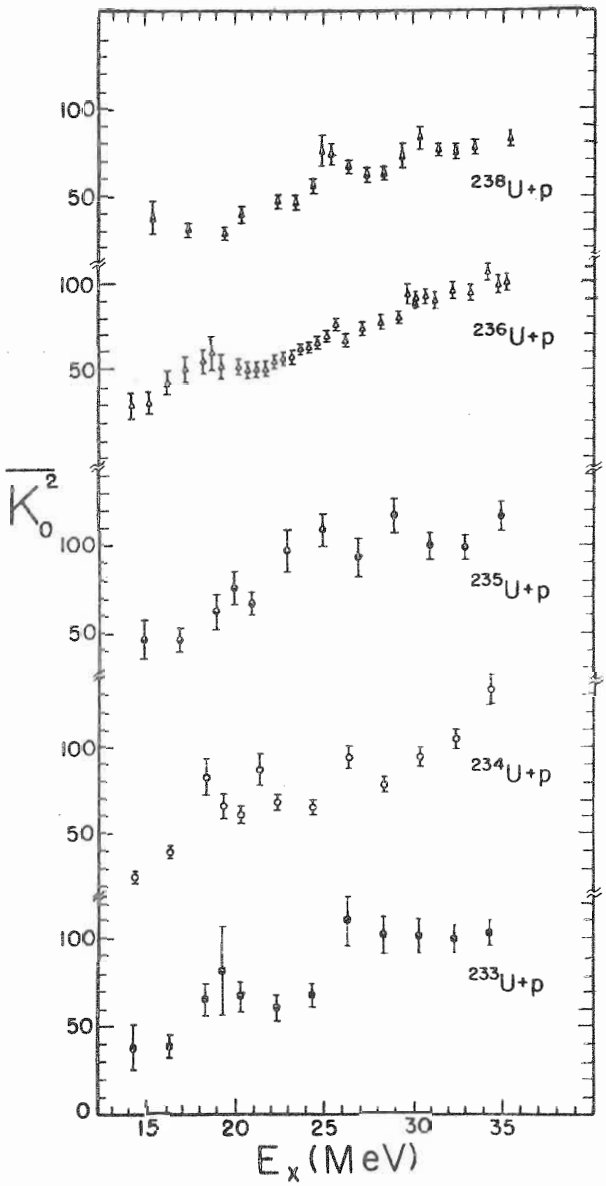
100
50
100
50
100
50
100
50
0
15
20
25
30
35
E_x (MeV)
$\overline{K_0^2}$
^{238}U+p
^{236}U+p
^{235}U+p
^{234}U+p
^{233}U+p

Appendix D
Angular Momentum Effects on the Model

The level density formulation of Gilbert and Cameron[11] includes angular momentum as follows:

$$\rho(E,J) = \rho(E,0)\, f_J(E)$$

where

$$f_J(E) = \begin{cases} (2J+1)\exp\left[\dfrac{-(J+1/2)^2}{2\sigma_x^2}\right] & \text{for } E < E_x \\ (2J+1)\exp\left[\dfrac{-(J+1/2)^2}{2\sigma^2}\right] & \text{for } E > E_x \end{cases}$$

and J = angular momentum of the system.

Substituting these into the formulas for Γ_n/Γ_f and summing over the final state spins one arrives at an approximate angular momentum correction for Γ_n/Γ_f as follows:[29]

$$\left(\frac{\Gamma_n}{\Gamma_f}\right)_J = \left(\frac{\Gamma_n}{\Gamma_f}\right)_0 \exp\left\{-\left(\frac{1}{2\sigma_n^2} - \frac{1}{2\sigma_f^2}\right) J(J+1)\right\}$$

where $J(J+1)$ is the mean square angular momentum of the initial compound nucleus. The change in angular momentum caused by neutron emission is small and can be neglected. The important quantities here are the level density spin cut off parameters for the ground state deformation, σ_n^2, and the saddle point deformation, σ_f^2, which are related to the effective moments of inertia. If we assume an extreme case of $\sigma_f^2 = \sigma_n^2$ and assume the values of $J(J+1)$ calculated by the optical model (See Fig. B4) then Γ_n/Γ_f is effectively reduced by about 12% at E_p = 30 MeV. The actual effects of angular momentum are expected to be smaller than this estimate. These effects can easily be absorbed in slight changes in a_f/a_n and thus explicit consideration of angular momentum does not seem meaningful.

Appendix E

Parameter Tables

The following tables list the parameters used in the calculations shown in figures 13, 15, 16, 17, 18, and 19, respectively. The compound nucleus formation cross section, σ_c, used is given by $\sigma_c = f_c(E_p)\,\sigma_R$. The optical model parameters of Becchetti and Greenlees were used in all cases. The shape parameter for the single peaked fission barrier, $\hbar\omega_f$, was always taken to be 0.6 MeV.

TABLE E1

Parameters for Figure 13

$$f_c(E_p) = 1.0 + 0.0/E_p + 0.0/E_p^2$$

A	E_f^A	P(Z)	P(N)	S(Z)	S(N)	a_f/a_m
239	6.227	0.00	0.43	-5.48	0.00	1.000
238	5.480	0.00	0.00	-5.48	0.00	1.000
237	6.619	0.00	0.49	-5.48	0.00	1.000
236	5.691	0.00	0.00	-5.48	0.00	1.000
235	6.991	0.00	0.57	-5.48	0.00	1.000
234	6.120	0.00	0.00	-5.48	0.00	1.000
233	7.350	0.00	0.60	-5.48	0.00	1.000
232	6.410	0.00	0.00	-5.48	0.00	1.000
231	7.630	0.00	0.79	-5.48	0.00	1.000

TABLE E2

Parameters for Figure 15

$$f_c(E_p) = 1.0 + 0.0/E_p + 0.0/E_p^2$$

A	E_f^A	P(Z)	P(N)	S(Z)	S(N)	a_f/a_m
239	5.650	0.00	0.43	-5.48	0.00	1.075
238	6.000	0.00	0.00	-5.48	0.00	1.075
237	5.500	0.00	0.49	-5.48	0.00	1.075
236	5.500	0.00	0.00	-5.48	0.00	1.075
235	5.400	0.00	0.57	-5.48	0.00	1.075
234	5.300	0.00	0.00	-5.48	0.00	1.075
233	4.750	0.00	0.60	-5.48	0.00	1.075
232	5.050	0.00	0.00	-5.48	0.00	1.075
231	5.050	0.00	0.79	-5.48	0.00	1.075

TABLE E3

Parameters for Figure 16

$$f_c(E_p) = 1.0 - 2.0/E_p - 2.0/E_p^2$$

A	E_f^A	P(Z)	P(N)	S(Z)	S(N)	a_f/a_m
239	5.650	0.00	0.43	-5.48	0.00	1.075
238	6.000	0.00	0.00	-5.48	0.00	1.075
237	5.500	0.00	0.49	-5.48	0.00	1.075
236	5.500	0.00	0.00	-5.48	0.00	1.075
235	5.400	0.00	0.57	-5.48	0.00	1.075
234	5.300	0.00	0.00	-5.48	0.00	1.075
233	4.750	0.00	0.60	-5.48	0.00	1.075
232	5.050	0.00	0.00	-5.48	0.00	1.075
231	5.050	0.00	0.79	-5.48	0.00	1.075

TABLE E4

Parameters for Figure 18

$$f_c(E_p) = 1.0 - 2.0/E_p - 2.0/E_p^2$$

A	E_f^A	P(Z)	P(N)	S(Z)	S(N)	a_f/a_m
239	5.650	0.00	0.50	-5.48	0.00	1.075
238	6.000	0.00	0.00	-5.48	0.00	1.075
237	5.500	0.00	0.75	-5.48	0.00	1.075
236	5.500	0.00	0.00	-5.48	0.00	1.075
235	5.400	0.00	0.65	-5.48	0.00	1.075
234	5.300	0.00	0.00	-5.48	0.00	1.075
233	4.750	0.00	0.40	-5.48	0.00	1.075
232	5.050	0.00	0.00	-5.48	0.00	1.075
231	5.050	0.00	0.40	-5.48	0.00	1.075

TABLE E5

Parameters for Figure 19

$$f_c(E_p) = 1.0 - 2.0/E_p - 2.0/E_p^2$$

A	E_f^A	P(Z)	P(N)	S(Z)	S(N)	a_f/a_m
239	5.650	0.00	0.50	-5.48	0.00	1.085
238	6.000	0.00	0.00	-5.48	0.00	1.100
237	5.500	0.00	0.75	-5.48	0.00	1.085
236	5.500	0.00	0.00	-5.48	0.00	1.070
235	5.400	0.00	0.65	-5.48	0.00	1.040
234	5.300	0.00	0.00	-5.48	0.00	1.025
233	4.750	0.00	0.40	-5.48	0.00	1.025
232	5.050	0.00	0.00	-5.48	0.00	1.025
231	5.050	0.00	0.40	-5.48	0.00	1.025

LIST OF REFERENCES

1. V. M. Strutinsky, Sov. J. Nucl. Phys. 3, 449 (1966); Nucl. Phys. A95, 420 (1967); Nucl. Phys. A122, 1 (1968).

2. Yu. A. Muzychka et al., Yad Fiz. 8, 716 (1968); Sov. J. Nucl. Phys. 8, 417 (1969).

3. S. G. Nilsson et al., Nucl. Phys. A115, 545 (1968); S. G. Nilsson et al., Nucl. Phys. A131, 1 (1969); J. R. Nix, Proceedings of the Interniional Conference on the Properties of Nuclei Far From the Region of Beta-Stability, Leysin, 1970, Report CERN 70-30, Geneva, 1970, Vol. 2. p. 605; T. Johansson et al., Ann. Phys. (Paris) 5, 377 (1970).

4. R. Vandenbosch and J. R. Huizenga, Proceedings of the Second United Nations International Conference on the Peaceful Uses of Atomic Energy, Geneva, 1958 (United Nations, Geneva, Switzerland, 1958), Vol. 15, p. 284; J. R. Huizenga et al., Phys. Rev. 126, 210 (1962).

5. F. D. Becchetti and G. W. Greenlees, Phys. Rev. 182, 1190 (1969).

6. N. Bohr and J. A. Wheeler, Phys. Rev. 56, 426 (1939).

7. J. R. Huizenga and R. Vandenbosch, "Nuclear Fission" a contribution to Vol. II of Nuclear Reactions (Amsterdam: North Holland Publishing Company, 1962), Editors, P. M. Endt and M. Demeur.

8. F. G. Perey, Phys. Rev. 131, 745 (1963).

9. J. J. H. Menet et al., Phys. Rev. C4, 1114 (1971).

10. C. H. Johnson and R. L. Kernell, Phys. Rev. C2, 639 (1970).

11. A. Gilbert and A. G. W. Cameron, Can. J. Phys. 43, 144 (1965).

12. H. K. Vonach and J. R. Huizenga, Phys. Rev. 138, B1372 (1965).

13. T. Ikkelnad et al., Phys. Rev. C3, 329 (1971).

14. H. C. Britt et al., Phys. Rev. C4, 1444 (1971).

15. D. L. Hill and J. A. Wheeler, Phys. Rev. 89, 1102 (1953).

16. V. F. Weisskopf, Phys. Rev. 52, 295 (1937).

17. J. E. Lynn, The Theory of Neutron Resonance Reactions (Clarendon Press, Oxford, 1968), p. 316

18. R. J. Eastgate and R. A. Hardekopf, Bull. Am. Phys. Soc. 16, 517 (1971).

19. V. E. Viola, Jr. and B. D. Wilkins, Nucl. Phys. 82, 65 (1966).

20. H. W. Schmitt and R. B. Murray, Phys. Rev. 116, 1575 (1960).

21. Neutron Cross Sections Vol III Z=88 to 98. BNL-325 Second Edition, Supplement No. 2, p. 93-237-6.

22. P. Decowski et al., Nucl. Phys. A110, 129 (1968).

23. R. Vandenbosch and U. Mosel, Phys. Rev. Lett. 28, 1726 (1972).

24. L. G. Moretto et al., Phys. Rev. 178, 1845 (1969); Phys. Lett. 38B, 471 (1972).

25. G. L. Bate And J. R. Huizenga, Phys. Rev. 136B, B1471 (1964).

26. D. G. Foster, Jr. and D. W. Glasgow, Phys Rev. C3, 576 (1971); D. W. Glasgow and D. G. Foster, Jr., Phys. Rev. C3, 604 (1971).

27. I. Halpern and V. M. Strutinsky, Proceedings of the Second United Nations International Conference on the Peaceful Uses of Atomic Energy, Geneva, 1958 (United Nations, Geneva, Switzerland, 1958), Vol. 15, P. 365; See also E. K. Hyde, The Nuclear Properties of the Heavy Elements Vol. III (Prentice-Hall, 1964) p. 365.

28. S. Bjornholm and V. M. Stutinsky, Nucl. Phys. A136, 1 (1969).

29. R. Bass, Private Communication (1972).

BIOGRAPHY

James Reid Boyce

Personal: Born December 22, 1941, Morelia, Michoacan, Mexico.

Education: B.S. Physics-Mathematics, Florida State University 1964;
M.S. Physics, Florida State University 1966.

Memberships: American Physical Society
Sigma Pi Sigma

M. S. Thesis: Investigations of Alpha Particle Induced Electron Tunneling Through Thin Film Barriers.

Abstracts:

1. Measurement of the Cross Section for Proton Induced Fission of ^{235}U for Proton Energies from 6.75 MeV to 30.0 MeV. (with T. D. Hayward, F. O. Purser, H. W. Schmitt, and H. W. Newson) Bull. Am. Phys. Soc. 15 , 1693 (1970).

2. Proton Induced Fission Cross Sections of the Uranium Isotopes (with T. D. Hayward, F. O. Purser, H. W. Schmitt, and H. W. Newson) Bull. Am. Phys. Soc. 16, 517 (1971).

3. Measurements of the Fission Fragment Angular Distributions for Proton Induced Fission of ^{236}u, ^{235}U, and ^{234}U for Proton Energies from 9.0 MeV to 30.0 MeV. (with T. D. Hayward, F. O. Purser, H. W. Schmitt, and H. W. Newson) Bull. Am. Phys. Soc. 16, 517 (1971).

4. Statistical Analysis of Fission Cross Sections (with R. Bass, T. D. Hayward, F. O. Purser, and H. W. Newson) Bull. Am. Phys. Soc. 23, 54 (1972).